Spring 2013

Development of a methodology for pseudo-rigid-body models of compliant segments with inserts, and experimental validation

Raghvendra Sharadchandra Kuber

Recommended Citation

Kuber, Raghvendra Sharadchandra, "Development of a methodology for pseudo-rigid-body models of compliant segments with inserts, and experimental validation" (2013). *Masters Theses*. 5363.
https://scholarsmine.mst.edu/masters_theses/5363

DEVELOPMENT OF A METHODOLOGY FOR PSEUDO-RIGID-BODY MODELS OF COMPLIANT SEGMENTS WITH INSERTS, AND EXPERIMENTAL VALIDATION

by

RAGHVENDRA SHARADCHANDRA KUBER

A THESIS

Presented to the Faculty of the Graduate School of the

MISSOURI UNIVERSITY OF SCIENCE AND TECHNOLOGY

In Partial Fulfillment of the Requirements for the Degree

MASTER OF SCIENCE IN MECHANICAL ENGINEERING

2013

Approved by

Dr. Ashok Midha, Advisor
Dr. John Sheffield
Dr. Shun Takai

ABSTRACT

Compliant mechanisms have shown a great deal of potential in the last few decades in providing better solutions to design problems with numerous benefits; however, their use has been limited due to current challenges in the material selection. With ever increasing focus on the applications of compliant mechanisms, it is necessary to find alternatives to the existing materials and methods of prototyping. The purpose of this work is to develop a methodology for pseudo-rigid-body models of compliant segments with compliant inserts, comprised of a resilient material placed between the layers of a softer material, to alleviate any creep and strength issues associated with the softer material. The pseudo-rigid-body models (PRBMs) for such beams subjected to various boundary conditions are presented and validated by means of analytical and experimental methods.

Pseudo-rigid-body models are used to devise simple methods of large deflection analysis, and help expedite the compliant mechanism design process. A method to improve the accuracy of the PRBM of a fixed-free beam by evaluating more accurate values of the stiffness coefficient is also presented.

ACKNOWLEDGMENTS

I would like to express my deepest gratitude and thanks to my advisor Dr. Ashok Midha for his never ending support, and excellent guidance throughout the duration of this research study. His continual encouragement and unflagging enthusiasm have been very inspiring, and have contributed significantly to the success of this work. I would also like to express my thanks to Dr. John Sheffield and Dr. Shun Takai for their invaluable time and effort as my committee members.

I would like to express a special thanks to my friend and research partner Sushrut Bapat for his valuable guidance and help during the experimental stage. It has been a pleasure working with him over the past two years. I wish to sincerely thank my other research partners, Ashish Koli and Vivekananda Chinta, and all my friends at Missouri S&T for the many enlightening conversations throughout this research effort. Support in the form Graduate Teaching Assistantships provided by the Department of Mechanical and Aerospace Engineering, Missouri S&T, is gratefully acknowledged.

Finally, I am deeply indebted to my parents, Mr. Sharadchandra Kuber, Mrs. Savita Kuber, my sisters Mrs. Meenakshi Kulkarni and Mrs. Snehal Kulkarni for their unconditional love and support, and God Almighty for guiding me through the various stages of my life.

TABLE OF CONTENTS

APPENDICES

LIST OF ILLUSTRATIONS

LIST OF TABLES

1. INTRODUCTION

1.1. COMPLIANT MECHANISMS

A mechanism is a mechanical device used to transfer motion, force, or energy (Erdman and Sandor, 1991; Shigley and Uicker, 1995; and Howell, 2001). Traditionally, the mechanisms are comprised of rigid links connected together through movable joints, or kinematic pairs (Howell, 2001). A simple example of a rigid-body mechanism is a planar four-bar linkage with a single degree of freedom. In the past couple of decades, research interest has had a phenomenal growth in a new class of mechanisms called "compliant mechanisms." A compliant mechanism gains some or all of its mobility from the deflection of at least one of its flexible members (Her, 1986; Howell and Midha, 1993; and Howell, 2001). A compliant fish hook remover (Compliers®), shown in Figure 1.1, is one such device.

Figure 1.1. Compliers®: A Compliant Fish Hook Remover

Compliant mechanisms are an attractive alternative to their rigid-body counterparts due to the many potential benefits they offer the designer, mentioned below:

a) The total number of parts in a mechanism may be significantly reduced. The reduction in the number of parts, in turn, can save on manufacturing and assembly costs significantly. The mechanism may even be fabricated as a single piece, using milling, extruding, injection molding, or other processes (Howell and Midha, 1993).
b) The mechanism may have a reduced number of rigid-body joints, resulting in reduced wear, backlash, and noise, and increased mechanical precision and reliability. The need for lubrication may also be eliminated (Sevak and McLarnan, 1974; and Her, 1986).
c) Since the mobility of compliant mechanisms involves the deflection of their flexible members, strain energy is stored in the flexible members. This energy can easily be stored or transformed, and may be applied toward a beneficial end in the design.
d) The energy storage characteristics may be used to design mechanisms that have specific force-deflection properties, or to cause a mechanism to tend to particular mobility positions (Howell, 2001).

As examples, Compliers® and Compliant Grippers (Byers, 1990; and Byers and Midha, 1991) illustrated in Figure 1.1 and Figure 1.2 highlight some of these advantages. In spite of the inherent advantages of compliant mechanisms, the use of compliant mechanisms has been limited due to following associated challenges (Howell, 2001):

a) Design and analysis of a compliant mechanism is relatively more difficult than those of a rigid-body mechanism.

b) Compliant links or segments subjected to long periods of mechanical or thermal loading may experience creep, if fabricated from polymeric materials.

c) Flexible segments when loaded cyclically over a period of time are prone to fatigue failure.

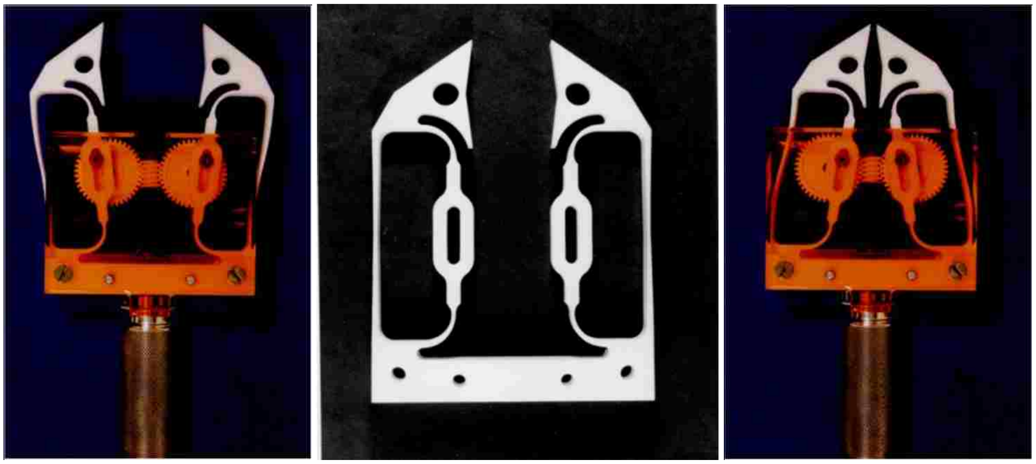

(a) (b) (c)

Figure 1.2. Compliant Grippers (a) In Open Position; (b) Fully Compliant (One-Piece); and (c) Grippers in Closed Position

1.2. HISTORICAL BACKGROUND

The early efforts in the area of compliant mechanisms (Burns, 1964), and (Burns and Crossley 1966, 1968) addressed the challenges involved in the design of compliant mechanisms, and developed closed-form solutions for simple geometric shapes using a kinetostatic analysis, for the analysis and synthesis of compliant mechanisms. Initial approximations to the problem solutions were obtained by using elliptic integral solutions of the undulating and nodal elastica, developed by Shoup and McLarnan (1971) and

Shoup (1972). Sevak and McLarnan (1974) used finite element techniques, along with optimization routines, to synthesize compliant mechanisms for function generation.

Her (1986), Her and Midha (1987), Howell (1993), and Murphy (1993) introduced the compliance number concept and investigated the mobility issues in compliant mechanisms. A finite element chain approach to analysis (Harrison, 1973; Miller, 1980; and Coulter and Miller, 1988) was further developed, referred to as the chain algorithm, and applied to compliant mechanism analysis (Midha, 1983), this was modified and improved upon by Her (1986), Salamon (1989), Midha et al. (1922a), and Her et al. (1992). Hill (1987), and Hill and Midha (1990) applied a graphical, user driven iterative technique for better convergence of the chain algorithm. A general methodology of adding compliance to a rigid-body design to obtain a compliant mechanism was presented by Salamon (1989). Salamon (1989), and Salamon and Midha (1992) studied the effects of compliance on the mechanical advantage of mechanisms.

Howell and Midha (1991) investigated the effects of compliance on the input/output characteristics of toggle mechanisms. Byers (1990) and Byers and Midha (1991) designed a gripper mechanism comprised of compliant, undulating structural members, which helped to produce a near parallel motion of gripping fingers using the chain algorithm. Nahvi (1991) used the finite element techniques to investigate the dynamics of large-deflection compliant mechanisms. He introduced the concept of using eigenvalues of the structural stiffness matrix, obtained from static analysis of the compliant mechanisms, as a structural stiffness and stability indicator.

Howell and Midha (1994) proposed a method for the design of compliant mechanisms comprised of small-length flexural pivots. The concept of using pseudo-rigid-body models to analyze and optimize compliant mechanisms was proposed. The mechanism thus obtained would be verified later using the chain algorithm with a Newton-Raphson shooting method. Howell (1991), and Howell and Midha (1995) further developed the pseudo-rigid-body model concept by presenting kinematic models for initially-straight cantilevered flexible segments, subjected to end-force loading, pure moment loading, and certain combined end-force and moment loading. Norton (1991) developed a stiffness coefficient definition for initially-straight, end-force loaded compliant members, to understand their force-deflection characteristics.

Murphy (1993) modified and expanded the existing type synthesis theory to include the complexities and unique features of compliant mechanisms, and proposed a novel method for the type synthesis of compliant mechanisms. Norton (1991), Midha et al., (1992b), Midha et al., (1992c), and Midha et al., (1994) proposed the nomenclature and classification of compliant mechanisms. Norton (1991), and Midha et al. (2000) used the triangle inequality concept (Midha et al., 1986; Norton et al., 1991, 1993, 1994; and Khanuja et al., 1994) and the pseudo-rigid-body model to investigate the kinematic mobility issues associated with compliant mechanisms.

Howell and Midha (1996) presented a generalized loop-closure synthesis technique for simple, yet efficient design of compliant mechanisms using the pseudo-rigid-body model concept. In this technique, the kinematic synthesis equations were combined with the work-energy equations obtained from virtual work principles, to account for the strain energy stored in flexible members. Mettlach and Midha (1999) proposed the characteristic deflection domain concept for planar compliant members subjected to end-force loading and certain combined end-force and moment loading. The concept of using average, single- or multi-segment pseudo-rigid-body models for planar compliant members of known geometry, to obtain initial estimates of end forces and/or moment for prescribed displacement boundary conditions, was introduced. Mettlach and Midha (1995, 1996) also implemented a graphical or analytical synthesis technique and Burmester theory using input torque and/or potential energy considerations in compliant mechanism design.

1.3. SCOPE OF THE INVESTIGATION

The objective of this work is to present a methodology for the development of pseudo-rigid-body models (PRBMs) of compliant segments with inserts, i.e., a strong material inside outer layers of a softer material, to alleviate the creep and strength issues associated with the softer material. Section 2 presents a brief overview of two important methods adopted by various researchers for the large deflection analysis of flexible beams.

Section 3 presents a method to improve the accuracy of the PRBM of a fixed-free beam by expressing the stiffness coefficient (K_Θ) as a function of the pseudo-rigid-body angle, Θ and the load factor, n. The improved expressions of stiffness coefficient for compressive and tensile loading have been evaluated and presented.

Section 4 presents a pseudo-rigid-body model based approach, for the analysis and modeling of compliant beams with inserts for various boundary conditions and cases. The PRBMs presented are validated using elliptic integral solutions and finite element analysis solutions. Section 5 deals with the experimental testing and validation of a fixed-free compliant beam with an insert subject to vertical, vertical and compressive and vertical and tensile loading. The results of an experiment comparing the creep behavior of plastic beams with and without insert material are discussed as well.

Section 6 presents a brief summary of the current research effort, and offers recommendations for future study.

2. LARGE DEFLECTION ANALYSIS

2.1. INTRODUCTION

Compliant mechanisms generally comprise of one or more flexible members that may be required to undergo large deflections. The geometrically nonlinear deflections often associated with the motion of compliant mechanisms increase the complexity of analysis and design of the flexible members and requires special considerations in deriving methods for their analysis. Much research has been undertaken into the analysis of large-deflection members (Howell, 1991). The linearized beam equations assume small deflection, and limit the applications to small-motion mechanisms. These equations are inadequate for the analysis of structural members that undergo large deflections.

The Bernoulli-Euler equation states that the bending moment is proportional to the beam curvature, i.e.

$$\kappa = \frac{d\theta}{ds} = \frac{M}{EI} + \frac{1}{R_i} \tag{2.1}$$

Where, κ is the curvature, M is the internal moment, θ the slope of the beam, s the length along curved beam, and EI the flexural rigidity, and R_i the initial undeflected radius of curvature of the beam at a given point.

For an initially-curved beam with a constant curvature, $1/R_i$ is a constant. A special case is a beam with zero initial curvature referred to as an initially-straight beam. The curvature may be written as,

$$\left(\frac{d\theta}{ds}\right) = \frac{\frac{d^2y}{dx^2}}{\left\{1 + \left(\frac{dy}{dx}\right)^2\right\}^{\frac{3}{2}}} \tag{2.2}$$

where, y is the transverse deflection and x the coordinate along the undeflected beam axis. For small deflections, $\left(\frac{dy}{dx}\right)^2$ is assumed to be negligibly small compared to unity. This assumption leads to the classical Euler-Bernoulli moment-curvature equation as follows (Shigley and Mischke, 2003):

$$M = EI\left(\frac{d^2y}{dx^2}\right) \tag{2.3}$$

However, when the beam undergoes large deflections, the slope $\frac{dy}{dx}$ may no longer be small and a small-deflection assumption will produce inaccurate results.

Analysis methods such as the closed-form solution, numerical methods, and pseudo-rigid-body approximations are used for compliant mechanisms as well. Bernoulli, in the 17th century, began the theoretical treatment of beam deflection. Later, in the 18th century, Euler developed the differential equation for slender beam deflection curves. Bisshopp and Drucker (1945) first derived a closed-form solution for large deflection cantilever beams with a vertical end load using elliptic integrals. Frisch-Fay (1962) summarized in a monograph, methods used by researchers to arrive at solutions.

Howell (1991) presented generalized, closed-form elliptic integral solutions for straight flexible members subjected to combined end force and moment. These were used to develop equivalent pseudo-rigid-body models (PRBMs) for large deflection members. In recent years, the closed-form elliptic integral and PRBM solutions for various cases and boundary conditions have been developed. This section provides a brief overview of these two distinct methods for standard compliant segments subjected to various boundary conditions.

2.2. CANTILEVER BEAM (FIXED-PINNED) WITH A FORCE AT THE FREE END

Figure 2.1 shows an initially-straight cantilever beam of length *l* and flexural rigidity *EI* subjected to non-follower horizontal and vertical end forces *nP* and *P*, respectively. The combined end forces may be treated as a single force *F* acting at an angle ϕ, where $\phi = \tan^{-1}\left(-\frac{1}{n}\right)$.

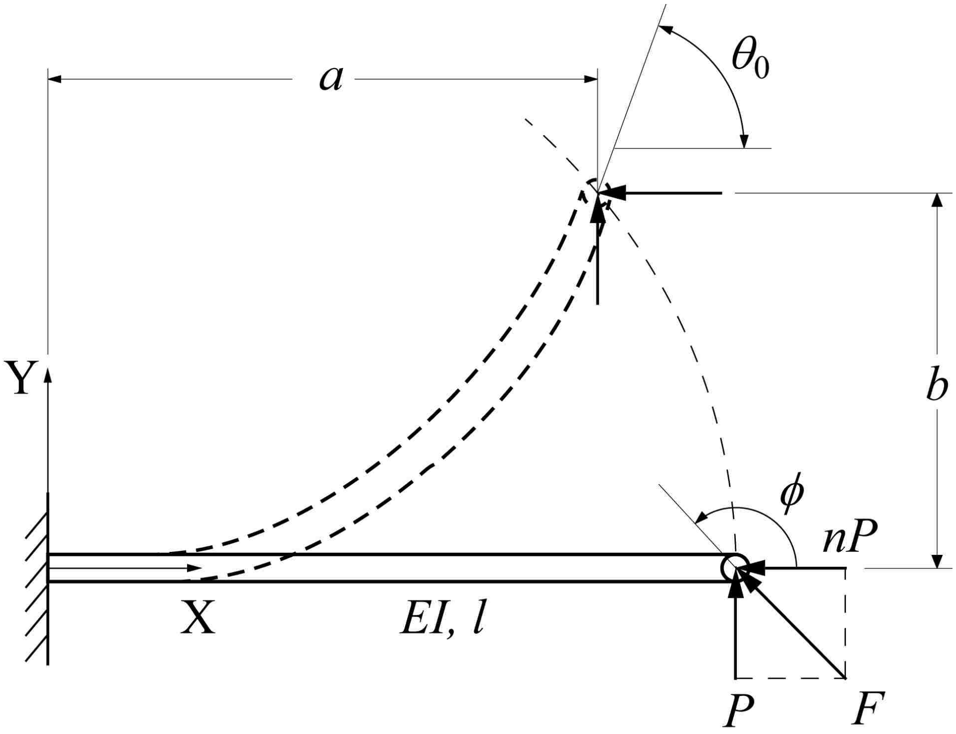

Figure 2.1. A Cantilever Beam with Forces at Free End

2.2.1. Closed-Form Elliptic Integral Solution. Bisshopp and Drucker (1945) used the elliptic integrals to find a closed-form solution for a large deflection cantilever beam subjected to a vertical end load. Burns (1964), Burns and Crossley (1968), Shoup and McLarnan (1971), Shoup (1972), and Winter and Shoup (1972) used these closed-form solutions in the analysis of flexible-link mechanisms. Howell (1991) presented generalized, elliptic integral equations for the end deflection of a flexible cantilever beam of uniform cross section subjected to a combined end force and moment loading.

From the generalized elliptic integral solutions (Howell, 1991), the beam end coordinates of the above cantilever beam may be given by:

for beam end angle $\theta_0 < \phi$,

$$\alpha = \frac{1}{\sqrt{\eta}}\left[F\left[\frac{\pi}{2}, t\right] - F[\gamma, t]\right] \tag{2.4}$$

$$\begin{aligned}\frac{a}{l} = \frac{1}{\alpha\eta^{5/2}}\Bigg\{&-n\eta\left[\left[F\left[\frac{\pi}{2}, t\right] - F[\gamma, t]\right] + 2\left[E[\gamma, t] - E\left[\frac{\pi}{2}, t\right]\right]\right] \\ &+ \sqrt{2\eta(\eta + \lambda)}\cos\gamma\Bigg\}\end{aligned} \tag{2.5}$$

$$\begin{aligned}\frac{b}{1} = \frac{1}{\alpha\eta^{5/2}}\Bigg\{&\eta\left[\left[F\left[\frac{\pi}{2}, t\right] - F[\gamma, t]\right] + 2\left[E[\gamma, t] - E\left[\frac{\pi}{2}, t\right]\right]\right] \\ &+ n\sqrt{2\eta(\eta + \lambda)}\cos\gamma\Bigg\}\end{aligned} \tag{2.6}$$

where,

$$\alpha = \sqrt{\frac{Pl^2}{EI}} \tag{2.7}$$

$$\lambda = \eta \cos(\theta_0 - \phi) \tag{2.8}$$

$$\eta = \sqrt{1 + n^2}; \qquad \phi = \tan^{-1}\left(-\frac{1}{n}\right) \tag{2.9}$$

$$\gamma = \sin^{-1}\sqrt{\frac{\eta - n}{\eta + \lambda}}; \qquad t = \sqrt{\frac{n + \lambda}{2\eta}} \tag{2.10}$$

and, $F[\beta, q]$ and $E[\beta, q]$ denote the incomplete elliptic integrals of the first kind and second kind respectively, with amplitude β and modulus q, calculated as,

$$F[\beta, q] = \int_0^\beta \frac{d\theta}{\sqrt{1 - q^2 \sin^2\theta}} \tag{2.11}$$

$$E[\beta, q] = \int_0^\beta \sqrt{1 - q^2 \sin^2\theta}\, d\theta \tag{2.12}$$

The elliptic integral solutions discussed above yield greater accuracy in large deflection analysis; however, these methods could only be applied to relatively simple geometries and loadings, and is often associated with convergence difficulties while solving set of nonlinear equations. The method also requires several simplifying assumptions such as linear material properties and inextensible members (Howell, 2001). A more simplified and efficient model was needed for the analysis of large deflection members.

2.2.2. Pseudo-Rigid-Body Model. Howell and Midha (1995) developed a physical model, called the pseudo-rigid-body model (PRBM), utilizing the observations of the nearly circular nature of beam end deflection paths in the elliptic integral solutions. In a PRBM, a compliant beam is simulated by rigid segments that are connected by a pin joint (characteristic pivot). A torsional spring is placed at the pin joint to simulate the beam compliance. Figure 2.2 shows the equivalent pseudo-rigid-body model of an initially-straight cantilever beam of length *l* and flexural rigidity *EI* subject to non-follower horizontal and vertical end forces *nP* and *P*, respectively.

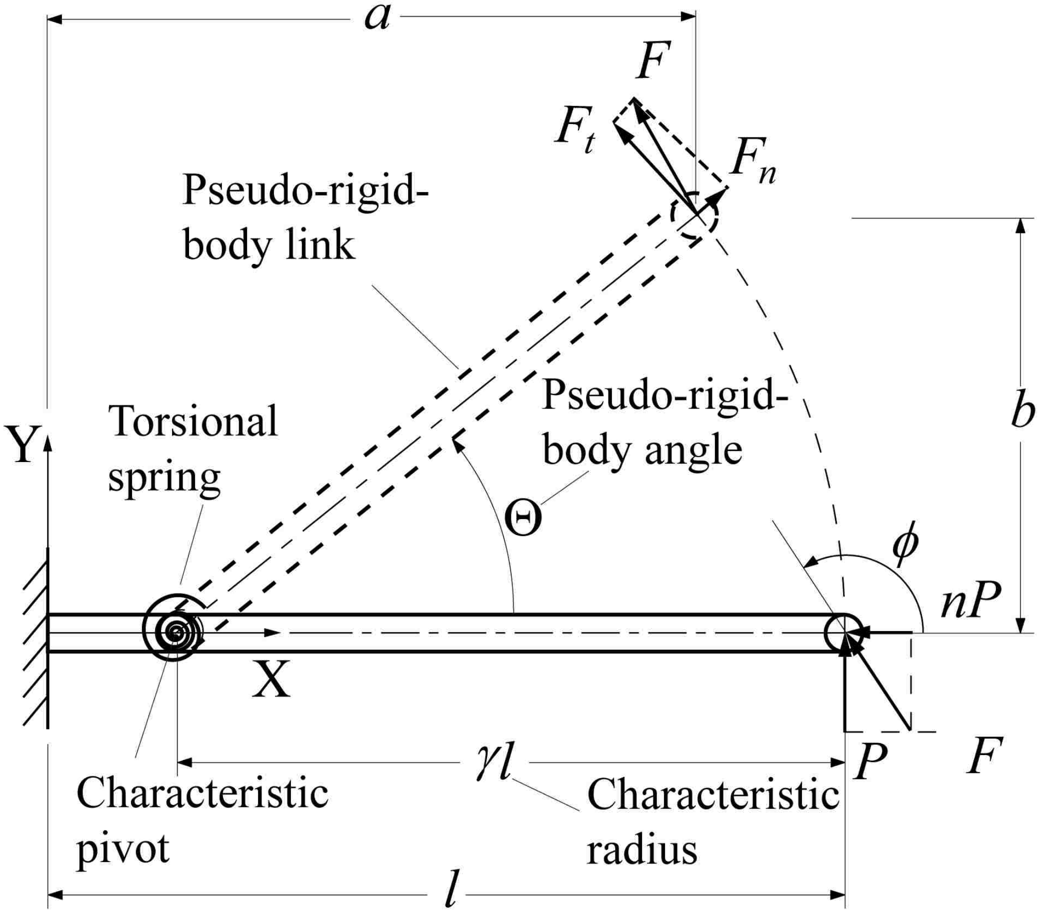

Figure 2.2. Pseudo-Rigid-Body Model of an End-Force-Loaded Cantilever Beam

A PRBM for a fixed-free compliant beam consists of two rigid segments pinned at the characteristic pivot. The beam's resistance to bending, or compliance, is modeled through a torsional spring located at the characteristic pivot. The characteristic radius factor γ helps locate the characteristic pivot along the undeformed beam geometry and is determined through optimization such that the characteristic radius γL will trace the beam end deflection path to within a defined error of 0.5% with respect to the corresponding closed-form elliptic integral solution (Howell, 1991). The beam end angle is denoted as θ_0, pseudo-rigid-body angle as Θ, vertical displaced position of the beam end as 'b', and the horizontal displaced position as 'a'.

In addition to the foundational work of Howell and Midha (1995), Pauly and Midha (2004) improved upon the PRBM parameters for a fixed-free compliant beam subjected to end forces, discussed briefly below.

The characteristic radius factor γ is given as:

$$\begin{aligned}
\gamma &= 0.855651 - 0.016438n, for\ -4 < n \leq -1.5 \\
\gamma &= 0.852138 - 0.01861n, for\ -1.5 < n \leq -0.5 \\
\gamma &= 0.851892 - 0.020805n + 0.005967n^2 - 0.000895n^3 \\
&\quad + 0.000069n^4 - 0.000002n^5, for\ -0.5 < n \leq 10
\end{aligned} \tag{2.13}$$

Beam end angle can be related to pseudo-rigid-body angle through the parametric angle coefficient c_θ (Howell, 2001) such that,

$$\theta_0 = c_\theta \Theta \tag{2.14}$$

The parametric angle coefficient c_θ is given as:

$$c_\theta = 1.238945 + 0.012035n + 0.00454n^2, for \ -4 < n \leq -0.5$$

$$c_\theta = 1.238845 + 0.009113n - 0.001929n^2 + 0.000191n^3 + 0.00039n^4 - 0.000013n^5, for \ -0.5 < n \leq 10 \tag{2.15}$$

The beam stiffness coefficient K_Θ is given as:

$$K_\Theta = 2.66041 - 0.069005n - 0.002268n^2, for \ -4 < n \leq -0.5$$

$$K_\Theta = 2.648834 - 0.074727n + 0.026328n^2 - 0.004609n^3 + 0.00039n^4 - 0.000013n^5, for \ -0.5 < n \leq 10 \tag{2.16}$$

The non-dimensional tangential load factor (Howell, 2001) is given as:

$$\alpha_t^2 = \frac{F_t l^2}{EI} \tag{2.17}$$

where, the tangential load, F_t, is given by,

$$F_t = Fsin(\phi - \Theta) \tag{2.18}$$

$$F = P\sqrt{1 + n^2}\,, \tag{2.19}$$

and the load factor,

$$n = \frac{nP}{n} \tag{2.20}$$

$$\phi = \tan^{-1}\left(-\frac{1}{n}\right) \tag{2.21}$$

also,

$$\alpha_t^2 = K_\Theta \Theta \tag{2.22}$$

The beam end coordinates are given by,

$$\frac{a}{l} = 1 - \gamma(1 - \cos\Theta) \tag{2.23}$$

$$\frac{b}{l} = \gamma \sin\Theta \tag{2.24}$$

2.3. INITIALLY-CURVED FIXED FREE SEGMENT

Figure 2.3 shows an initially-curved cantilever beam of length *l* and flexural rigidity *EI* subjected to non-follower horizontal and vertical end forces *nP* and *P*, respectively. The beam has an initial radius of curvature R_i and hence a curvature of $1/R_i$.

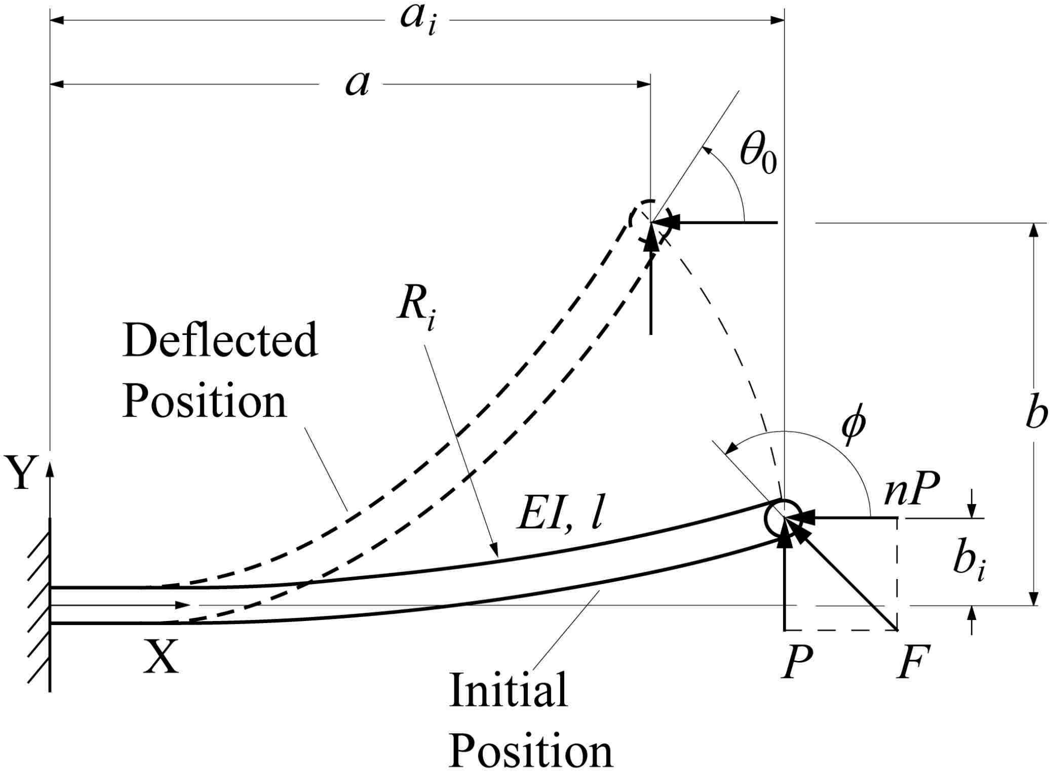

Figure 2.3. Initially-Curved Beam with Forces at Free End

The initial curvature can be related to the beam length using the non-dimensional parameter κ_0 as,

$$\kappa_0 = \frac{l}{R_i} \tag{2.25}$$

Figure 2.4 illustrates the beam shapes for various κ_0, in the range: $0 \le \kappa_0 \le 2$.

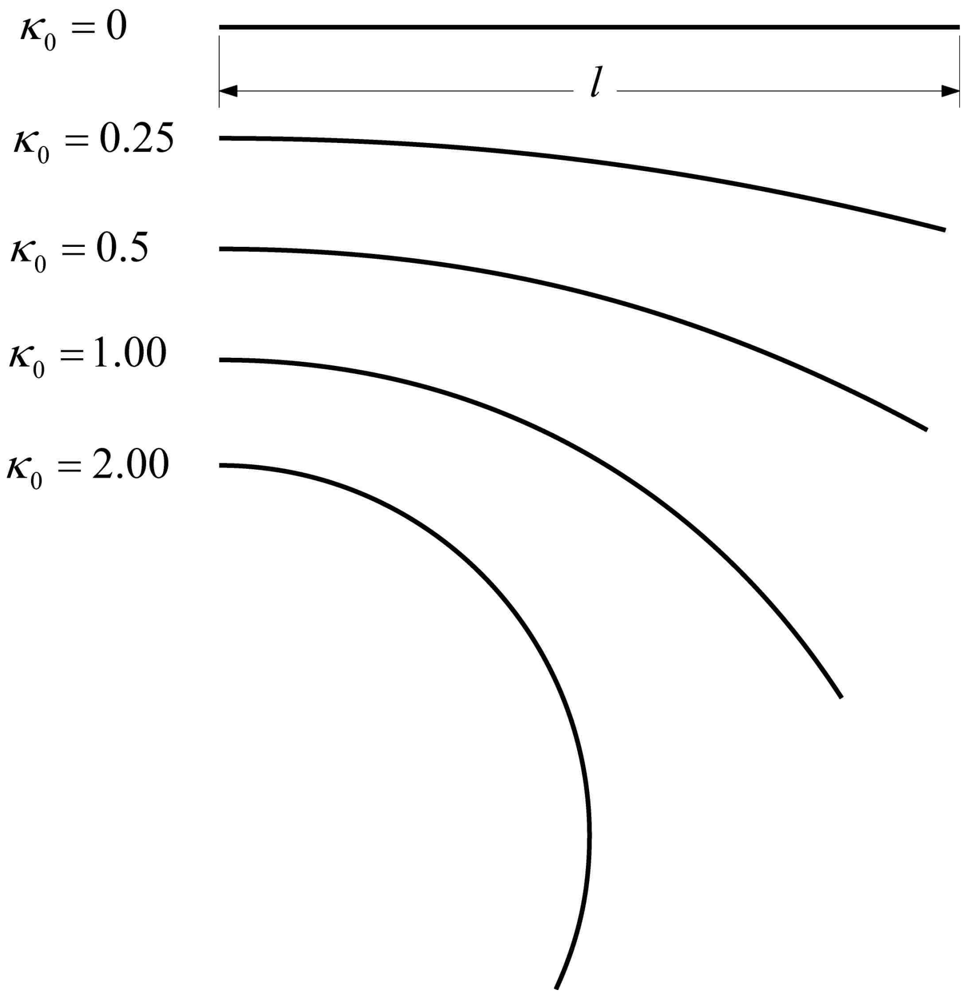

Figure 2.4. Beam Shapes for Various κ_0

2.3.1. Closed-Form Elliptic Integral Solution. Howell (1991) presented elliptic integral solutions of such cantilever beam with initial curvature subjected to a combination of end forces. The simplified equations for the end deflections are summarized below (Howell, 2001):

$$\eta = \sqrt{1+n^2} \tag{2.26}$$

$$\phi = \tan^{-1}\left(-\frac{1}{n}\right) \tag{2.27}$$

for $|\lambda| < \eta; \phi - \cos^{-1}(-\lambda/n) \leq -\theta_0 < \phi'$ and $\alpha \neq 0$,

$$\alpha = \frac{1}{\sqrt{\eta}}[F[\gamma_2, t] - F[\gamma_1, t]] \tag{2.28}$$

$$\begin{aligned}\frac{\mathrm{a}}{l} = \frac{1}{\alpha\eta^{5/2}}\Big\{-n\eta\left[[F[\gamma_2, t] - F[\gamma_1, t]] + 2\big[E[\gamma_1, t] - E[\gamma_2, t]\big]\right] \\ + \sqrt{2\eta(\eta+\lambda)}(\cos\gamma_1 - \cos\gamma_2)\Big\}\end{aligned} \tag{2.29}$$

$$\begin{aligned}\frac{b}{l} = \frac{1}{\alpha\eta^{5/2}}\Big\{\eta\left[[F[\gamma_2, t] - F[\gamma_1, t]] + 2\big[E[\gamma_1, t] - E[\gamma_2, t]\big]\right] \\ + n\sqrt{2\eta(\eta+\lambda)}(\cos\gamma_1 - \cos\gamma_2)\Big\}\end{aligned} \tag{2.30}$$

for $\lambda > \eta; \phi - \pi \leq -\theta_0$

$$\alpha = \sqrt{\frac{2}{\lambda+\eta}}[F[\psi_2, r] - F[\psi_1, r]] \tag{2.31}$$

$$\begin{aligned}\frac{a}{l} = \frac{\sqrt{2(\eta+\lambda)}}{\alpha\eta^2}\left\{-n\left[\frac{\lambda}{\eta+\lambda}[F[\psi_2, r] - F[\psi_1, r]] + \big[E[\psi_1, r] - E[\psi_2, r]\big]\right]\right. \\ \left. + \left[\sqrt{1 - \frac{\eta - n}{\eta+\lambda}} - \sqrt{1 - \frac{\eta + \sin\theta_0 - n\cos\theta_0}{\eta+\lambda}}\right]\right\}\end{aligned} \tag{2.32}$$

$$
\begin{aligned}
\frac{b}{l} = \frac{\sqrt{2(\eta+\lambda)}}{\alpha\eta^2} & \left\{ \frac{\lambda}{\eta+\lambda}\left[F[\psi_2,r]-F[\psi_1,r]\right]+\left[E[\psi_1,r]-E[\psi_2,r]\right]\right. \\
& \left. + n\left[\sqrt{1-\frac{\eta-n}{\eta+\lambda}} - \sqrt{1-\frac{\eta+\sin\theta_0-n\cos\theta_0}{\eta+\lambda}}\right]\right\}
\end{aligned}
\tag{2.33}
$$

where,

$$\lambda = \frac{1}{2}\left(\frac{\kappa_0}{\alpha}\right)^2 + \sin\theta_0 - n\cos\theta_0 \tag{2.34}$$

$$\eta = \sqrt{1+n^2}; \qquad \phi' = \tan^{-1}\left(\frac{1}{n}\right) \tag{2.35}$$

$$\alpha = \sqrt{\frac{Pl^2}{EI}} \tag{2.36}$$

$$\gamma_1 = \sin^{-1}\sqrt{\frac{\eta-n}{\eta+\lambda}}; \quad \gamma_2 = \sin^{-1}\sqrt{\frac{\eta+\sin\theta_0-n\cos\theta_0}{\eta+\lambda}} \tag{2.37}$$

$$\psi_1 = \sin^{-1}\sqrt{\frac{\eta-n}{2\eta}}; \quad \psi_2 = \sin^{-1}\sqrt{\frac{\eta+\sin\theta_0-n\cos\theta_0}{\psi_1}} \tag{2.38}$$

$$t = \sqrt{\frac{\eta+\lambda}{2\eta}}; \qquad r = \sqrt{\frac{2\eta}{\eta+\lambda}} \tag{2.39}$$

2.3.2. Pseudo-Rigid-Body Model. Figure 2.5 (Howell, 1991) shows the pseudo-rigid-body-model of an initially-curved cantilever beam of length *l* and flexural rigidity *EI* subjected to combined end forces. The characteristic radius length γl is measured along the beam as if it were initially straight.

The initial beam end coordinates $a_i$and b_i (Howell, 2001) are,

$$a_i = \frac{l}{\kappa_0}\sin\kappa_0 = 0 \tag{2.40}$$

$$b_i = \frac{l}{\kappa_0}(1-\cos\kappa_0) \tag{2.41}$$

To account for the curvature, the length of rigid-body link is ρl where ρ is given by,

$$\rho = \left\{\left[\frac{a_i}{l} - (1-\gamma)\right]^2 + \left(\frac{b_i}{l}\right)^2\right\}^{\frac{1}{2}} \tag{2.42}$$

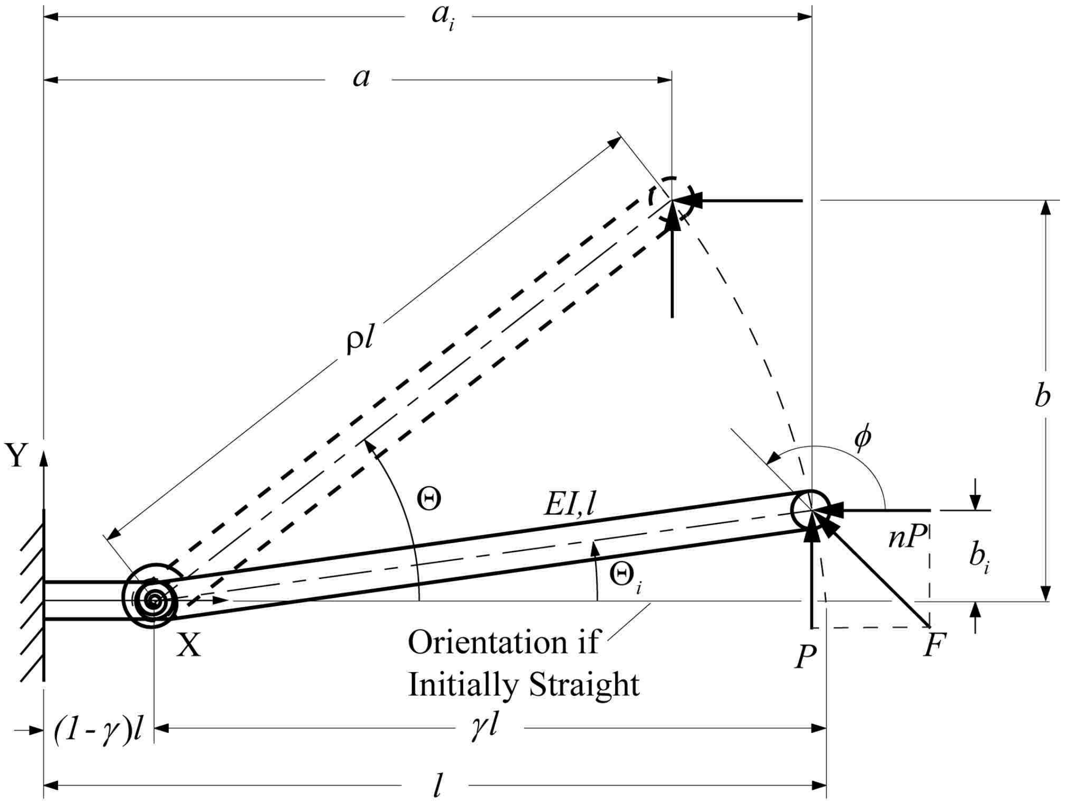

=

Figure 2.5. Pseudo-Rigid-Body Model of an Initially-Curved Cantilever Beam

Due to the initial curvature of the beam, the pseudo-rigid-body angle Θ will have a non-zero initial value such that,

$$\Theta_i = \tan^{-1}\frac{b_i}{a_i - l(1-\gamma)} \tag{2.43}$$

The non-dimensional tangential load factor is,

$$\alpha_t^2 = \frac{F_t l^2}{EI} \tag{2.44}$$

where,

$$F_t = F\sin(\phi - \Theta) \tag{2.45}$$

$$F = P\sqrt{1+n^2} \tag{2.46}$$

$$n = \frac{nP}{n} \tag{2.47}$$

$$\phi = \tan^{-1}\left(-\frac{1}{n}\right) \tag{2.48}$$

also,

$$\alpha_t^2 = K_\Theta(\Theta - \Theta_i) \tag{2.49}$$

The beam end coordinates are given by,

$$\frac{a}{l} = 1 - \gamma + \rho\cos\Theta \tag{2.50}$$

$$\frac{b}{l} = \rho\sin\Theta \tag{2.51}$$

2.4. INITIALLY-STRAIGHT SMALL LENGTH FLEXURAL PIVOT

Figure 2.6 shows an initially-straight cantilever beam subjected to non-follower horizontal and vertical end forces *nP* and *P*, respectively. The beam consists of two segments: one is shorter of length *l*, and the other longer of length *L*. The small segment is significantly shorter and more flexible than the long element, i.e. $L \gg l$, and $(EI)_L \gg (EI)_l$.

The small segment is referred to as *small-length flexural pivot* (Howell, 2001). Usually, L is 10 or more times larger than l. The following section presents the closed-form elliptic integral solution for an initially-straight SLFP subjected to a combination of axial and transverse forces.

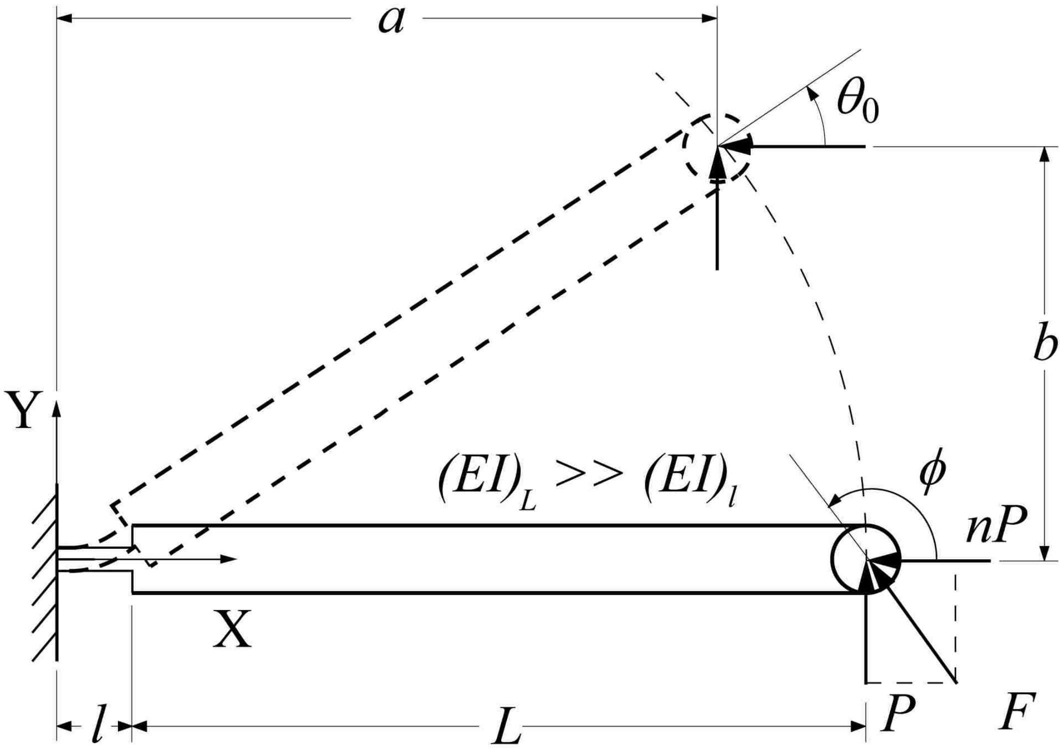

Figure 2.6. Initially-Straight Small-Length Flexural Pivot

2.4.1. Closed-Form Elliptic Integral Solution. As the beam is comprised of two discrete segments, the total displacement may be determined from the superposition of the elastic displacement of the compliant segment and the rigid-body displacement of the rigid segment. The elastic displacement of the compliant segment is due to the equivalent force and moment acting on the segment, determined from the beam end forces. The rotation of the rigid segment of the beam is dictated by the beam end angle of the compliant segment.

The force *F* acting at the beam end may be computed (Howell, 2001) as:

$$F = \sqrt{P^2 + (nP)^2} \tag{2.52}$$

The angle of the force *F* is given by

$$\phi = tan^{-1}\left(-\frac{1}{n}\right) \tag{2.53}$$

The transverse or tangential component of this force may be expressed as:

$$F_t = Fsin(\phi - \theta_0) \tag{2.54}$$

As seen in Figure 2.7, the beam end force *F* can be transferred to the compliant segment as a combination of force *F* and an equivalent moment M_0. The moment acting on the beam end of the compliant segment due to the tangential component F_t may be written as,

$$M_0 = F_t L \tag{2.55}$$

$$M_0 = FL\sin(\phi - \theta_0) \tag{2.56}$$

where,

$$\phi = \tan^{-1}\left(-\frac{1}{n}\right) \tag{2.57}$$

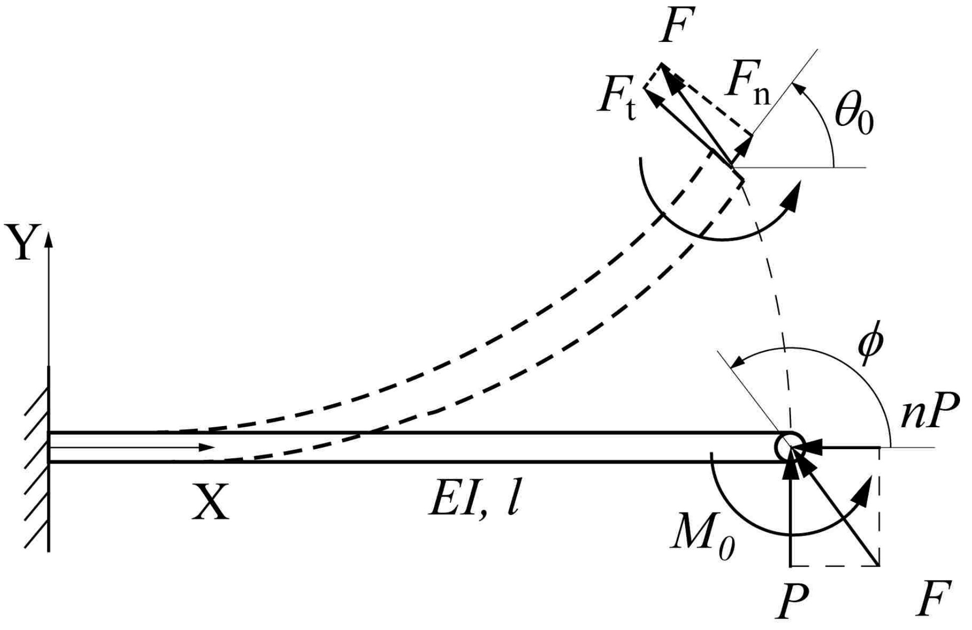

Figure 2.7. Equivalent Forces and Moment Acting on the Straight SLFP Segment

The deflection of the compliant segment may be calculated using existing knowledge of the large deflection beam theory for a fixed-free cantilever beam with a force and moment applied at the free end. The total displacement of the beam is calculated by superimposing the displacement of the rigid segment attached to the end of the compliant segment. The beam end coordinates of the deflected beam, may be expressed as follows:

$$\alpha = \frac{1}{\sqrt{2}} \int_0^{\theta_0} \frac{d\theta}{\sqrt{\cos(\theta_0 - \phi) - \cos(\theta - \phi) + \lambda}} \tag{2.58}$$

$$\frac{b}{l} = \frac{1}{\sqrt{2}\alpha} \int_0^{\theta_0} \frac{\sin\theta \, d\theta}{\sqrt{\cos(\theta_0 - \phi) - \cos(\theta - \phi) + \lambda}} + L \sin\theta_0 \tag{2.59}$$

$$\frac{\mathrm{a}}{l} = \frac{1}{\sqrt{2}\mathrm{\alpha}}\int_0^{\theta_0} \frac{\cos\theta\, d\theta}{\sqrt{\cos(\theta_0 - \phi) - \cos(\theta - \phi) + \lambda}} + L\cos\theta_0 \tag{2.60}$$

where,

$$\alpha = \sqrt{\frac{Fl^2}{EI}} \tag{2.61}$$

$$\lambda = \frac{1}{2}\left(\frac{M_0}{EI}\right)^2 \left(\frac{l}{\alpha}\right)^2 \tag{2.62}$$

E is the elastic modulus, *I* the moment of inertia, and *l* the length of the flexural pivot. The input parameters to the system of equations (2.58 - 2.60) are the three load parameters α, λ, and ϕ. Given these three load boundary conditions, the tip deflection parameters θ_0, *a/l* and *b/l* can be computed easily. The large deflection equations can be solved using numerical integration, or the elliptic integral solution (Howell, 1991), as summarized below.

for $|\lambda| < \eta; \phi - \cos^{-1}(-\lambda/n) \leq -\theta_0 < \phi'$ and $\alpha \neq 0$,

$$\alpha = \frac{1}{\sqrt{\eta}}[F[\gamma_2, t] - F[\gamma_1, t]] \tag{2.63}$$

$$\begin{aligned}\frac{\mathrm{a}}{l} = \frac{1}{\alpha\eta^{5/2}}\Big\{&-n\eta\,\Big[[F[\gamma_2, t] - F[\gamma_1, t]] + 2\big[E[\gamma_1, t] - E[\gamma_2, t]\big]\Big] \\ &+ \sqrt{2\eta(\eta + \lambda)}(\cos\gamma_1 - \cos\gamma_2)\Big\} + L\cos\theta_0\end{aligned} \tag{2.64}$$

$$\begin{aligned}\frac{b}{l} = \frac{1}{\alpha\eta^{5/2}}\Big\{&\eta\,\Big[[F[\gamma_2, t] - F[\gamma_1, t]] + 2\big[E[\gamma_1, t] - E[\gamma_2, t]\big]\Big] \\ &+ n\sqrt{2\eta(\eta + \lambda)}(\cos\gamma_1 - \cos\gamma_2)\Big\} + L\sin\theta_0\end{aligned} \tag{2.65}$$

for $\lambda > \eta;\ \phi - \pi \leq -\theta_0 < \phi' and\ \alpha \neq 0$,

$$\alpha = \sqrt{\frac{2}{\lambda+\eta}}\,[F[\psi_2,r]-F[\psi_1,r]] \tag{2.66}$$

$$\begin{aligned}\frac{a}{l} = \frac{\sqrt{2(\eta+\lambda)}}{\alpha\eta^2}\Bigg\{&-n\left[\frac{\lambda}{\eta+\lambda}[F[\psi_2,r]-F[\psi_1,r]]+\big[E[\psi_1,r]-E[\psi_2,r]\big]\right]\\ &+\left[\sqrt{1-\frac{\eta-n}{\eta+\lambda}}-\sqrt{1-\frac{\eta+\sin\theta_0-n\cos\theta_0}{\eta+\lambda}}\right]\Bigg\}+L\cos\theta_0\end{aligned} \tag{2.67}$$

$$\begin{aligned}\frac{b}{l} = \frac{\sqrt{2(\eta+\lambda)}}{\alpha\eta^2}\Bigg\{&\frac{\lambda}{\eta+\lambda}[F[\psi_2,r]-F[\psi_1,r]]+\big[E[\psi_1,r]-E[\psi_2,r]\big]\\ &+n\left[\sqrt{1-\frac{\eta-n}{\eta+\lambda}}-\sqrt{1-\frac{\eta+\sin\theta_0-n\cos\theta_0}{\eta+\lambda}}\right]\Bigg\}+L\sin\theta_0\end{aligned} \tag{2.68}$$

where,

$$\alpha = \sqrt{\frac{Pl^2}{EI}} \tag{2.69}$$

$$\lambda = \frac{1}{2}\left(\frac{M_0}{EI}\right)^2\left(\frac{l}{\alpha}\right)^2+\sin\theta_0-n\cos\theta_0 \tag{2.70}$$

$$\eta = \sqrt{1+n^2}; \qquad \phi' = \tan^{-1}\left(\frac{1}{n}\right) \tag{2.71}$$

$$\gamma_1 = \sin^{-1}\sqrt{\frac{\eta-n}{\eta+\lambda}}; \qquad \gamma_2 = \sin^{-1}\sqrt{\frac{\eta+\sin\theta_0-n\cos\theta_0}{\eta+\lambda}} \tag{2.72}$$

$$\psi_1 = \sin^{-1}\sqrt{\frac{\eta-n}{2\eta}}; \qquad \psi_2 = \sin^{-1}\sqrt{\frac{\eta+\sin\theta_0-n\cos\theta_0}{\psi_1}} \tag{2.73}$$

$$t = \sqrt{\frac{\eta+\lambda}{2\eta}}; \qquad r = \sqrt{\frac{2\eta}{\eta+\lambda}} \tag{2.74}$$

2.4.2. Pseudo-Rigid-Body Model. Howell and Midha (1994) developed a pseudo-rigid-body model for an initially-straight small-length flexural pivot subjected to end transverse and axial forces as shown in Figure 2.8. The beam is modeled as two rigid links pinned at the characteristic pivot located at the center of the undeformed flexural pivot. The pseudo-rigid-body angle, Θ, describes the rotation of the rigid link. For small-length flexural pivots, the pseudo-rigid-body angle is assumed to be equal to the beam end angle (Howell, 2001), i.e.

$$\Theta = \theta_0 \tag{2.75}$$

The compliant segment's resistance to deflection is modeled through a torsional spring located at the characteristic pivot. The stiffness of the torsional spring is given by,

$$K = \frac{EI}{l} \tag{2.76}$$

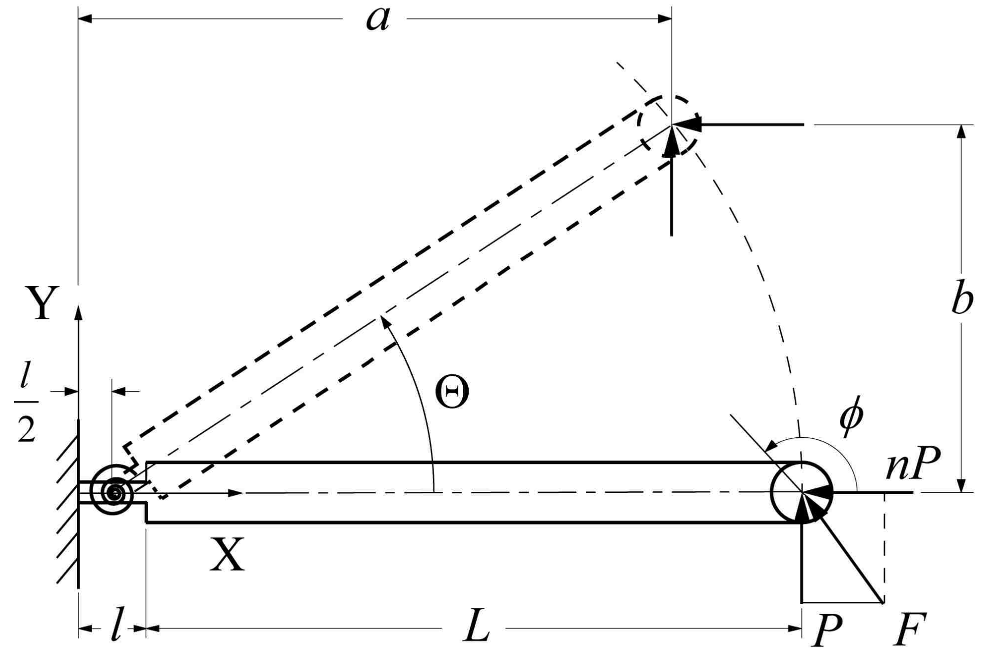

Figure 2.8. Pseudo-Rigid-Body Model of a Straight Small-Length Flexural Pivot

The beam end deflections are given by,

$$a = \frac{l}{2} + \left(L + \frac{l}{2}\right)\cos\Theta \tag{2.77}$$

$$b = \left(L + \frac{l}{2}\right)\sin\Theta \tag{2.78}$$

also,

$$K\Theta = \left(L + \frac{l}{2}\right)F\sin(\phi - \Theta) \tag{2.79}$$

The values of the non-dimensionalized beam tip deflection $\left(\frac{a}{l+L}, \frac{b}{l+L}\right)$ are calculated from the pseudo-rigid-body model equations (2.77) and (2.78). These are then compared favorably with the values obtained from the elliptic integral solution equations (2.64) and (2.65) as shown in Figure 2.9.

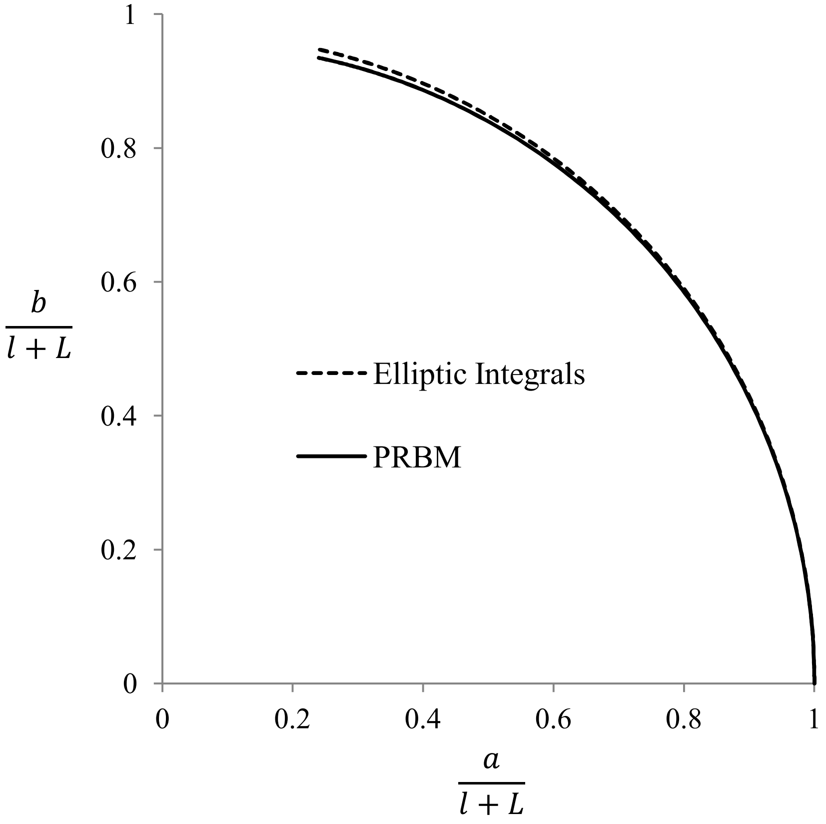

Figure 2.9. Beam End Deflections of an Initially-Straight SLFP

Figure 2.10 shows a plot of the beam end angle θ_0, calculated using the elliptic integral solution, vs the pseudo-rigid-body angle Θ. As can be seen from the figure, the plot is nearly linear, thus validating the assumption that for a small-length flexural pivot, the beam end angle is equal to the pseudo-rigid-body angle.

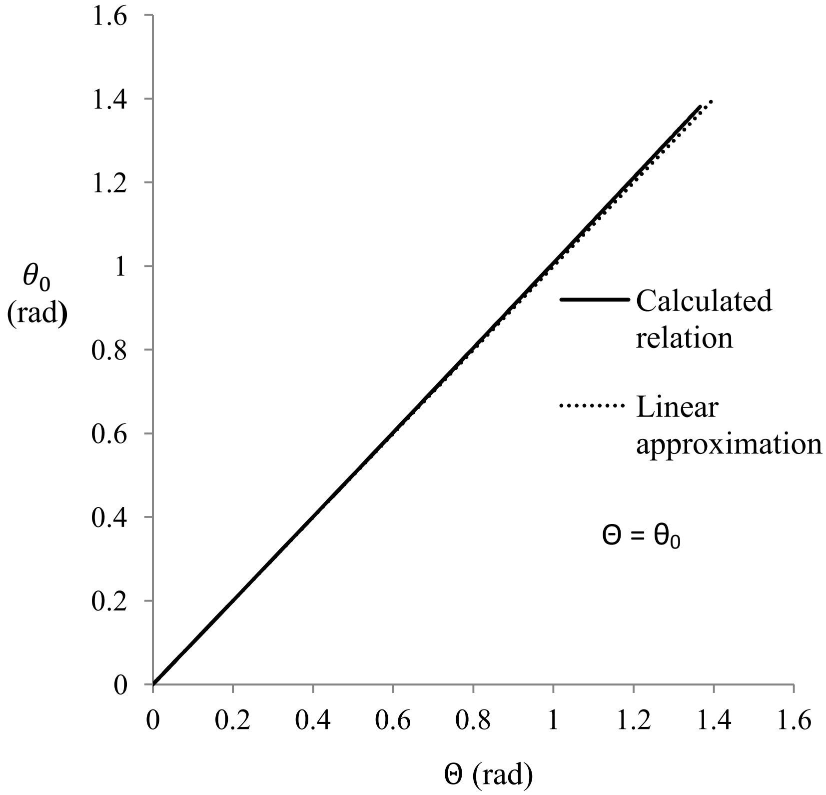

Figure 2.10. Plot of θ_0 vs. Θ for Initially-Straight SLFP

2.5. INITIALLY-CURVED SMALL-LENGTH FLEXURAL PIVOT

Figure 2.11 shows an initially-curved small-length flexural pivot of length *l* and flexural rigidity *EI* subjected to non-follower horizontal and vertical end forces *nP* and *P*, respectively. The beam has two segments; one is compliant and shorter of length *l*, and the other rigid and longer of length L. The flexural pivot has an initial radius of curvature R_i and hence a curvature of $1/R_i$. The elliptic integral solution for the initially-curved small-length flexural pivot has been presented in the following section.

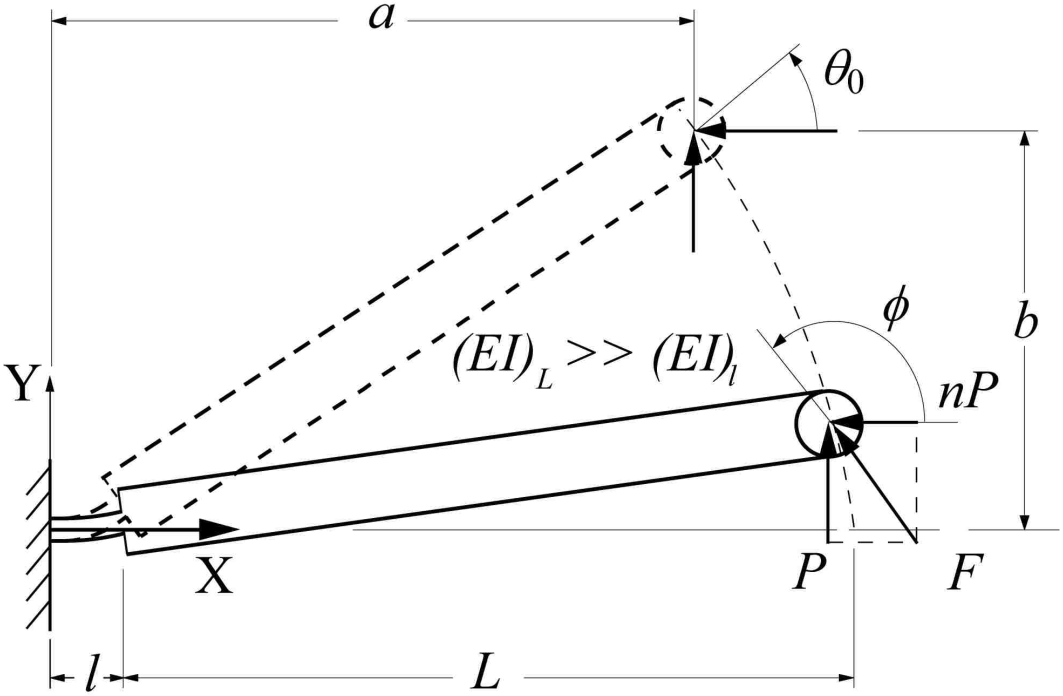

Figure 2.11. Initially-Curved Small-Length Flexural Pivot

2.5.1. Closed-Form Elliptic Integral Solution. A methodology similar to that presented in the previous section is used to derive the elliptic integral deflection solution of an initially-curved small-length flexural pivot subjected to end forces. The total displacement at the beam end may be determined by combining the elastic displacement of the initially-curved compliant segment and the rigid-body displacement of the rigid segment. The elastic displacement of the initially-curved compliant segment is due to the equivalent force and moment acting on the segment, as determined from the beam end forces. The rigid segment of the beam follows the beam end angle of the compliant segment as a force is applied.

Figure 2.12, shows the equivalent force F and moment M_0 acting on the initially-curved compliant segment, as a result of the force F applied at the beam end. The moment acting on the beam end of the compliant segment due to the tangential component F_t may be written as follows:

$$M_0 = F_t L \tag{2.80}$$

$$M_0 = FL\sin(\phi - \theta_0) \tag{2.81}$$

where,

$$\phi = \tan^{-1}\left(-\frac{1}{n}\right) \tag{2.82}$$

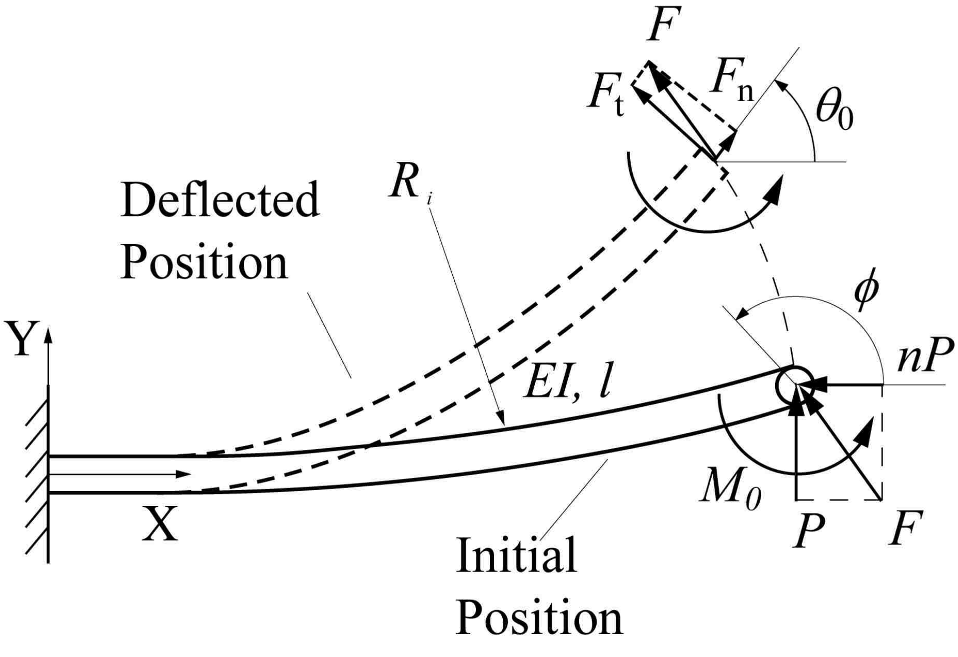

Figure 2.12. Equivalent Forces and Moment Acting on the Curved SLFP Segment

Again, the deflection of the compliant segment may be calculated using existing knowledge of the elliptic integral solution for an initially-curved fixed-free cantilever beam with a force and moment applied at the free end (Howell, 1991). The total deflection of the beam may be calculated by superimposing the deflection due to rigid-body rotation and the deflection of the compliant segment. The beam end coordinates of the deflected beam may be expressed as:

for $|\lambda| < \eta; \phi - \cos^{-1}(-\lambda/n) \leq -\theta_0 < \phi'$ and $\alpha \neq 0$,

$$\alpha = \frac{1}{\sqrt{\eta}}[F[\gamma_2, t] - F[\gamma_1, t]] \tag{2.83}$$

$$\begin{aligned} \frac{\mathrm{a}}{l} = \frac{1}{\alpha\eta^{5/2}}\Big\{-n\eta\left[[F[\gamma_2, t] - F[\gamma_1, t]] + 2\big[E[\gamma_1, t] - E[\gamma_2, t]\big]\right] \\ + \sqrt{2\eta(\eta + \lambda)}(\cos\gamma_1 - \cos\gamma_2)\Big\} + L\cos\theta_0 \end{aligned} \tag{2.84}$$

$$\begin{aligned} \frac{b}{l} = \frac{1}{\alpha\eta^{5/2}}\Big\{\eta\left[[F[\gamma_2, t] - F[\gamma_1, t]] + 2\big[E[\gamma_1, t] - E[\gamma_2, t]\big]\right] \\ + n\sqrt{2\eta(\eta + \lambda)}(\cos\gamma_1 - \cos\gamma_2)\Big\} + L\sin\theta_0 \end{aligned} \tag{2.85}$$

for $\lambda > \eta;\ \phi - \pi \leq -\theta_0 < \phi' and\ \alpha \neq 0$,

$$\alpha = \sqrt{\frac{2}{\lambda + \eta}}[F[\psi_2, r] - F[\psi_1, r]] \tag{2.86}$$

$$\begin{aligned} \frac{a}{l} = \frac{\sqrt{2(\eta + \lambda)}}{\alpha\eta^2}\left\{-n\left[\frac{\lambda}{\eta + \lambda}[F[\psi_2, r] - F[\psi_1, r]] + \big[E[\psi_1, r] - E[\psi_2, r]\big]\right]\right. \\ \left. + \left[\sqrt{1 - \frac{\eta - n}{\eta + \lambda}} - \sqrt{1 - \frac{\eta + \sin\theta_0 - n\cos\theta_0}{\eta + \lambda}}\right]\right\} + L\cos\theta_0 \end{aligned} \tag{2.87}$$

$$\frac{b}{l}=\frac{\sqrt{2(\eta+\lambda)}}{\alpha\eta^2}\left\{\frac{\lambda}{\eta+\lambda}[F[\psi_2,r]-F[\psi_1,r]]+\big[E[\psi_1,r]-E[\psi_2,r]\big]\right.$$

$$\left.+n\left[\sqrt{1-\frac{\eta-n}{\eta+\lambda}}-\sqrt{1-\frac{\eta+\sin\theta_0-n\cos\theta_0}{\eta+\lambda}}\right]\right\}+L\sin\theta_0 \tag{2.88}$$

where,

$$\alpha=\sqrt{\frac{Pl^2}{EI}} \tag{2.89}$$

$$\lambda=\frac{1}{2}\left(\frac{M_0}{EI}+\frac{1}{R_i}\right)^2\left(\frac{l}{\alpha}\right)^2+\sin\theta_0-n\cos\theta_0 \tag{2.90}$$

$$\eta=\sqrt{1+n^2};\qquad \phi'=\tan^{-1}\left(\frac{1}{n}\right) \tag{2.91}$$

$$\gamma_1=\sin^{-1}\sqrt{\frac{\eta-n}{\eta+\lambda}};\qquad \gamma_2=\sin^{-1}\sqrt{\frac{\eta+\sin\theta_0-n\cos\theta_0}{\eta+\lambda}} \tag{2.92}$$

$$\psi_1=\sin^{-1}\sqrt{\frac{\eta-n}{2\eta}};\qquad \psi_2=\sin^{-1}\sqrt{\frac{\eta+\sin\theta_0-n\cos\theta_0}{\psi_1}} \tag{2.93}$$

$$t=\sqrt{\frac{\eta+\lambda}{2\eta}};\qquad r=\sqrt{\frac{2\eta}{\eta+\lambda}} \tag{2.94}$$

2.5.2. Pseudo-Rigid-Body Model. Figure 2.13 shows the PRBM of an initially-curved small length flexural pivot. The beam has an initial radius of curvature R_i and hence a curvature of $1/R_i$. The initial curvature can be related to the beam length using the non-dimensional parameterκ_0 as:

$$\kappa_0=\frac{l}{R_i} \tag{2.95}$$

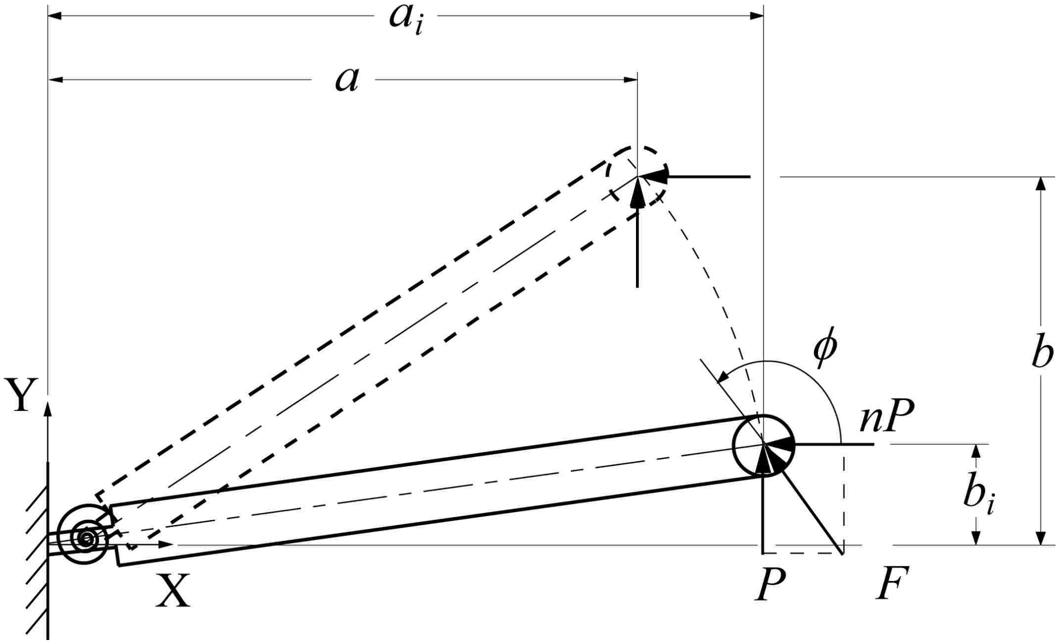

Figure 2.13. PRBM of an Initially-Curved Small-Length Flexural Pivot

The beam is modeled as two rigid links joined at the characteristic pivot located at the center of the flexural pivot along the undeformed curvature. The angle of the pseudo-rigid link is the pseudo-rigid-body angle Θ. For small-length flexural pivots, the pseudo-rigid-body angle is equal to the beam end angle, i.e.

$$\Theta = \theta_0 \tag{2.96}$$

The initial beam end coordinates a_i and b_i are,

$$a_i = \frac{l}{\kappa_0} \sin \kappa_0 + L \cos \kappa_0 \tag{2.97}$$

$$b_i = \frac{l}{\kappa_0} (1 - \cos \kappa_0) + L \sin \kappa_0 \tag{2.98}$$

As the beam is initially-curved, the pseudo-rigid-body angle Θ will have a non-zero initial value such that,

$$\Theta_i = \tan^{-1}\left(\frac{b_i - \frac{l}{2\kappa_0}(1-\cos\kappa_0)}{a_i - \frac{l}{2\kappa_0}\sin\kappa_0}\right) \tag{2.99}$$

The compliant segment's resistance to deflection is modeled through a torsional spring located at the characteristic pivot. The stiffness of the torsional spring is given by:

$$K = \frac{EI}{l} \tag{2.100}$$

The beam end deflections are given by,

$$a = \frac{l}{2\kappa_0}\sin\kappa_0 + \left(L + \frac{l}{2}\right)\cos\Theta \tag{2.101}$$

$$b = \frac{l}{2\kappa_0}(1-\cos\kappa_0) + \left(L + \frac{l}{2}\right)\sin\Theta \tag{2.102}$$

also,

$$K(\Theta - \Theta_i) = \left(L + \frac{l}{2}\right)F\sin(\phi - \Theta) \tag{2.103}$$

Figure 2.14 shows the plot of the non-dimensionalized beam tip deflection $\left(\frac{a}{l+L}, \frac{b}{l+L}\right)$, as obtained from the pseudo-rigid-body model and the elliptic integral solution.

Figure 2.15 plots the beam end angle θ_0, calculated from the elliptic integral solution, vs. the pseudo-rigid-body angle Θ. Again, it is evident that the plot is nearly linear, confirming that for a curved small-length flexural pivot, the beam end angle and the pseudo-rigid-body angle are equal.

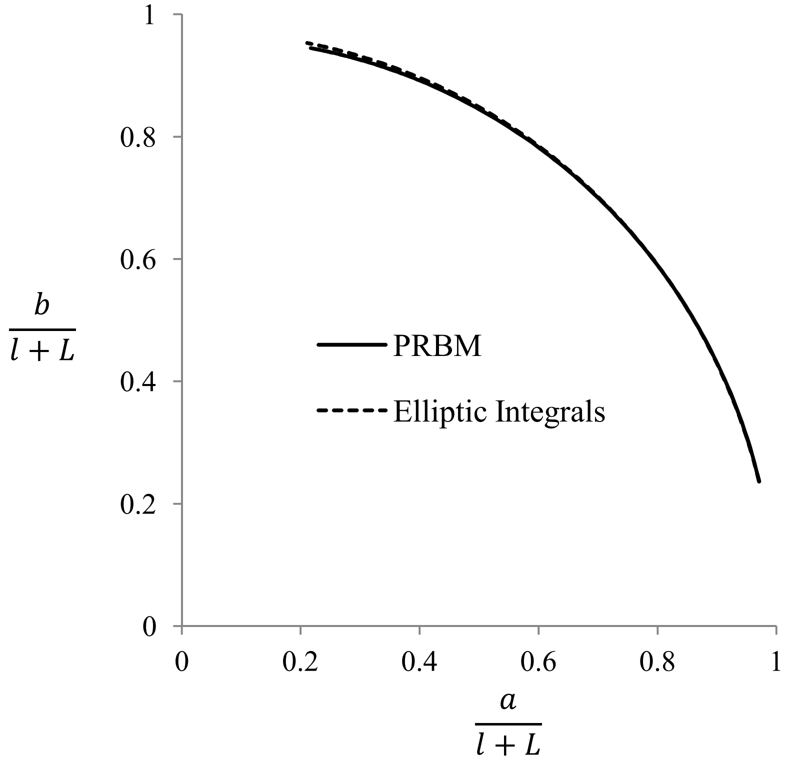

Figure 2.14. Beam End Deflections of an Initially-Curved SLFP

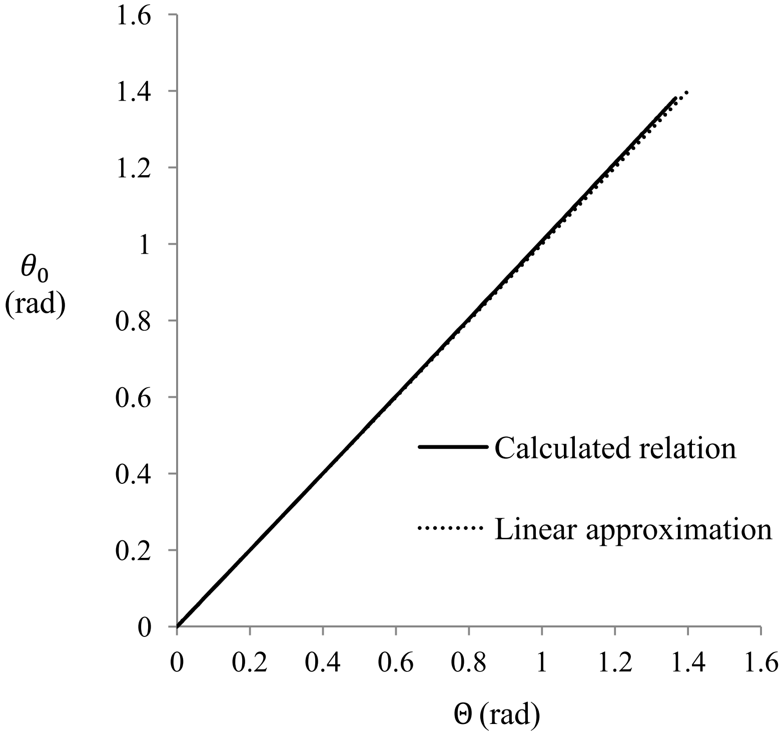

Figure 2.15. Plot of θ_0 vs. Θ for Initially-Curved SLFP

2.6. INITIALLY-CURVED PINNED-PINNED SEGMENT

Figure 2.16 shows an initially-curved pinned-pinned flexible segment of length *l* and flexural rigidity *EI* subjected to non-follower horizontal force *P*. The beam has an initial curvature κ_0 where,

$$\kappa_0 = \frac{l}{R_i} \tag{2.104}$$

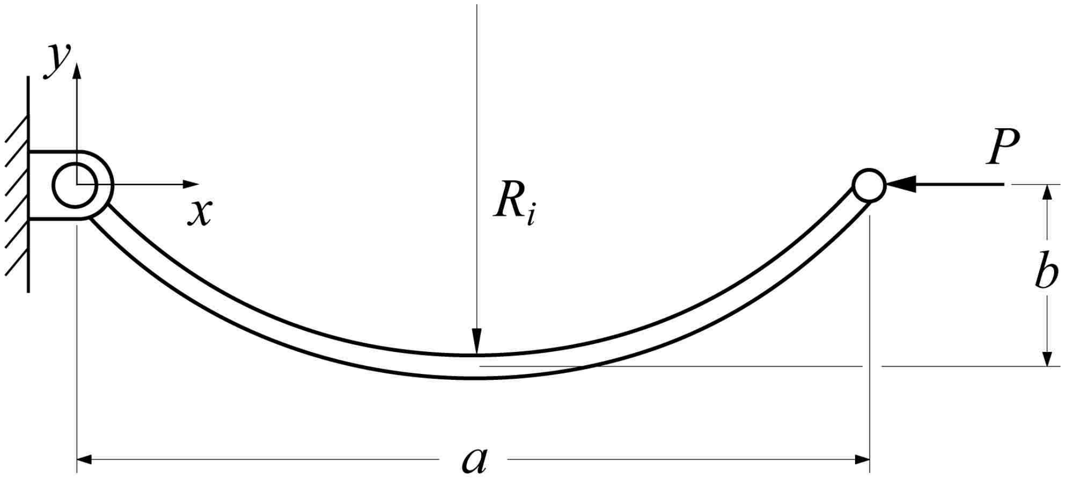

Figure 2.16. Initially-Curved Pinned-Pinned Segment

2.6.1. Closed-Form Elliptic Integral Solution. Edwards (1996) presented the elliptic integral solution for such beam. The equations are briefly summarized below: for $\lambda > 1$

$$\frac{a}{l} = \frac{1}{\alpha t}\left[(t^2 - 2)F(\beta, t) + 2E(\beta, t)\right] \tag{2.105}$$

$$\frac{b}{l} = \frac{\sqrt{2}}{\alpha}\left(\sqrt{\lambda + 1} - \sqrt{\lambda + \cos\theta_0}\right) \tag{2.106}$$

$$\alpha = tF(\beta, t) \tag{2.107}$$

$$\alpha = \sqrt{\frac{Pl^2}{EI}} \tag{2.108}$$

$$\lambda = \frac{k_0^2}{2\alpha^2} - \cos\theta_0 \tag{2.109}$$

$$\beta = \frac{\theta_0}{2} \tag{2.110}$$

$$t = \sqrt{\frac{2}{\lambda + 1}} \tag{2.111}$$

For $|\lambda| < 1$

$$\frac{a}{l} = \frac{1}{\alpha}[2E(\psi, r) - F(\psi, r)] \tag{2.112}$$

$$\frac{b}{l} = \frac{\sqrt{2}}{\alpha}\left(\sqrt{\lambda + 1} - \sqrt{\lambda + \cos\theta_0}\right) \tag{2.113}$$

$$\alpha = F(\psi, r) \tag{2.114}$$

$$\psi = \sin^{-1}\sqrt{\frac{1 - \cos\theta_0}{\lambda + 1}} \tag{2.115}$$

$$r = \sqrt{\frac{\lambda + 1}{2}} \tag{2.116}$$

2.6.2. Pseudo-Rigid-Body Model. Edwards (1996) and Mavanthoor (2002) developed the pseudo-rigid-body model of an initially-curved pinned-pinned segment. As the beam is symmetric, the complete segment is divided into two equivalent half-segments which are conceptually equivalent to initially-curved fixed-free segments. Figure 2.17 shows the PRBM of such a beam. Thus, the entire pinned-pinned segment may be represented in terms of an identical PRBM on each side of the beam's midpoint. The resistance of the beam to the deflection is modeled through nonlinear torsional springs which are identical due to symmetry. The resulting pseudo-rigid-body model is given in Figure 2.18.

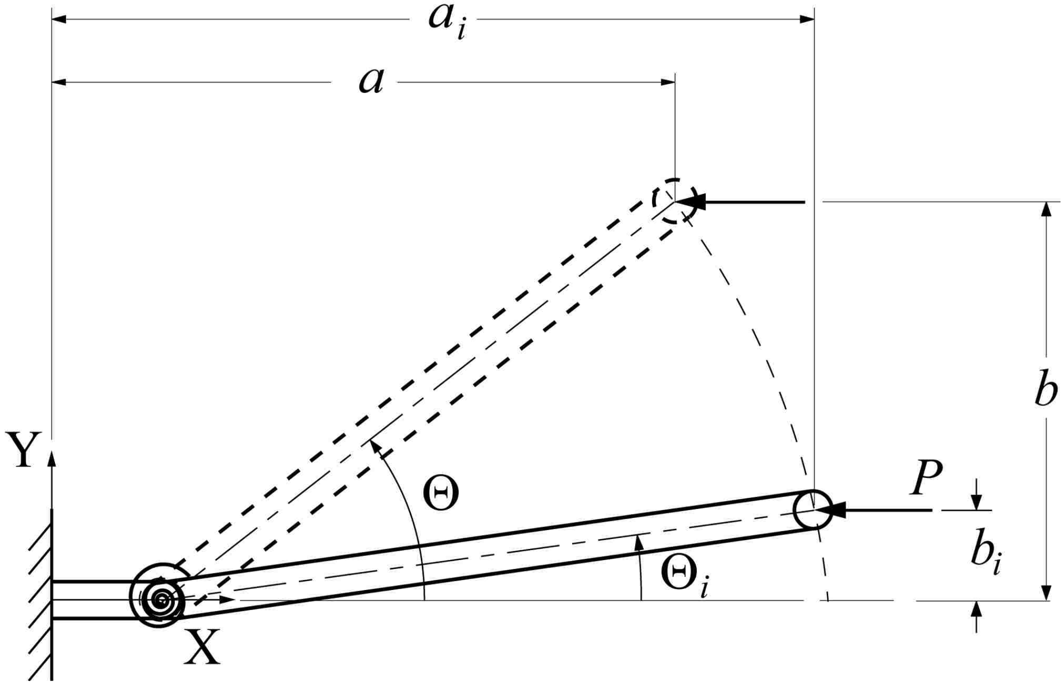

Figure 2.17. PRBM in Deflected Position

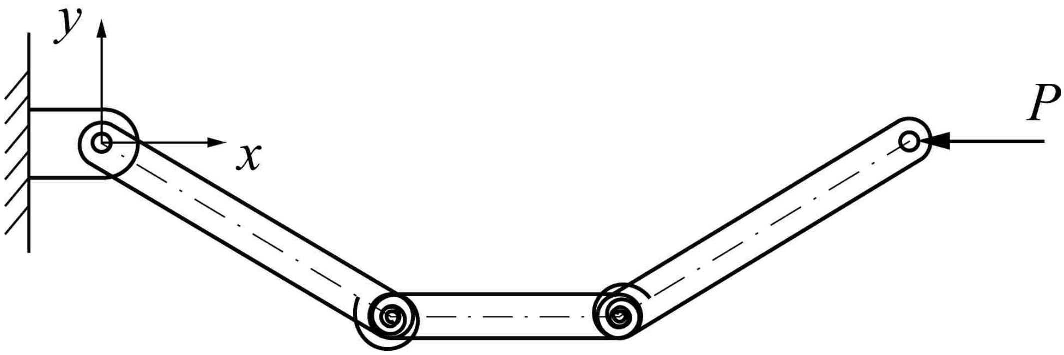

Figure 2.18. PRBM of Entire Pinned-Pinned Segment

The initial non-dimensional horizontal and vertical coordinates of the beam are,

$$a_i = \frac{l}{\kappa_0} \sin \kappa_0 \tag{2.117}$$

$$b_i = \frac{l}{\kappa_0} (1 - \cos \kappa_0) \tag{2.118}$$

And the initial value of the pseudo-rigid-body angle $\Theta_i$is,

$$\Theta_i = \tan^{-1} \frac{b_i}{a_i - l(1-\gamma)} \tag{2.119}$$

To account for the curvature, the length of rigid-body link is ρl where ρ is given by,

$$\rho = \left\{ \left[\frac{a_i}{l} - (1-\gamma) \right]^2 + \left(\frac{b_i}{l} \right)^2 \right\}^{\frac{1}{2}} \tag{2.120}$$

The non-dimensional tangential load factor α_t^2 is given by,

where,

$$\alpha_t^2 = \frac{F_t l^2}{EI} \tag{2.121}$$

$$F_t = F \sin(\Theta) \tag{2.122}$$

Also,

$$\alpha_t^2 = K_\Theta (\Theta - \Theta_i) \tag{2.123}$$

And the value of the stiffness of spring constant is given by,

$$K = \rho K_\Theta \frac{EI}{l} \tag{2.124}$$

The beam end coordinates are given by,

$$\frac{a}{l} = 1 - \gamma + \rho \cos \theta \tag{2.125}$$

$$\frac{b}{l} = \rho \sin \theta \tag{2.126}$$

2.7. FIXED-GUIDED COMPLIANT BEAM WITH AN INFLECTION POINT

A fixed-guided compliant beam of length l and flexural rigidity EI subject to end forces and moment is shown in Figure 2.19, where, P is the transverse force, nP the axial force, and M the moment.

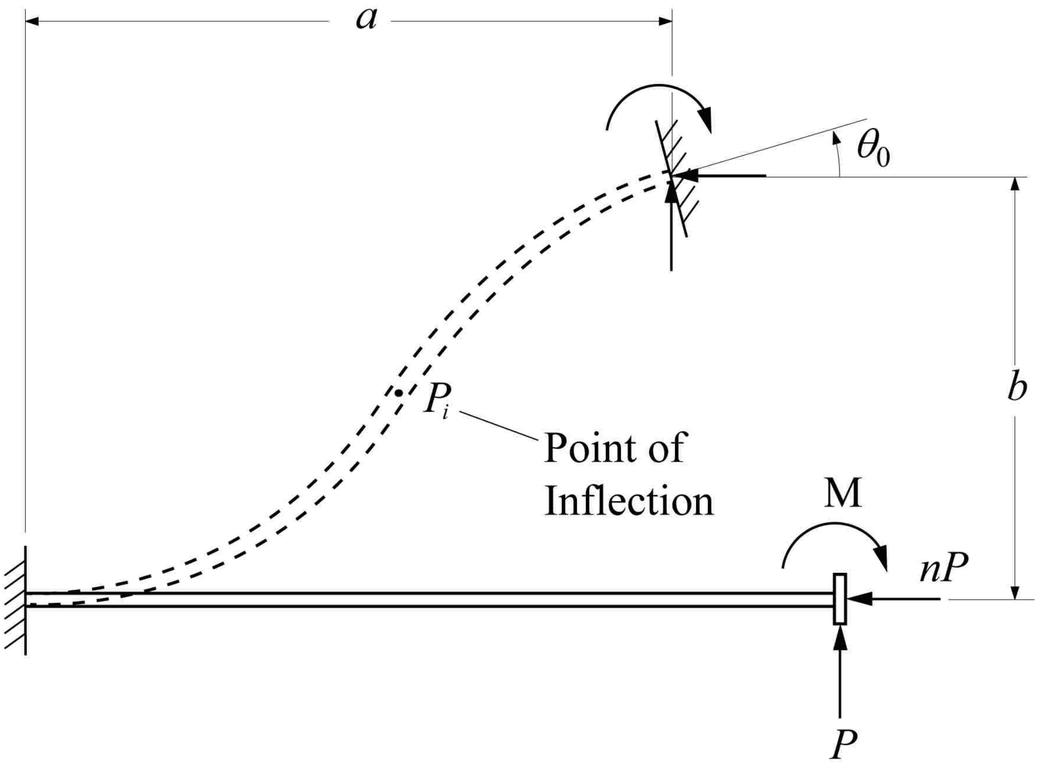

Figure 2.19. Fixed-Guided Compliant Beam with End Forces and Opposing Moment

2.7.1 Closed-Form Elliptic Integral Solution. Kimball (2002) developed the elliptic integral solutions for such beam. The equations for fixed guided beams with an inflection point are summarized below:

The non-dimensionalized beam tip deflections are given by,

$$\frac{a}{l} = \frac{1}{\alpha\eta^{5/2}}\left[-n\eta f^* + 2n\eta e^* + \sqrt{2\eta}c_x^*\right] \tag{2.127}$$

$$\frac{b}{l} = \frac{1}{\alpha\eta^{5/2}}\left[\eta f^* - 2\eta e^* + \sqrt{2\eta}c_y^*\right] \tag{2.128}$$

where,

$$\eta = \sqrt{1+n^2} \tag{2.129}$$

$$\alpha = \sqrt{\frac{Pl^2}{EI}} \tag{2.130}$$

$$\alpha = \sqrt{\frac{1}{\eta}f^*} \tag{2.131}$$

$$f^* = F(\gamma_1, k) + F(\gamma_2, k) \tag{2.132}$$

$$e^* = E(\gamma_1, k) + E(\gamma_2, k) \tag{2.133}$$

$$c_x^* = c_{x1} + c_{x2} \tag{2.134}$$

$$c_y^* = c_{y1} + c_{y2} \tag{2.135}$$

$$c_{x1} = -\sqrt{\lambda+\eta}\left(n\sqrt{\frac{\eta-n}{\eta+n}} - 1\right) \tag{2.136}$$

$$c_{x2} = -\sqrt{\kappa}\left(n\sqrt{\frac{\eta+\sin\theta_0 - n\cos\theta_0}{\eta-\sin\theta_0 + n\cos\theta_0}} - 1\right) \tag{2.137}$$

$$c_{y1} = \sqrt{\lambda+\eta}\left(n + \sqrt{\frac{\eta-n}{\eta+n}}\right) \tag{2.138}$$

$$c_{y2} = \sqrt{\kappa}\left(n + \sqrt{\frac{\eta + \sin\theta_0 - n\cos\theta_0}{\eta - \sin\theta_0 + n\cos\theta_0}}\right) \tag{2.139}$$

$$\gamma_1 = \sin^{-1}\sqrt{\frac{2\eta}{\lambda + \eta}\left(\frac{\lambda + n}{\eta + n}\right)} \tag{2.140}$$

$$\gamma_2 = \sin^{-1}\sqrt{\frac{2\eta}{\lambda + \eta}\left(\frac{\kappa}{\eta - \sin\theta_0 + n\cos\theta_0}\right)} \tag{2.141}$$

$$\kappa = \sqrt{\frac{\lambda + n}{2\eta}} \tag{2.142}$$

2.7.2. Pseudo-Rigid-Body Model. Figure 2.20Figure 2. (a) shows a fixed-guided compliant beam in its deformed state with a positive beam end angle, where P, nP, and M are the transverse force, the axial force, and the moment, respectively; a, b, and θ_0 are the beam end horizontal location, the vertical location and the angle, measured relative to the undeformed position of the beam end.

This type of loading will lead to an inflection point in the beam. Midha (2012) modeled the beam as two fixed-free compliant segments, pinned at the inflection point, P_i, which is characterized by zero curvature and, therefore, a zero moment. Both the compliant segments and their respective pseudo-rigid-body models are shown in Figure 2.20 (b), 2.20 (c), 2.20 (d) and 2.20 (e) respectively.

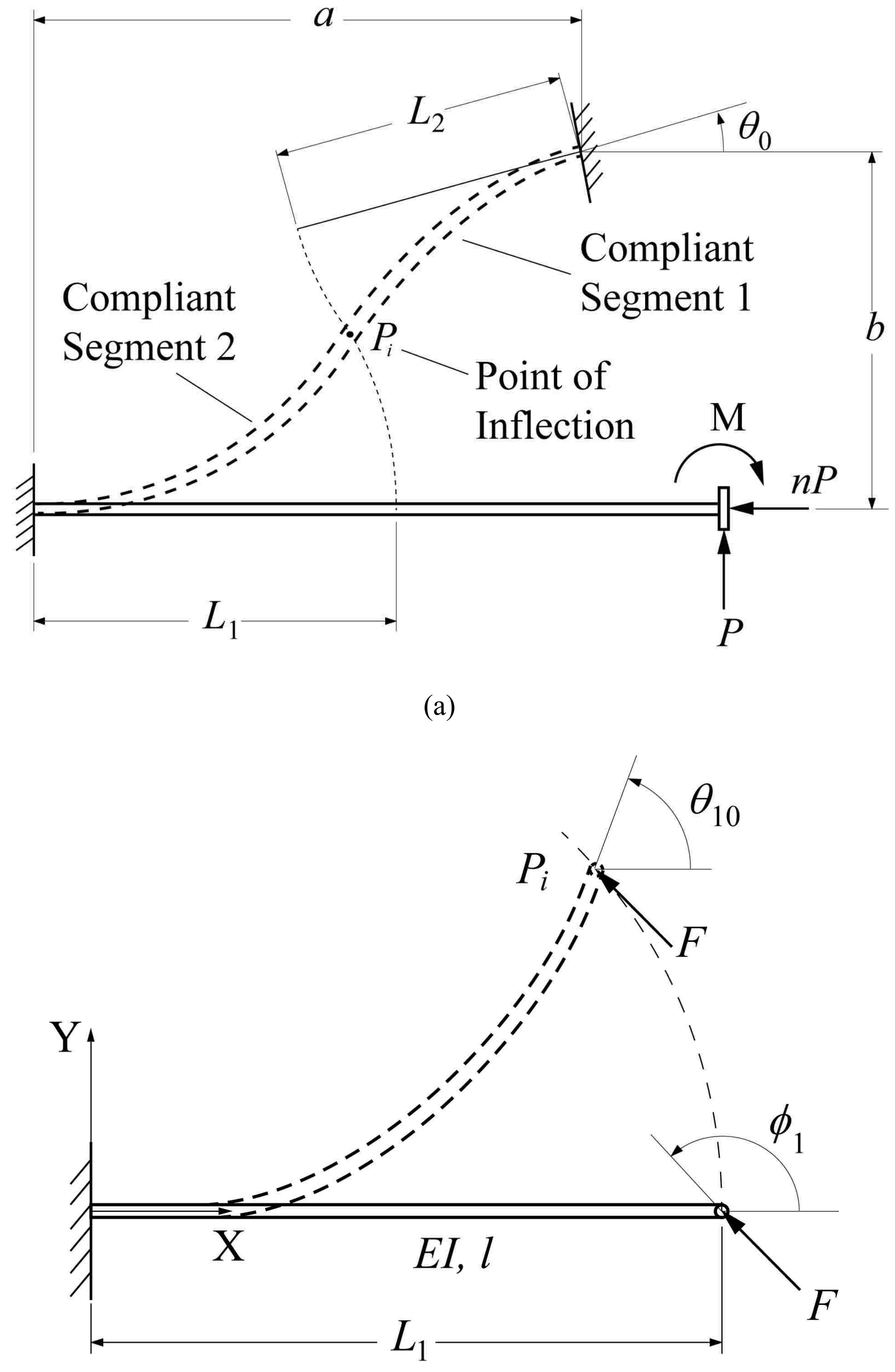

(a)

(b)

Figure 2.20. Deformed State of Fixed-Guided Compliant Beam (a) Considered as Two Compliant Segments; (b) Compliant Segment 1; (c) Compliant Segment 2; (d) PRBM of Compliant Segment 1; and (e) PRBM of Compliant Segment 2

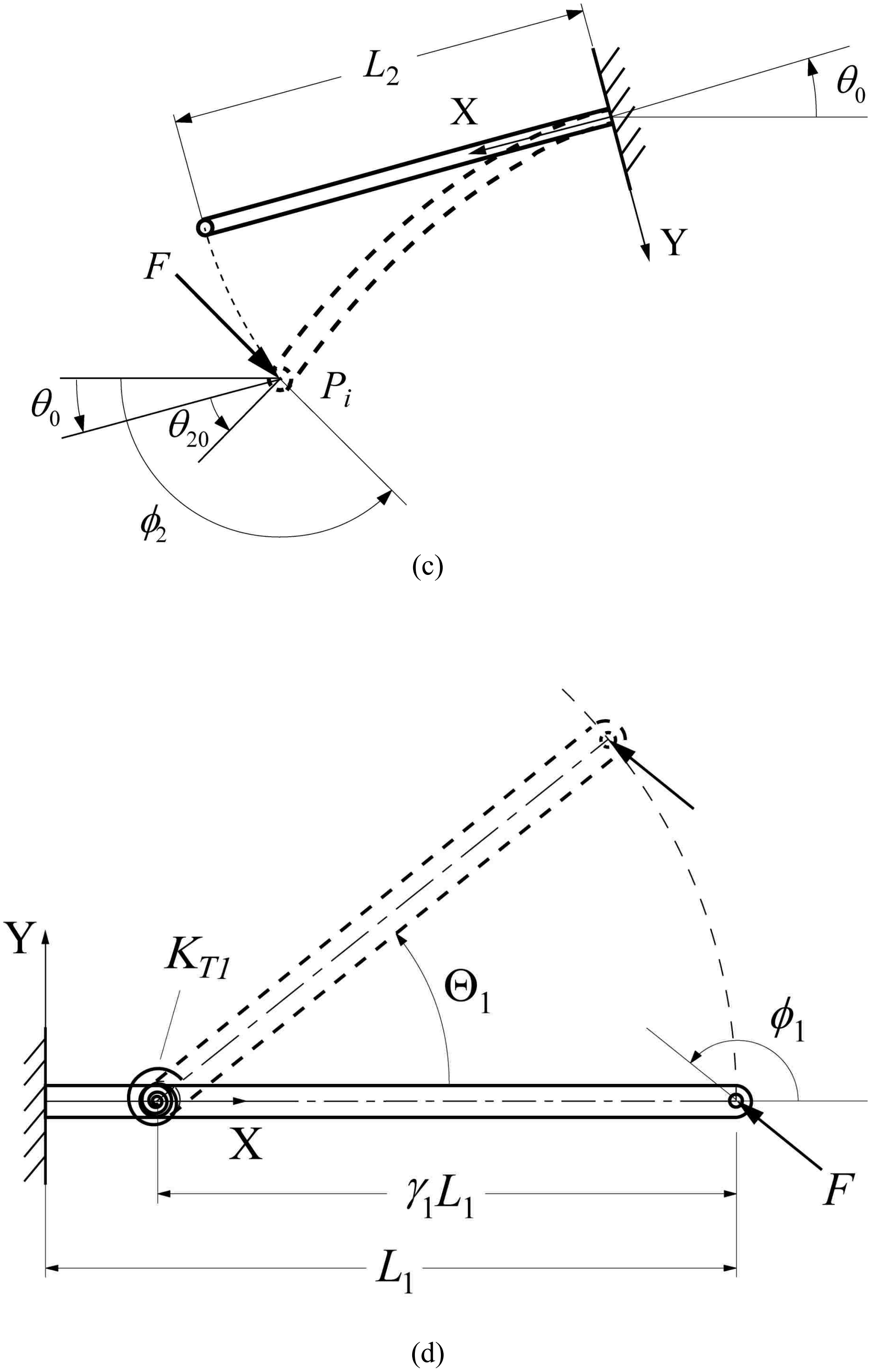

Figure 2.20. Deformed State of Fixed-Guided Compliant Beam (a) Considered as Two Compliant Segments; (b) Compliant Segment 1; (c) Compliant Segment 2; (d) PRBM of Compliant Segment 1; and (e) PRBM of Compliant Segment 2 (cont.)

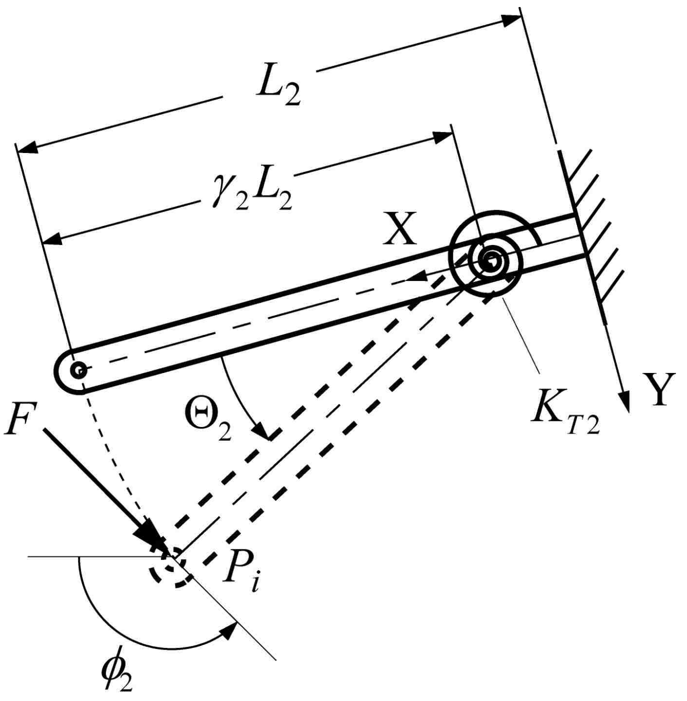

(e)

Figure 2.20. Deformed State of Fixed-Guided Compliant Beam (a) Considered as Two Compliant Segments; (b) Compliant Segment 1; (c) Compliant Segment 2; (d) PRBM of Compliant Segment 1; and (e) PRBM of Compliant Segment 2 (cont.)

The equations for the analysis of the fixed-guided compliant beam, subjected to a variety of beam end load and/or displacement boundary conditions are summarized below.

Based on the parametric expressions, equations (2.143) through (2.148) and are referred to as *Parametric Equations* (Midha, 2012).

$$\gamma_1 = 0.855651 - 0.016438 n_1, for\ -4\ < n_1\ \leq\ -1.5$$

$$\gamma_1 = 0.852138 - 0.018615 n_1, for\ -1.5\ < n_1\ \leq\ -0.5 \tag{2.143}$$

$$\gamma_1 = 0.851892 - 0.020805 n_1\ + 0.005867 n_1^2 - 0.000895 n_1^3 +$$

$$0.000069n_1^4 - 0.000002n_1^5, for\ -0.5\ < n_1\ \leq\ 10$$

$$\gamma_2 = 0.855651 - 0.016438n_2, for\ -4\ < n_2\ \leq\ -1.5$$

$$\gamma_2 = 0.852138 - 0.018615n_2, for\ -1.5\ < n_2\ \leq\ -0.5$$

$$\gamma_2 = 0.851892 - 0.020805n_2\ + 0.005867n_2^2 - 0.000895n_2^3 + \tag{2.144}$$

$$0.000069n_2^4 - 0.000002n_2^5, for\ -0.5\ < n_2\ \leq\ 10$$

$$c_{\theta_1} = 1.238945 + 0.012035n_1 + 0.00454n_1^2, for\ -4 < n_1 \leq\ -0.5$$

$$c_{\theta_1} = 1.238845 + 0.009113n_1 - 0.001929n_1^2 + 0.000191n_1^3 + \tag{2.145}$$

$$0.000390n_1^4 - 0.000013n_1^5, for\ -0.5\ < n_1\ \leq\ 10$$

$$c_{\theta_2} = 1.238945 + 0.012035n_2 + 0.00454n_2^2, for\ -4 < n_2 \leq\ -0.5$$

$$c_{\theta_2} = 1.238845 + 0.009113n_2 - 0.001929n_2^2 + 0.000191n_2^3 + \tag{2.146}$$

$$0.000390n_2^4 - 0.000013n_2^5\ , for\ -0.5\ < n_2 \leq\ 10$$

$$K_{\Theta_1} = 2.66041 - 0.069005n_1 - 0.002268n_1^2, for\ -4 < n_1 \leq\ -0.5$$

$$K_{\Theta_1} = 2.648834 - 0.074727n_1 + 0.026328n_1^2 - 0.004609n_1^3 + \tag{2.147}$$

$$0.000390n_1^4 - 0.000013n_1^5, for\ -0.5 < n_1 \leq\ 10$$

$$K_{\Theta_2} = 2.66041 - 0.069005n_2 - 0.002268n_2^2, for\ -4 < n_2 \leq\ -0.5$$

$$K_{\Theta_2} = 2.648834 - 0.074727n_2 + 0.026328n_2^2 - 0.004609n_2^3 + \tag{2.148}$$

$$0.000390n_2^4 - 0.000013n_2^5,\ for\ -0.5 < n_2 \leq\ 10$$

Equations (2.149) through (2.153) are derived from force and moment equilibrium using the free-body diagrams, and are referred to as the *Static Equilibrium Equations.*

$$\frac{FL_1^2}{EI}\sin\left(\phi_1-\frac{\theta_{10}}{c_{\theta_1}}\right)-K_{\Theta_1}\frac{\theta_{10}}{c_{\theta_1}}=0 \tag{2.149}$$

$$\frac{FL_2^2}{EI}\sin\left(\phi_2-\frac{\theta_{20}}{c_{\theta_2}}\right)-K_{\Theta_2}\frac{\theta_{20}}{c_{\theta_2}}=0 \tag{2.150}$$

$$n_1=\frac{-1}{tan\ (\phi_1)} \tag{2.151}$$

$$n_2=\frac{-1}{tan\ (\phi_2)} \tag{2.152}$$

$$M+\left\{[nPcos(\theta_0)-Psin(\theta_0)]\gamma_2L_2sin\left(\frac{\theta_{10}-\theta_0}{c_{\theta_2}}\right)\right\}+\left\{[Pcos(\theta_0)+\right.$$
$$nPsin(\theta 0)1-\gamma 2L2+\gamma 2L2sin\theta 10-\theta 0c\theta 2=0 \tag{2.153}$$

Equations (2.154) through (2.158) reflect constraints of length, slope, and displacements, and will be referred to as the *Compatibility Equations*.

$$L_1+L_2=L \tag{2.154}$$

$$\theta_{10}=\theta_{20}+\theta_0 \tag{2.155}$$

$$\phi_1=\phi_2+\theta_0 \tag{2.156}$$

$$b=\gamma_1L_1\sin\left(\frac{\theta_{10}}{c_{\theta_1}}\right)+\gamma_2L_2\sin\left(\frac{\theta_{20}}{c_{\theta_2}}+\theta_0\right)+(1-\gamma_2)L_2\sin\ (\theta_0) \tag{2.157}$$

$$a=(1-\gamma_1)L_1+\gamma_1L_1\cos\left(\frac{\theta_{10}}{c_{\theta_1}}\right)+\gamma_2L_2\cos\left(\frac{\theta_{20}}{c_{\theta_2}}+\theta_0\right)+(1-$$
$$\gamma 2L2cos\quad \theta 0 \tag{2.158}$$

2.8. SUMMARY

In this Section, two distinct methods of large deflection analysis for various boundary conditions and cases, adopted by various researchers for the design of compliant mechanisms, have been discussed. The closed form elliptic integral solutions for initially-straight and initially-curved small-length flexural pivot have been presented. The closed-form elliptic integral solutions provide the best accuracy to large deflection analysis; but their use is limited to relatively simple geometries and loadings. The pseudo-rigid-body models provide a simple and accurate method of analysis of the compliant mechanisms. The following section discusses an improved method to calculate the stiffness coefficient for a PRBM of a fixed-free compliant segment.

3. A METHOD FOR A MORE ACCURATE EVALUATION OF THE STIFFNESS COEFFICIENT IN PSEUDO-RIGID-BODY MODEL (PRBM)

3.1. INTRODUCTION

The previous section presented a brief overview of the large deflection analysis methods used in design of large deflection members. As discussed earlier, Howell (1991) developed the elliptic integral solution of a cantilever beam subject to a combination of end loads. Observing the nature of the beam end deflection paths obtained using elliptic integral solutions, the pseudo-rigid-body model was developed. This uses the parameterization of the beam end deflection path, beam end angular deflection and load-deflection relationships, in terms of the pseudo-rigid-body angle, Θ. The parametric expressions were developed through polynomial curve fit of the available data. Norton (1991) proposed a linear relation between the non-dimensional transverse force, α_t^2 and the pseudo-rigid-body angle Θ. He proposed a stiffness coefficient, K_Θ, as a function of the load factor, n, which is defined as the ratio of the applied horizontal force to the vertical force. However, the linear approximation yields certain amount of errors relative to the elliptic integral solutions when any arbitrary load and displacement boundary conditions are considered. This Section focuses on deriving improved expressions for K_Θ so as to reduce the error by investigating the effects of various parameters on K_Θ. Subsequently, a relationship among the non-dimensional transverse force α_t^2, pseudo-rigid-body model angle Θ and the load factor n is discovered. New parameterization expressions for K_Θ have been developed to show this relationship using a 3-dimensional curve fit among α_t^2, Θ and n.

Figure 3.1 shows a large deflection cantilever (fixed-free) beam subjected to non-follower horizontal and vertical end forces *nP* and *P*, respectively. Its equivalent pseudo-rigid-body model is shown in Figure 3.2. In a PRBM, a compliant beam is simulated by rigid segments that are connected by a pin joint (characteristic pivot) along the undeformed beam geometry. The characteristic radius factor γ is used to help define the lengths of the rigid segments. The beam end angle is denoted as θ_0, pseudo-rigid-body angle as Θ, vertical displaced position of the beam end as 'b', and horizontal displaced position as 'a' (Howell, 2001).

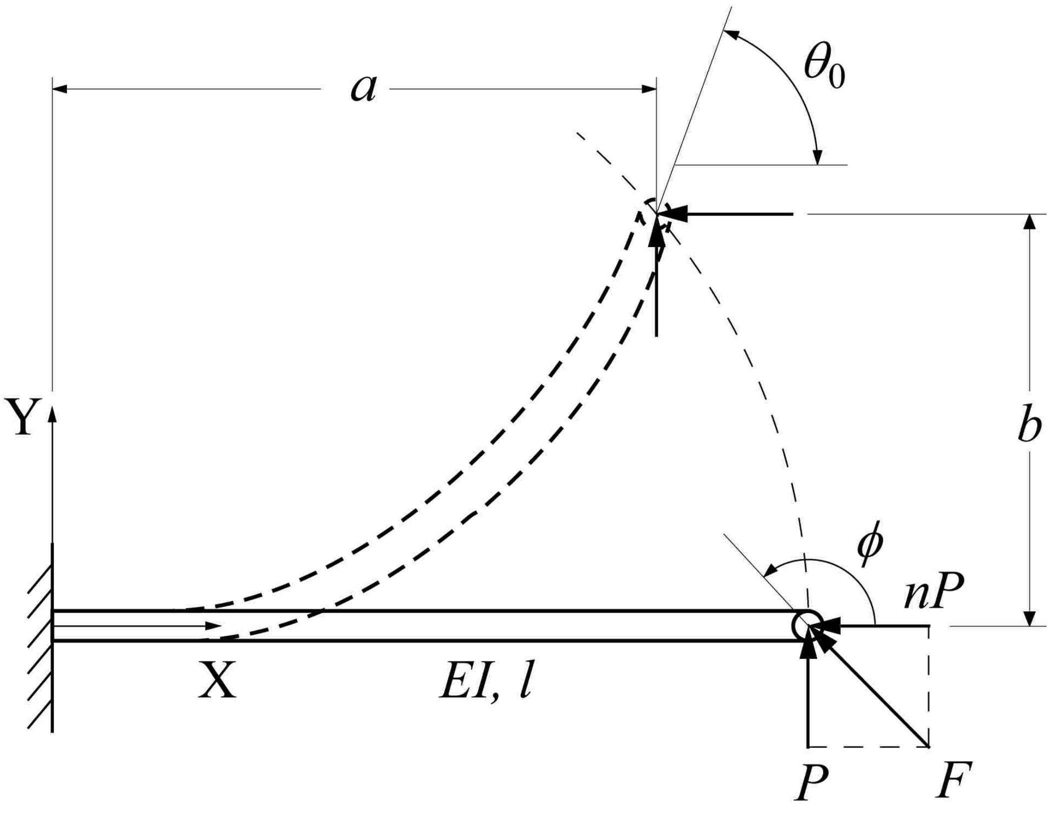

Figure 3.1. A Large-Deflection Cantilever Beam with End Forces nP and P

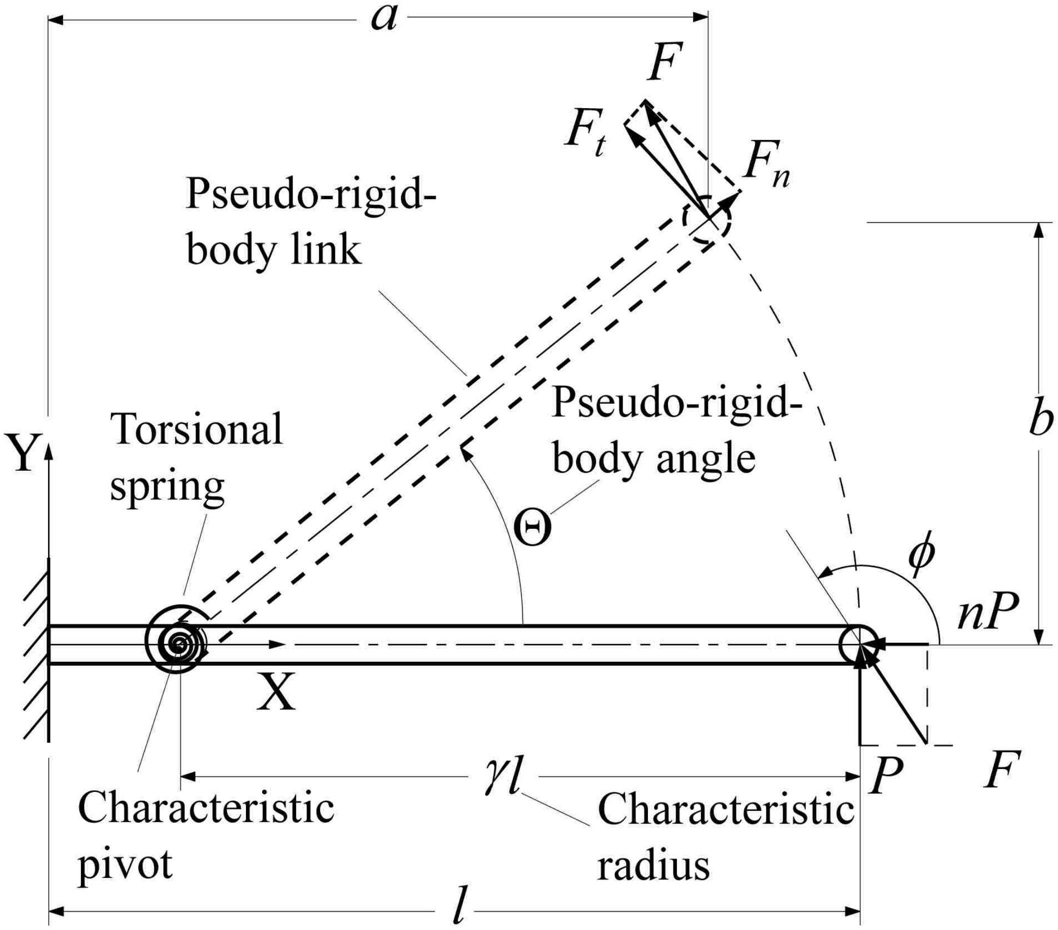

Figure 3.2. Pseudo-Rigid-Body Representation of a Large Deflection Beam

The force acting at the beam end, F, is given by,

$$F = \sqrt{P^2 + (np)^2} = \eta P \tag{3.1}$$

where,

$$\eta = \sqrt{1 + n^2} \tag{3.2}$$

The force contributing to the deflection of the pseudo-rigid link or the *active force* is the transverse or tangential component of the force *F*, and is given by:

$$F_t = F\sin(\phi - \Theta) \tag{3.3}$$

A non-dimensional representation of F_t is used as the non-dimensional transverse load index, α_t^2, as follows:

$$\alpha_t^2 = \frac{\eta P \sin(\phi - \Theta) l^2}{EI} \tag{3.4}$$

where,

$$\phi = \tan^{-1}\left(-\frac{1}{n}\right) \tag{3.5}$$

The pseudo-rigid-body angle is calculated as,

$$\Theta = \tan^{-1}\frac{b}{a - l(1-\gamma)} \tag{3.6}$$

where, *a* and *b* are the beam end coordinates calculated from elliptic integral solution using equations (2.5) and (2.6) respectively, γ is the characteristic radius factor calculated from equation (2.13) for given load index *n*. The equations for elliptic integral solution are briefly mentioned below, for details, kindly refer Section 2.2.1.

$$\frac{a}{l} = \frac{1}{\alpha\eta^{5/2}}\left\{-n\eta\left[\left[F\left[\frac{\pi}{2},t\right] - F[\gamma,t]\right] + 2\left[E[\gamma,t] - E\left[\frac{\pi}{2},t\right]\right]\right]\right. \\ \left. + \sqrt{2\eta(\eta+\lambda)}\cos\gamma\right\} \tag{2.5}$$

$$\frac{b}{1} = \frac{1}{\alpha\eta^{5/2}}\left\{\eta\left[\left[F\left[\frac{\pi}{2},t\right] - F[\gamma,t]\right] + 2\left[E[\gamma,t] - E\left[\frac{\pi}{2},t\right]\right]\right]\right. \\ \left. + n\sqrt{2\eta(\eta+\lambda)}\cos\gamma\right\} \tag{2.6}$$

where,

$$\alpha = \sqrt{\frac{Pl^2}{EI}} \tag{2.7}$$

$$\begin{aligned}
\gamma &= 0.855651 - 0.016438n, \quad \mathit{for}\ -4 < n \le -1.5 \\
\gamma &= 0.852138 - 0.01861n, \quad \mathit{for}\ -1.5 < n \le -0.5 \\
\gamma &= 0.851892 - 0.020805n + 0.005967n^2 - 0.000895n^3 \\
&\quad + 0.000069n^4 - 0.000002n^5, \quad \mathit{for}\ -0.5 < n \le 10
\end{aligned} \tag{2.13}$$

The compliant beam's resistance to deflection is modeled through a torsional spring located at the characteristic pivot. The value of the spring constant for the beam's equivalent pseudo-rigid-body model, K is determined (Howell, 2001) by combining the non-dimensional stiffness coefficient with the geometric and material properties of the beam as follows:

$$K = \gamma K_{\Theta} \frac{EI}{l} \tag{3.7}$$

The non-dimensional transverse load index, α_t^2 is assumed to have the following linear relation with the pseudo-rigid-body angle Θ, related through a parameter K_Θ termed as the stiffness coefficient:

$$\alpha_t^2 = K_{\Theta}\Theta \tag{3.8}$$

where, K_Θ is the stiffness coefficient, expressed in terms of the load factor *n*, as discussed in equation (2.16), expressed below:

$$\begin{aligned}
K_{\Theta} &= 2.66041 - 0.069005n - 0.002268n^2, \quad \mathit{for}\ -4 < n \le -0.5 \\
K_{\Theta} &= 2.648834 - 0.074727n + 0.026328n^2 - 0.004609n^3 + 0.00039n^4 \\
&\quad - 0.000013n^5, \quad \mathit{for}\ -0.5 < n \le 10
\end{aligned} \tag{2.16}$$

The assumption of the linear relation in equation (3.8) helps in simplification of the parametric expressions; however, it is not accurate for the entire range of deflection.

Figure 3.3 shows the plot of non-dimensional transverse load index α_t^2, versus the pseudo-rigid-body angle, Θ for $n = 0$. As seen in the figure, while the exact and the linear curve fits are close, there is room for improvement. The results will be accurate for those values of Θ where the linear curve fit is closer to the exact curve, and errors will be introduced as the linear curve deviates further from the exact curve.

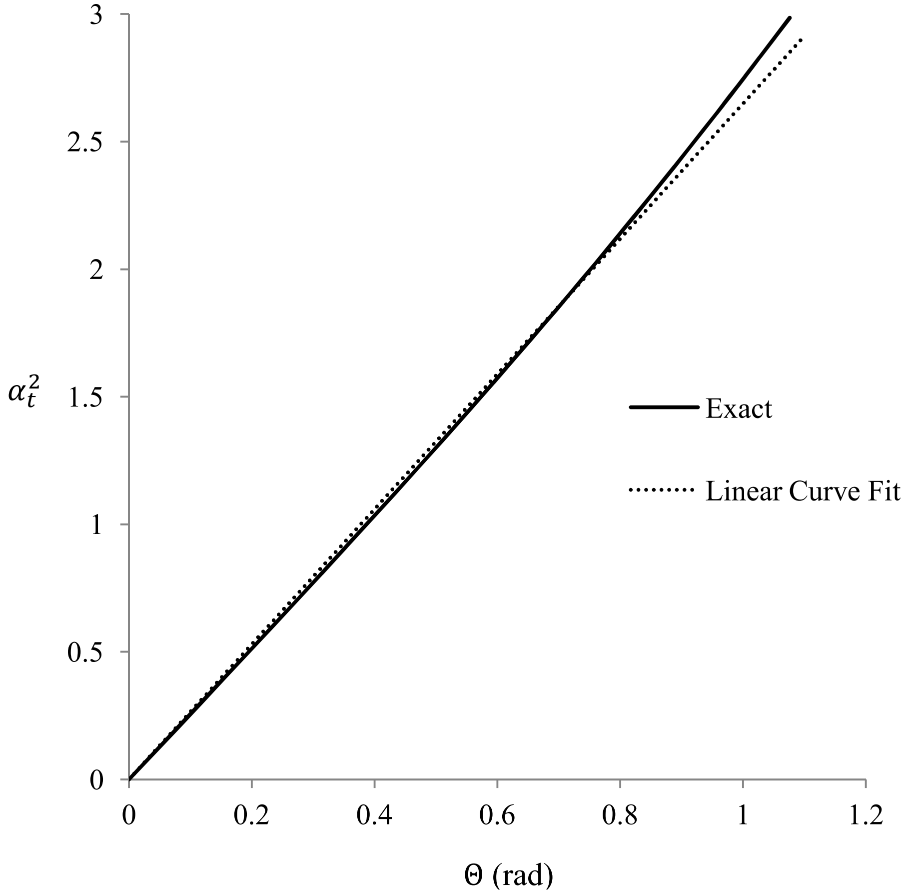

Figure 3.3. Non-Dimensional Tangential Force versus Pseudo-Rigid-Body Angle

In order to better understand the relation between α_t^2 and Θ for other load factors n, various plots are generated. Through these plots, it is observed that the non-dimensional transverse force α_t^2 is not only a function of the load factor n, but also a function of the pseudo-rigid-body angle Θ, i.e., the stiffness coefficient, K_Θ should be expressible as a function of the load factor n as well as the pseudo-rigid-body angle, Θ. The following sections discuss the improved expressions of the stiffness coefficient for a positive and negative load factor, i.e. for a compressive and tensile load, respectively, which yield significantly lower relative errors.

3.2. IMPROVED K_Θ EQUATION FOR COMPRESSIVE LOADS, OR POSITIVE LOAD FACTOR

Figure 3.4 shows the three-dimensional plot of the non-dimensional transverse force α_t^2, with the load factor n, and the pseudo-rigid-body angle Θ for compressive loads. A polynomial relation between α_t^2, n and Θ may be derived.

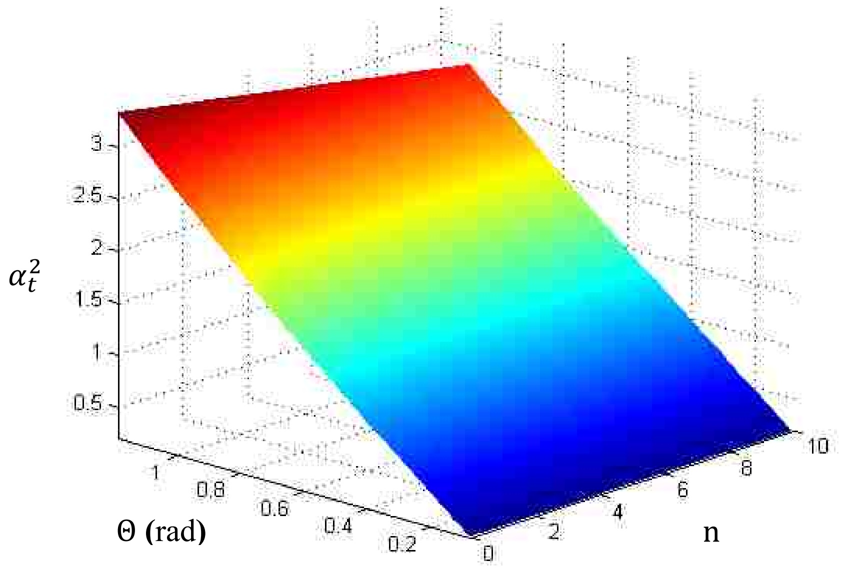

Figure 3.4. Three-Dimensional Plot of α_t^2, Θ and n for Compressive Loads

Figure 3.5 shows the flowchart of the procedure used to obtain the three-dimensional plot in Figure 3.4. The inputs to the code are the step size for the beam end angular deflection, $\Delta\theta_0$, step size for the load factor Δn, the range for the beam end angle and the load factor, and the geometric and material properties of the beam. With the beam end angle initially set to $\Delta\theta_0$ and the load factor initially set to n_i, the corresponding characteristic radius factor γ and the load angle ϕ are calculated using equation (2.3) and equation (3.5) respectively. The vertical and horizontal deflections are calculated using the elliptic integrals from equation (2.5) and equation (2.6). The pseudo-rigid-body angle Θ is calculated using equation (3.5) and the corresponding force P and the non-dimensional transverse force, α_t^2 is calculated using equation (2.7) and equation (3.4). The values of the non-dimensional transverse force α_t^2, the load factor n, and the pseudo-rigid-body angle Θ are recorded. The load factor is incremented by Δn and the process is continued till the load factor is less than the maximum value specified. When the maximum load factor is exceeded, the beam end angle is incremented by $\Delta\theta_0$, triggering the second loop. The entire process is stopped when the beam end angle exceeds the maximum value specified. The values used for $\Delta\theta_0$, Δn, n_i, n_{max} and θ_{0max} are 0.01 rad., 0.1, 0, 10 and 1.4 rad, respectively.

The three-dimensional plot is generated using the values recorded in the process above. A polynomial curve-fit procedure may now be utilized to express α_t^2 as a function of n and Θ. A commercially available software CurveExpert® is used to generate a polynomial full cubic 3D equation. Equation (3.9) expresses the cubic relation among α_t^2, n, and Θ.

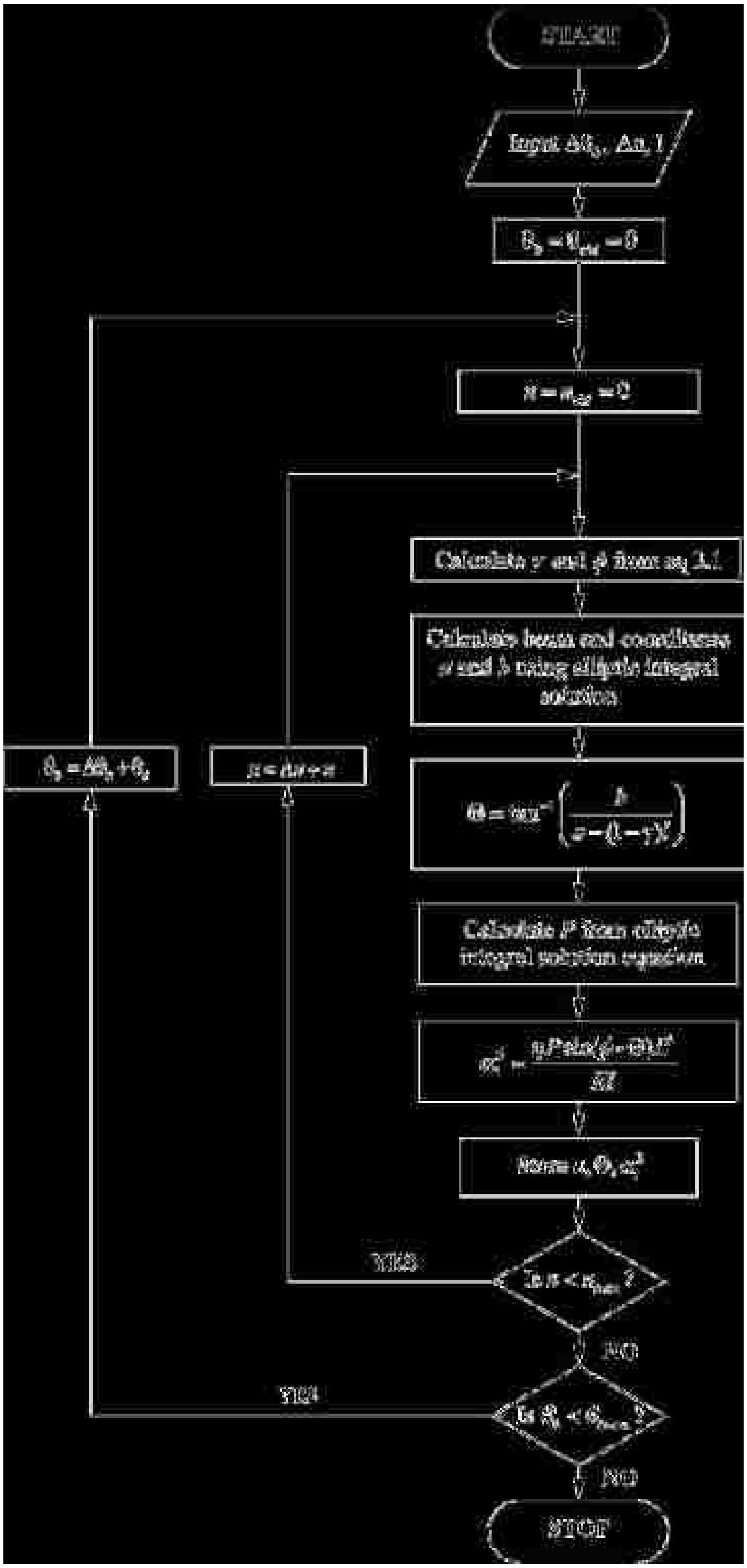

Figure 3.5. A Flow-Chart of Three-Dimensional Plot

$$\alpha_t^2 = (0.004233 - 0.012972n + 2.567095\Theta + 0.003993\mathrm{n}^2 - 0.037173\Theta^2 - 0.000297n^3 + 0.179970\Theta^3 - 0.034678n\Theta + 0.003467n^2\Theta - 0.009474\mathrm{n}\Theta^2), \qquad for\ 0 \leq n \leq 10, 0 \leq \Theta \leq 65^0 \tag{3.9}$$

In order to maintain the consistency with the conventional equations, the stiffness coefficient K_Θ is given by (Norton 1991),

$$\alpha_t^2 = K_\Theta \Theta \tag{3.10}$$

From equation (3.9) and equation (3.10), the improved equation for stiffness coefficient is obtained as:

$$K_\Theta = \frac{1}{\Theta}(0.004233 - 0.012972n + 2.567095\Theta + 0.003993\mathrm{n}^2 - 0.037173\Theta^2 - 0.000297n^3 + 0.179970\Theta^3 - 0.034678n\Theta + 0.003467n^2\Theta - 0.009474\mathrm{n}\Theta^2), \qquad for\ 0 \leq n \leq 10, 0 < \Theta \leq 65^0 \tag{3.11}$$

The square of the correlation coefficient $r^2$for the above relation is 0.9999 and the fitting target used is the lowest sum of squared relative error.

3.3. IMPROVED K_Θ EQUATION FOR TENSILE LOADS, OR NEGATIVE LOAD FACTOR

Figure 3.6 shows the 3-dimensional plot among the non-dimensional transverse force α_t^2, the load factor *n*, and the pseudo-rigid-body angle Θ for tensile loads. The plot is obtained using the same procedure mentioned above for tensile loads. The values used for $\Delta\theta_0$, Δn, n_i, n_{max} and θ_{0max} are 0.01 rad., 0.1, -4, 0 and ϕ rad, respectively. It should be noted that the maximum value of θ_0 i.e. θ_{0max} for tensile loads is equal to ϕ since the elliptic integral solutions are valid only when $\theta_0 < \phi$ (Howell 1991).

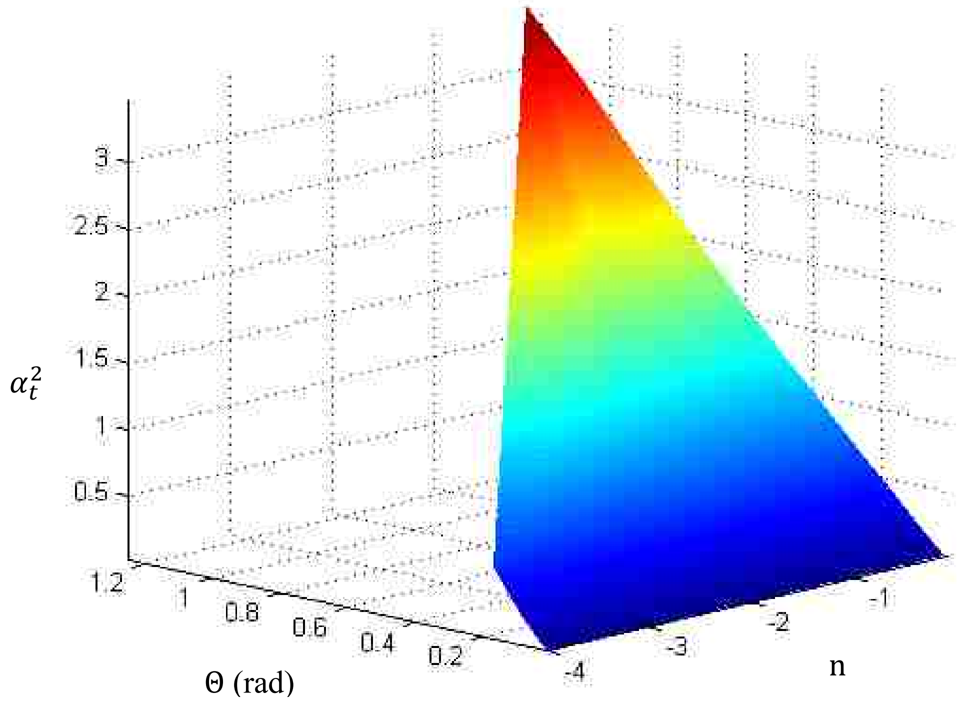

Figure 3.6. Three-Dimensional Plot of α_t^2, Θ and n for Tensile Loads

The data points are then used to derive the following expression for the stiffness coefficient K_Θ for tensile loads.

$$\begin{aligned} K_\Theta = \frac{1}{\Theta}(&0.000651 - 0.008244n + 2.544577\Theta - 0.004764\mathrm{n}^2 \\ &+ 0.071215\Theta^2 - 0.000104n^3 + 0.079696\Theta^3 + 0.069274n\Theta \\ &+ 0.061507n^2\Theta - 0.347588\mathrm{n}\Theta^2), \\ &for - 4 < n < 0, 0 < \Theta < 0.8\phi \end{aligned} \tag{3.12}$$

The square of the correlation coefficient r^2 for the above relation is 0.9998 and the fitting target used is the lowest sum of squared relative error.

Figure 3.8Figure 3.7 presents a vectorial illustration of the relative error calculation. Figure 3.8 (Howell, 2001) plots the relative error versus the pseudo-rigid-body angle Θ for $n = 0$ with comparing the old and new K_Θ equations, the plots for various values of n in the range -4 to 10 can be found in the Appendix A.

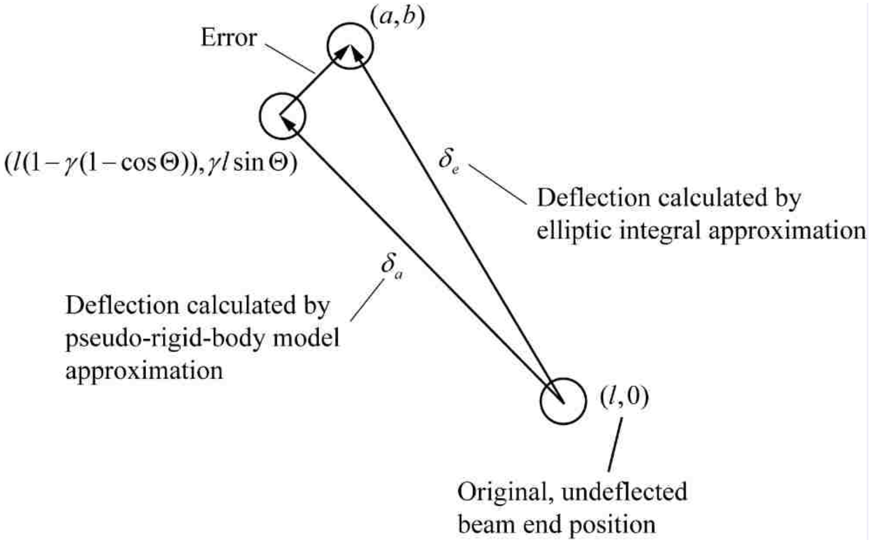

Figure 3.7. Calculation of Error in Approximating Beam End Deflection

The relative error is calculated as follows:

$$\frac{error}{\delta_e} = \frac{\sqrt{\left(\frac{a}{l} - (1 - \gamma(1 - \cos\Theta))\right)^2 + \left(\frac{b}{l} - \gamma\sin\Theta\right)^2}}{\sqrt{\left(1 - \frac{a}{l}\right)^2 + \left(\frac{b}{l}\right)^2}} \tag{3.13}$$

where, a and b are the horizontal and vertical beam end deflections, respectively, obtained using the elliptic integral approach. The pseudo-rigid-body angle Θ is calculated considering the curve fit equations for K_Θ.

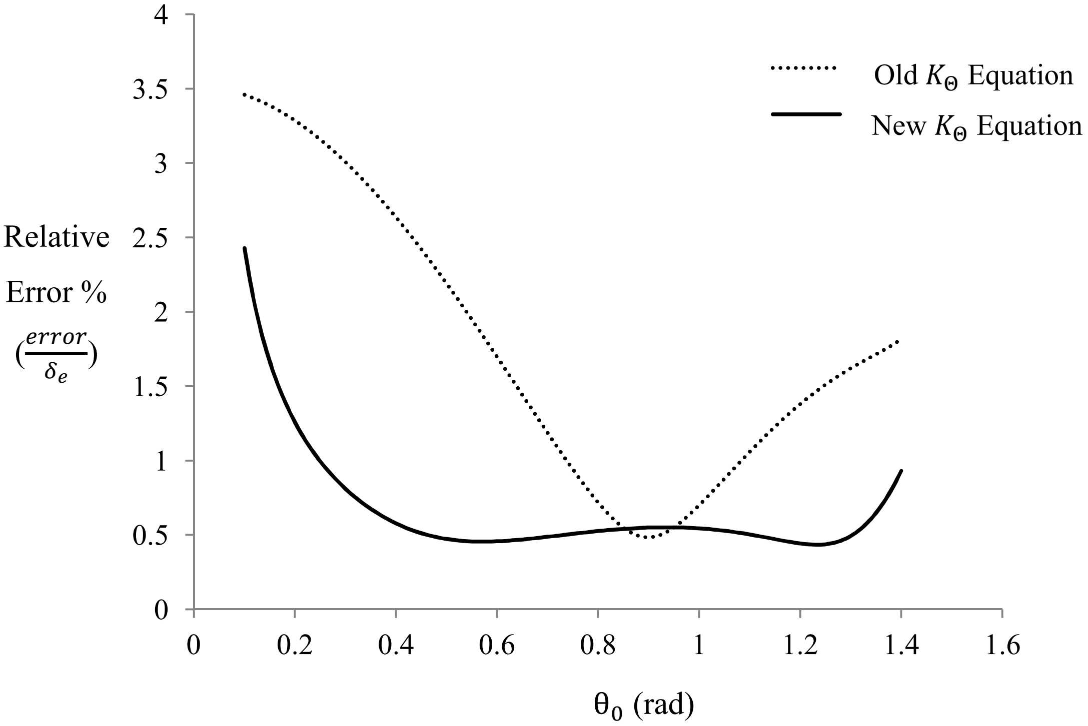

Figure 3.8. Relative Error versus Beam End Angle for $\mathrm{n} = 0$

It should be noted that the conventionally defined 0.5% relative error of PRBM is the error when pseudo-rigid-body angle Θ is calculated directly using the elliptic integral beam end coordinates and the characteristic radius factor without considering the curve fit for stiffness coefficient i.e. equation 3.8, however, the errors are significantly higher when the curve fits are considered.

It can be seen from Figure 3.8 that the relative error is significantly reduced with the improved K_Θ equations for most of the deflection range.

3.4. AVERAGE K_Θ VALUES

The equations discussed in above sections give fairly accurate results when compared with the elliptic integral solution, however, the equations are more complex. An average value of the stiffness coefficient, $K_{\Theta\mathrm{avg}}$, may be obtained for use in rough calculations or when high accuracy is not required. Howell (2003) calculated the average K_Θ value by integrating the K_Θ equation over a specified range of n. Here, the average K_Θ value is determined by taking the average of the K_Θ values calculated directly from the data points using the elliptic integral solutions. This way, the approximation of the curve fit equation is eliminated resulting in more accurate K_Θ values.

For the load factor range $-4.0 < n < 10.0$ or $14.04^0 < \phi < 174.3^0$, the average K_Θ value is determined to be,

$$K_{\Theta\mathrm{avg}} = 2.68 \tag{3.14}$$

Considering loads in only the most common range of $-0.5 < n < 1.0$ $63^0 < \phi < 135^0$, the average K_Θ value is found to be,

$$K_{\Theta\mathrm{avg}} = 2.62 \tag{3.15}$$

It should be noted that this approximation is valid only for a small range and should be used only for rough calculations.

3.5. EXAMPLE

A flexible steel beam with $E = 30 \times 10^6$ psi, length $l = 12$ in., width $w = 1.0$ in. and height $h = (1/32)$ in. is subjected to a vertical force of 0.4 lb and a horizontal compressive force of 0.8 lb. Calculate the horizontal and vertical deflections (*a* and *b*) using pseudo-rigid-body model and compare the solution with elliptic integrals.

Solution:

Given, $E = 30 \times 10^6$, $l = 12, w = 1.5, h = (1/32), P = 0.4$ lb, $nP = 0.8$ lb.

The moment of inertia, I, is

$$I = \frac{wh^3}{12} = \frac{(1.5) \times (1/32)^3}{12} = 2.543 \times 10^{-4} \text{ in}^4. \tag{3.16}$$

Load factor is,

$$n = \frac{nP}{P} = \frac{0.8}{0.4} = 2 \tag{3.17}$$

The load angle ϕ is,

$$\phi = \tan^{-1}\left(-\frac{1}{n}\right) = 2.6779 \text{ rad.} \tag{3.18}$$

Characteristic radius is found from equation (3.7) as,

$$\begin{aligned}\gamma = {} & 0.851892 - 0.020805n + 0.005967n^2 - 0.000895n^3 \\ & + 0.000069n^4 - 0.000002n^5\end{aligned} \tag{3.19}$$

$\gamma = 0.8276$

Old $K_\Theta$equation:

$$\begin{aligned}K_\Theta = {} & 2.648834 - 0.074727n + 0.026328n^2 - 0.004609n^3 \\ & + 0.00039n^4 - 0.000013n^5\end{aligned} \tag{3.20}$$

$K_\Theta = 2.5736$

Beam stiffness is,

$$K = \gamma K_{\Theta}\left(\frac{EI}{L}\right) = 13.5423 \quad (3.21)$$

The net force acting on the beam tip is:

$$F = \sqrt{P^2 + (np)^2} = 0.8944 \quad (3.22)$$

The angular position of the pseudo-rigid-body link is related to the input force by the relations:

$$T = K\Theta \quad (3.23)$$

$$T = F_t \gamma l \quad (3.24)$$

$$K = \gamma K_{\Theta}\left(\frac{EI}{L}\right) \quad (3.25)$$

$$F_t = F\sin(\phi - \Theta) \quad (3.26)$$

From equation (3.23) through (3.26) we get,

$$K\Theta = F_t \gamma l \quad (3.27)$$

$$K\Theta = F\sin(\phi - \Theta)\,\gamma l \quad (3.28)$$

Substituting values,

$$13.5423\Theta = 0.8944\sin(2.6779 - \Theta)\,0.8276 \times 12 \quad (3.29)$$

Solving equation (3.29) for Θ, we get,

$$\Theta = 0.5589 \text{ rad.} \quad (3.30)$$

The beam tip deflections are,

$$\mathrm{a} = \mathrm{L}\big(1 - \gamma(1 - \cos\Theta)\big) = 10.4887 \text{ in.} \quad (3.31)$$

$$\mathrm{b} = \mathrm{L}\gamma\sin\Theta = 5.2665 \text{ in.} \quad (3.32)$$

Using Improved K_{Θ} equation,

$$\begin{aligned} K_{\Theta} = \frac{1}{\Theta}(&0.004233 - 0.012972n + 2.5670950\Theta + 0.003993\mathrm{n}^2 \\ &- 0.0371730\Theta^2 - 0.000297n^3 + 0.1799700\Theta^3 - 0.034678n\Theta \\ &+ 0.003467n^2\Theta - 0.009474\mathrm{n}\Theta^2) \end{aligned} \tag{3.33}$$

$$K_{\Theta} = \frac{-0.0081 + 2.5116\Theta - 0.0561\Theta^2 + .17997\Theta^3}{\Theta} \tag{3.34}$$

Beam stiffness is,

$$K = 5.261980692\left(\frac{-0.0081 + 2.5116\Theta - 0.0561\Theta^2 + .17997\Theta^3}{\Theta}\right) \tag{3.35}$$

Substituting in equation (3.28),

$$\begin{aligned} &-0.0427 + 13.216\Theta - 0.2953\Theta^2 + 0.947\Theta^3 \\ &\qquad = 0.8944\sin(2.6779 - \Theta)\, 0.8276 \times 12 \end{aligned} \tag{3.36}$$

Solving equation (3.36) for Θ, we get,

$$\Theta = 0.57539 \text{ rad.} \tag{3.37}$$

The beam tip deflections are,

$$\mathrm{a} = \mathrm{L}\big(1 - \gamma(1 - \cos\Theta)\big) = 10.40 \text{ in.} \tag{3.38}$$

$$\mathrm{b} = \mathrm{L}\gamma\sin\Theta = 5.4044 \text{ in.} \tag{3.39}$$

Solving the above problem using the elliptic integral solution discussed briefly in Section 2 results in the following beam tip deflection:

$$\mathrm{a} = 10.3879 \text{ in.} \tag{3.40}$$

$$\mathrm{b} = 5.4071 \text{ in.} \tag{3.41}$$

Table 3.1 summarizes the above results comparing the old and the improved K_Θ equation in terms of the relative error calculated using equation 3.12

Table 3.1. Summary of Results

	Old K_Θ equation	**Improved K_Θ equation**	**Elliptic integral solution**
a	10.4887	10.40	10.3879
b	5.2665	5.4044	5.4071
Relative error (%)	3.0669	0.2343	

3.6. SUMMARY

In this Section, an improved method to calculate the stiffness coefficient (K_Θ) for pseudo-rigid-body model of a fixed-free beam has been presented. The improved expressions for the stiffness coefficient for compressive and tensile loads have been developed using a three-dimensional curve fit among non-dimensional transverse force α_t^2, the load factor *n*, and the pseudo-rigid-body angle Θ. An example has been presented showing the relative error comparison of the old and improved K_Θ expressions. The plots of relative error versus the pseudo-rigid-body angle for various values of *n* in the range -4 to 10 may be found in the Appendix A.

4. PSEUDO-RIGID-BODY MODEL FOR COMPLIANT SEGMENTS WITH INSERTS FOR VARIED BOUNDARY CONDITIONS AND CASES

4.1. INTRODUCTION

The popularity of compliant mechanisms has been growing since past few decades due to their inherent advantages and continuous development of simpler methods of analysis. The use of pseudo-rigid-body models has considerably simplified the analysis and synthesis of compliant mechanisms. Although offering number of advantages, their use has been limited due to current challenges in the material selection as the compliant links that are subject to large deflections for long periods or at high temperatures may experience stress relaxation or creep (Howell 2001). The creep is more prominent in polymers however, metals experience creep only at elevated temperatures. With ever increasing focus on the applications of compliant mechanisms, it is necessary to find alternatives to the existing materials usage and methods of fabrication.

This section presents a methodology for the development of PRBMs of compliant segments with inserts, i.e., a strong material inside outer layer of a softer material, to alleviate the creep and strength issues associated with conventional materials. The following sections discuss the closed-form elliptic integral and pseudo-rigid-body model solutions for standard compliant segments with inserts subjected to various boundary conditions.

4.2. EQUIVALENT SPRING STIFFNESS

The proposed PRBM and elliptic integral solutions are similar to the solutions for beams without insert material mentioned earlier. The flexible beam with insert is modeled assuming the two beams are in parallel; hence, the beam has equivalent stiffness equal to the addition of individual stiffness of the outer beam (casing) and the inner beam (insert). This is analogous to the deformation of two linear springs connected in parallel. Figure 4.1 shows a CAD model of a compliant segment with an insert showing the casing and insert material.

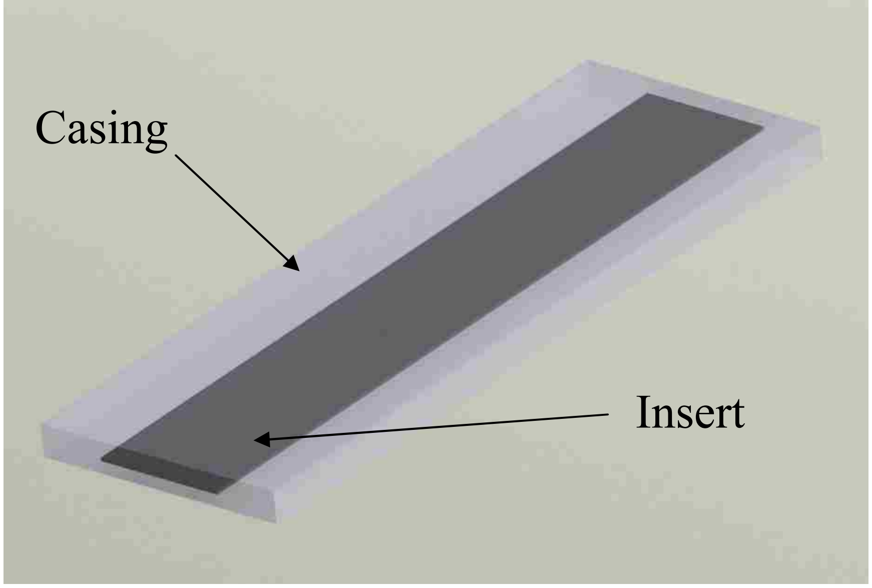

Figure 4.1. Compliant Segment with an Insert

Figure 4.2 shows two linear springs in parallel where, the deflection of each spring is equal to the total deflection of the system of springs.

$$x = x_1 = x_2 \tag{4.1}$$

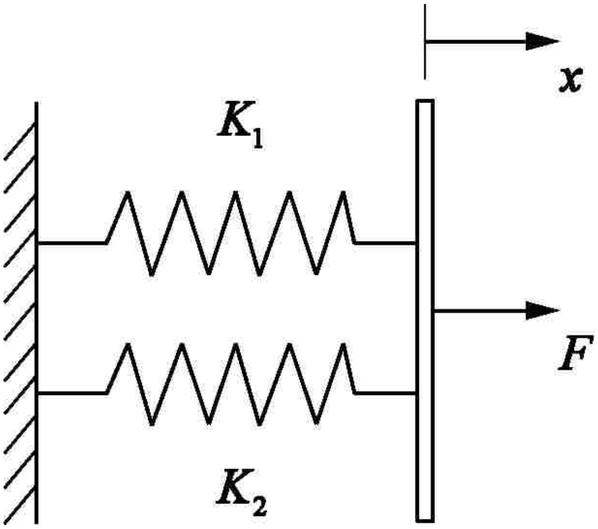

Figure 4.2. Linear Springs in Parallel

The total force applied is equal to the sum of the force exerted each spring. Therefore, the total force is,

$$F = K_1 x_1 + K_2 x_2 \tag{4.2}$$

where, K_1 and K_2 represent the stiffness, and x_1 and x_2 the displacement of each spring. The equivalent spring stiffness K^e is given by,

$$K^e = K_1 + K_2 \tag{4.3}$$

Equation (4.3) is used to heuristically estimate the stiffness of the equivalent torsional spring at the characteristic pivot of the equivalent pseudo-rigid-body model. The equivalent torsional spring models the combined resistance of the casing and the insert to the deflection.

The assumptions made in this effort are summarized below:

a) It is assumed that the casing and the insert are not bonded together, and therefore, each beam behaves independently under the applied load. The beam that is weaker in longitudinal bending (in this case, the plastic casing) will deform to the shape of the stronger beam (the metal insert) about its own neutral axis.

b) When loaded, each layer is free to slide on the adjacent layer(s), allowing slippage to occur. Assuming negligible errors, the effect of the slip is ignored. The surfaces are assumed to be smooth, therefore, the frictional resistance of the beams during deformation is considered negligible.

c) The casing and the insert are assumed to be of equal lengths subject to the same boundary conditions.

4.3. CANTILEVER BEAM WITH AN INSERT AND A FORCE AT THE FREE END

Figure 4.3 shows an initially-straight cantilever beam of length *l* with an outer beam (casing) of flexural rigidity $E_1 I_1$ and inner beam (insert) of flexural rigidity $E_2 I_2$ subjected to non-follower horizontal and vertical end forces *nP* and *P*, respectively. The combined end forces may be treated as a single force *F* acting at an angle ϕ, where $\phi = \tan^{-1}\left(-\frac{1}{n}\right)$.

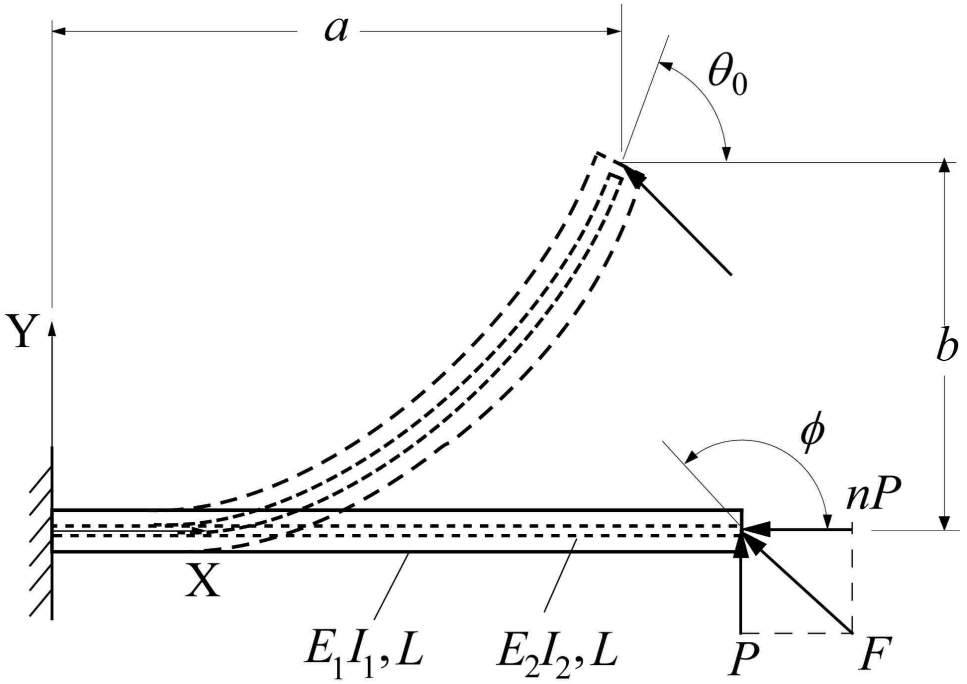

Figure 4.3. Initially-Straight Fixed-Free Beam with an Insert and End Forces

4.3.1. Closed-Form Elliptic Integral Solution. The tip deflection of the above cantilever beam can be shown to be:

For beam end angle $\theta_0 < \phi$,

$$\frac{a}{l} = \frac{1}{\alpha^e \eta^{5/2}} \left\{ -n\eta \left[\left[F\left[\frac{\pi}{2}, t\right] - F[\gamma, t] \right] + 2\left[E[\gamma, t] - E\left[\frac{\pi}{2}, t\right] \right] \right] + \sqrt{2\eta(\eta + \lambda)} \cos\gamma \right\} \tag{4.4}$$

$$\frac{b}{l} = \frac{1}{\alpha^e \eta^{5/2}} \left\{ \eta \left[\left[F\left[\frac{\pi}{2}, t\right] - F[\gamma, t] \right] + 2\left[E[\gamma, t] - E\left[\frac{\pi}{2}, t\right] \right] \right] + n\sqrt{2\eta(\eta + \lambda)} \cos\gamma \right\} \tag{4.5}$$

where,

$$\alpha^e = \frac{1}{\sqrt{\eta}}\left[F\left[\frac{\pi}{2}, t\right] - F[\gamma, t]\right] \tag{4.6}$$

$$\alpha^e = \sqrt{\frac{Pl^2}{E_1 I_1 + E_2 I_2}} \tag{4.7}$$

$$\lambda = \eta \cos(\theta_0 - \phi) \tag{4.8}$$

$$\eta = \sqrt{1 + n^2}; \qquad \phi = \tan^{-1}\left(-\frac{1}{n}\right) \tag{4.9}$$

$$\gamma = \sin^{-1}\sqrt{\frac{\eta - n}{\eta + \lambda}}; \qquad t = \sqrt{\frac{n + \lambda}{2\eta}} \tag{4.10}$$

Where, $F[\beta, q]$ and $E[\beta, q]$ denote the incomplete elliptic integrals of the first kind and second kind respectively, with amplitude β and modulus q, calculated as,

$$F[\beta, q] = \int_0^{\beta} \frac{d\theta}{\sqrt{1 - q^2 \sin^2 \theta}} \tag{4.11}$$

$$E[\beta, q] = \int_0^{\beta} \sqrt{1 - q^2 \sin^2 \theta}\, d\theta \tag{4.12}$$

4.3.2. Equivalent Pseudo-Rigid-Body Model. As discussed in Section 2, in a PRBM, a compliant beam is simulated by rigid segments that are connected by a pin joint (characteristic pivot). A torsional spring is placed at the pin joint to simulate the beam compliance. Figure 4.4 shows the equivalent pseudo-rigid-body model of shows an initially-straight cantilever beam of length *l* with casing of flexural rigidity $E_1 I_1$ and insert of flexural rigidity $E_2 I_2$ subjected to non-follower horizontal and vertical end forces *nP* and *P*, respectively.

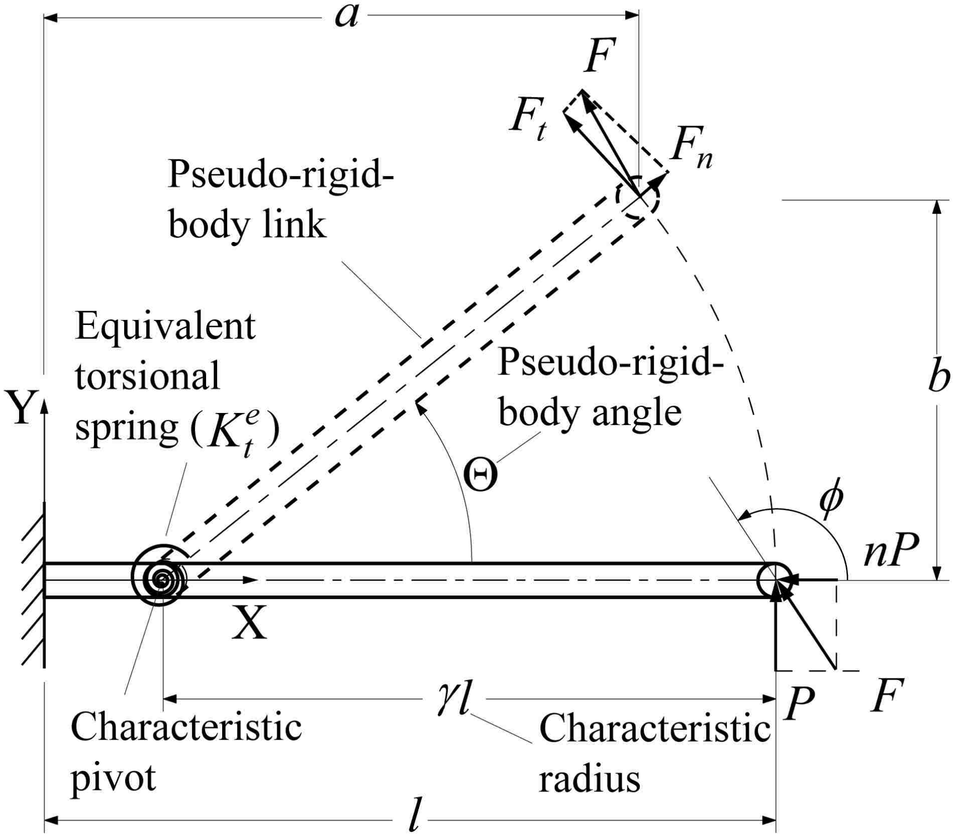

Figure 4.4. PRBM of an Initially-Straight Fixed-Free Beam with an Insert

The torsional spring moment at the characteristic pivot is given by the following relationship:

$$K_t^e \Theta = F \sin(\phi - \Theta)\, \gamma l \tag{4.13}$$

Where, K_t^e is the equivalent stiffness of the torsional spring, Θ is the pseudo-rigid-body angle, F_t is the transverse force and γl the characteristic radius. The characteristic radius factor γ is expressed as a function of the load factor n by the following relation:

$$\gamma = 0.855651 - 0.016438n, \text{ for } -4 < n \leq -1.5 \tag{4.14}$$

$$\gamma = 0.852138 - 0.01861n, \text{ for } -1.5 < n \leq -0.5$$

$$\gamma = 0.851892 - 0.020805n + 0.005967n^2 - 0.000895n^3 + 0.000069n^4 - 0.000002n^5, \text{ for } -0.5 < n \leq 10$$

As it can be seen in Figure 4.4, both the casing and the insert will have the same angular deflection Θ.

therefore, $$\Theta = \Theta_1 = \Theta_2 \tag{4.15}$$

Based on the similarity between equation (4.1) and (4.15), the equivalent torsional spring at the characteristic pivot of the equivalent PRBM is approximated by two linear torsional springs connected in parallel with stiffness values K_1 and K_2 where, $K_1$is the stiffness of the casing and K_2 is the stiffness of the insert. The equivalent torque of the torsional spring is given by,

$$K_t^e \Theta = K_1 \Theta + K_2 \Theta \tag{4.16}$$

therefore, $$K_t^e = K_1 + K_2 \tag{4.17}$$

where,

$$K_1 = K_\Theta \gamma \frac{E_1 I_1}{l} \tag{4.18}$$

and

$$K_2 = K_\Theta \gamma \frac{E_2 I_2}{l} \tag{4.19}$$

therefore, $$K_t^e = K_\Theta \gamma \left(\frac{E_1 I_1 + E_2 I_2}{l} \right) \tag{4.20}$$

The beam stiffness coefficient K_Θ is calculated using the following improved equations discussed in Section 3:

$$K_\Theta = \frac{1}{\Theta}(0.004233 - 0.012972n + 2.567095\Theta + 0.003993\mathrm{n}^2$$

$$- 0.037173\Theta^2 - 0.000297n^3 + 0.179970\Theta^3 - 0.034678n\Theta$$

$$+ 0.003467n^2\Theta - 0.009474\mathrm{n}\Theta^2),$$

$$for\ 0 \leq n \leq 10, 0 < \Theta \leq 65^0$$

$$K_\Theta = \frac{1}{\Theta}(0.000651 - 0.008244n + 2.544577\Theta \tag{4.21}$$

$$- 0.004764\mathrm{n}^2 + 0.071215\Theta^2 - 0.000104n^3$$

$$+ 0.079696\Theta^3 + 0.069274n\Theta + 0.061507n^2\Theta$$

$$- 0.347588\mathrm{n}\Theta^2),$$

$$for - 4 < n < 0, 0 < \Theta < 0.8\phi$$

Beam end angle can be related to pseudo-rigid-body angle through the parametric angle coefficient c_θ (Howell, 2001) such that,

$$\theta_0 = \mathrm{c}_\theta\Theta \tag{4.22}$$

The parametric angle coefficient c_θ is given as:

$$c_\theta = 1.238945 + 0.012035n + 0.00454n^2, for\ -4 < n \leq -0.5$$

$$c_\theta = 1.238845 + 0.009113n - 0.001929n^2 + 0.000191n^3 + 0.00039n^4 \tag{4.23}$$

$$- 0.000013n^5, \text{ for } -0.5 < n \leq 10$$

The beam end coordinates are given by,

$$\frac{a}{l} = 1 - \gamma(1 - \cos\Theta) \tag{4.24}$$

$$\frac{b}{l} = \gamma \sin\Theta \tag{4.25}$$

Above mentioned equations are validated with commercially available finite element software ABAQUS®. Figure 4.5 shows the plot of the non-dimensionalized beam tip deflection $\left(\frac{a}{l}, \frac{b}{l}\right)$ calculated from the elliptic integral solution equations (4.4) and (4.5), pseudo-rigid-body model equations (4.24) and (4.25) and ABAQUS®.

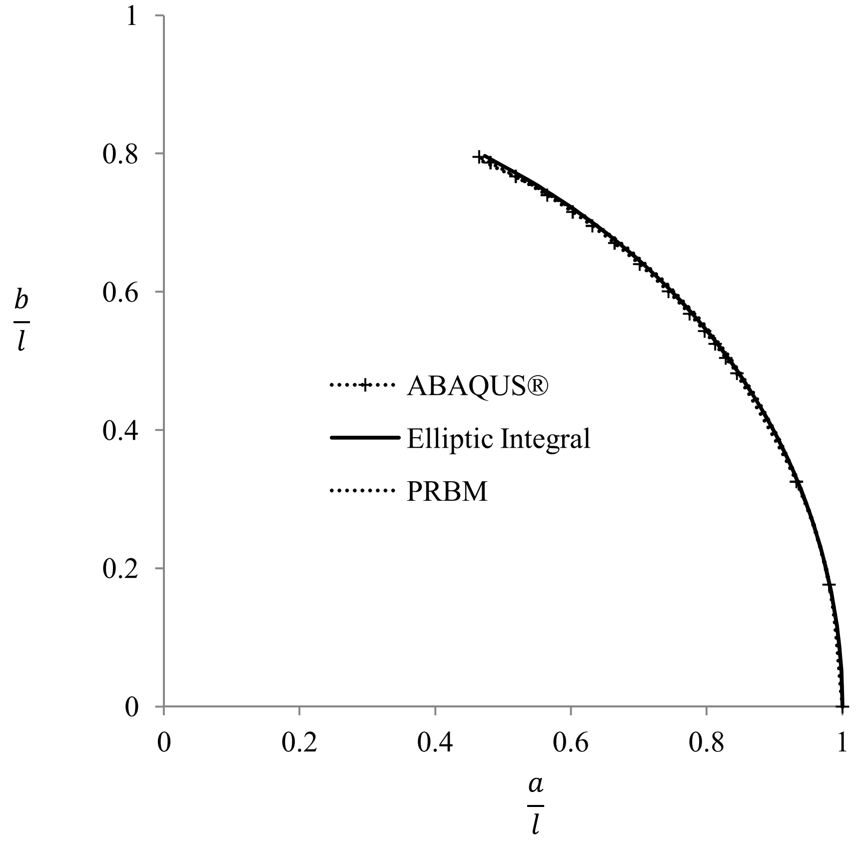

Figure 4.5. Beam End Deflection Comparison of an Initially-Straight Fixed-Free Beam with an Insert for $\text{n} = 0$

4.3.3. Stress Calculations. As discussed in equation (4.2), the total force applied will be divided into two forces at the casing and the insert as P_1 and P_2 respectively. The stress at the top and bottom of the casing may be given by,

$$\sigma_{1_{top}} = \frac{-(P_1 a + nP_1 b)c_1}{I_1} - \frac{nP_1}{A_1} \tag{4.26}$$

$$\sigma_{1_{bottom}} = \frac{(P_1 a + nP_1 b)c_1}{I_1} - \frac{nP_1}{A_1} \tag{4.27}$$

The stress at the top and bottom of the insert may be given by,

$$\sigma_{2_{top}} = \frac{-(P_2 a + nP_2 b)c_2}{I_2} - \frac{nP_2}{A_2} \tag{4.28}$$

$$\sigma_{2_{bottom}} = \frac{P_2 a + nP_2 b)c_2}{I_2} - \frac{nP_2}{A_2} \tag{4.29}$$

where, A_1 and A_2 are the areas cross-section, and c_1 and c_2 are the maximum distances from the neutral axes of the beam and insert respectively. Also,

$$P_1 = \frac{K_1 \Theta}{\eta \gamma l \sin(\phi - \Theta)} \tag{4.30}$$

$$P_2 = \frac{K_2 \Theta}{\eta \gamma l \sin(\phi - \Theta)} \tag{4.31}$$

4.4. INITIALLY-CURVED FIXED FREE BEAM WITH AN INSERT

Figure 4.6 shows an initially-curved cantilever beam of length *l* with casing of flexural rigidity $E_1 I_1$ and insert of flexural rigidity $E_2 I_2$ subjected to non-follower horizontal and vertical end forces *nP* and *P*, respectively.

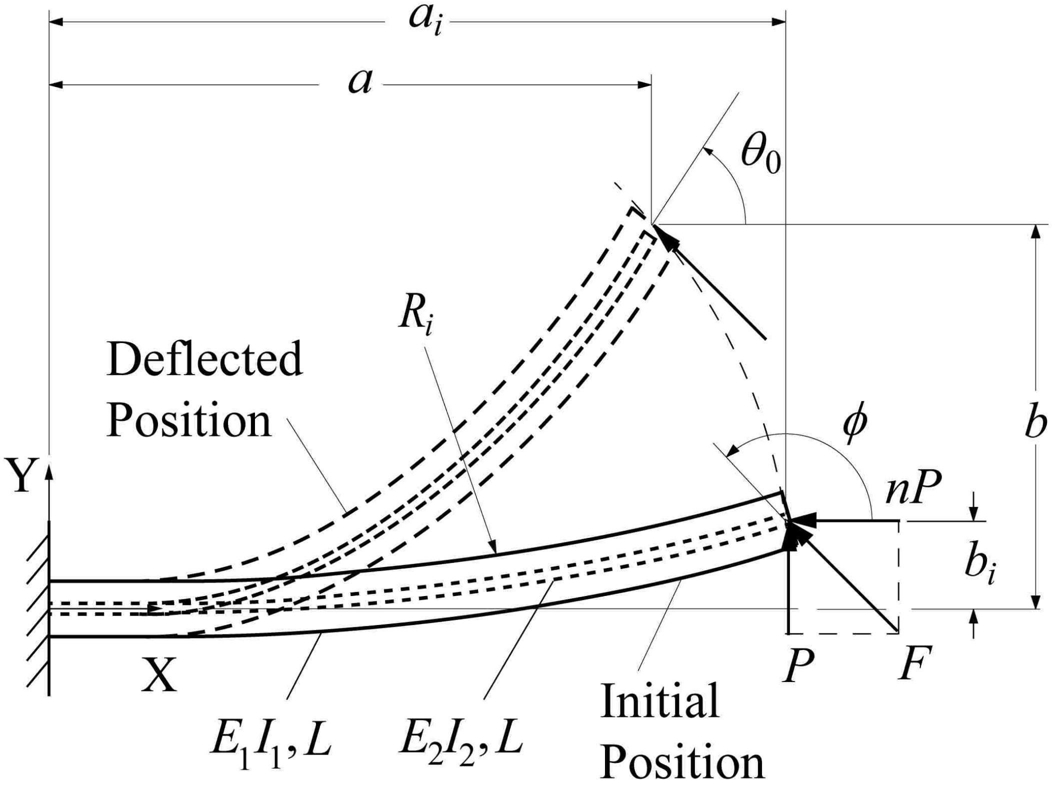

Figure 4.6. Initially-Curved Fixed-Free Beam with an Insert Subject to End Forces

The beams have an initial radius of curvature R_i and hence a curvature of $1/R_i$. The initial curvature can be related to the beam length using the non-dimensional parameterκ_0 as,

$$\kappa_0 = \frac{l}{R_i} \tag{4.32}$$

4.4.1. Closed-Form Elliptic Integral Solution. The beam end deflections may be given by following equations:

$$\eta = \sqrt{1 + n^2} \tag{4.33}$$

$$\phi = \tan^{-1}\left(-\frac{1}{n}\right) \tag{4.34}$$

for $|\lambda| < \eta; \phi - \cos^{-1}(-\lambda/n) \leq -\theta_0 < \phi'$ and $\alpha \neq 0$,

$$\alpha^e = \frac{1}{\sqrt{\eta}}[F[\gamma_2, t] - F[\gamma_1, t]] \tag{4.35}$$

$$\begin{aligned} \frac{\mathrm{a}}{l} = \frac{1}{\alpha^e \eta^{5/2}} \Big\{ &-n\eta \Big[[F[\gamma_2, t] - F[\gamma_1, t]] + 2\big[E[\gamma_1, t] - E[\gamma_2, t]\big] \Big] \\ &+ \sqrt{2\eta(\eta + \lambda)}(\cos\gamma_1 - \cos\gamma_2) \Big\} \end{aligned} \tag{4.36}$$

$$\begin{aligned} \frac{b}{l} = \frac{1}{\alpha^e \eta^{5/2}} \Big\{ &\eta \Big[[F[\gamma_2, t] - F[\gamma_1, t]] + 2\big[E[\gamma_1, t] - E[\gamma_2, t]\big] \Big] \\ &+ n\sqrt{2\eta(\eta + \lambda)}(\cos\gamma_1 - \cos\gamma_2) \Big\} \end{aligned} \tag{4.37}$$

for $\lambda > \eta; \phi - \pi \leq -\theta_0$

$$\alpha^e = \sqrt{\frac{2}{\lambda + \eta}}[F[\psi_2, r] - F[\psi_1, r]] \tag{4.38}$$

$$\begin{aligned} \frac{a}{l} = \frac{\sqrt{2(\eta + \lambda)}}{\alpha^e \eta^2} \Bigg\{ &-n \left[\frac{\lambda}{\eta + \lambda}[F[\psi_2, r] - F[\psi_1, r]] + \big[E[\psi_1, r] - E[\psi_2, r]\big] \right] \\ &+ \left[\sqrt{1 - \frac{\eta - n}{\eta + \lambda}} - \sqrt{1 - \frac{\eta + \sin\theta_0 - n\cos\theta_0}{\eta + \lambda}} \right] \Bigg\} \end{aligned} \tag{4.39}$$

$$\begin{aligned} \frac{b}{l} = \frac{\sqrt{2(\eta + \lambda)}}{\alpha^e \eta^2} \Bigg\{ &\frac{\lambda}{\eta + \lambda}[F[\psi_2, r] - F[\psi_1, r]] + \big[E[\psi_1, r] - E[\psi_2, r]\big] \\ &+ n \left[\sqrt{1 - \frac{\eta - n}{\eta + \lambda}} - \sqrt{1 - \frac{\eta + \sin\theta_0 - n\cos\theta_0}{\eta + \lambda}} \right] \Bigg\} \end{aligned} \tag{4.40}$$

where,

$$\lambda = \frac{1}{2}\left(\frac{\kappa_0}{\alpha^e}\right)^2 + \sin\theta_0 - n\cos\theta_0 \tag{4.41}$$

$$\eta = \sqrt{1+n^2}; \qquad \phi' = \tan^{-1}\left(\frac{1}{n}\right) \tag{4.42}$$

$$\alpha^e = \sqrt{\frac{Pl^2}{E_1I_1 + E_2I_2}} \tag{4.43}$$

$$\gamma_1 = \sin^{-1}\sqrt{\frac{\eta - n}{\eta + \lambda}}; \quad \gamma_2 = \sin^{-1}\sqrt{\frac{\eta + \sin\theta_0 - n\cos\theta_0}{\eta + \lambda}} \tag{4.44}$$

$$\psi_1 = \sin^{-1}\sqrt{\frac{\eta - n}{2\eta}}; \quad \psi_2 = \sin^{-1}\sqrt{\frac{\eta + \sin\theta_0 - n\cos\theta_0}{\psi_1}} \tag{4.45}$$

$$t = \sqrt{\frac{\eta + \lambda}{2\eta}}; \qquad r = \sqrt{\frac{2\eta}{\eta + \lambda}} \tag{4.46}$$

4.4.2. Equivalent Pseudo-Rigid-Body Model. Figure 4.7 shows the equivalent pseudo-rigid-body-model of an initially-curved cantilever beam of length l with casing of flexural rigidity E_1I_1 and insert of flexural rigidity E_2I_2 subjected to combined end forces P and nP . The equivalent characteristic radius length γl is measured along the beam as if it were initially straight. The combined end forces may be treated as a single force F acting at an angle ϕ, where $\phi = \tan^{-1}\left(-\frac{1}{n}\right)$.

The initial beam end coordinates a_i and b_i may be given in terms of the initial curvature as below:

$$a_i = \frac{l}{\kappa_0} \sin \kappa_0 \tag{4.47}$$

$$b_i = \frac{l}{\kappa_0} (1 - \cos \kappa_0) \tag{4.48}$$

To account for the curvature, the length of rigid-body link is ρl where ρ is given by,

$$\rho = \left\{ \left[\frac{a_i}{l} - (1 - \gamma) \right]^2 + \left(\frac{b_i}{l} \right)^2 \right\}^{\frac{1}{2}} \tag{4.49}$$

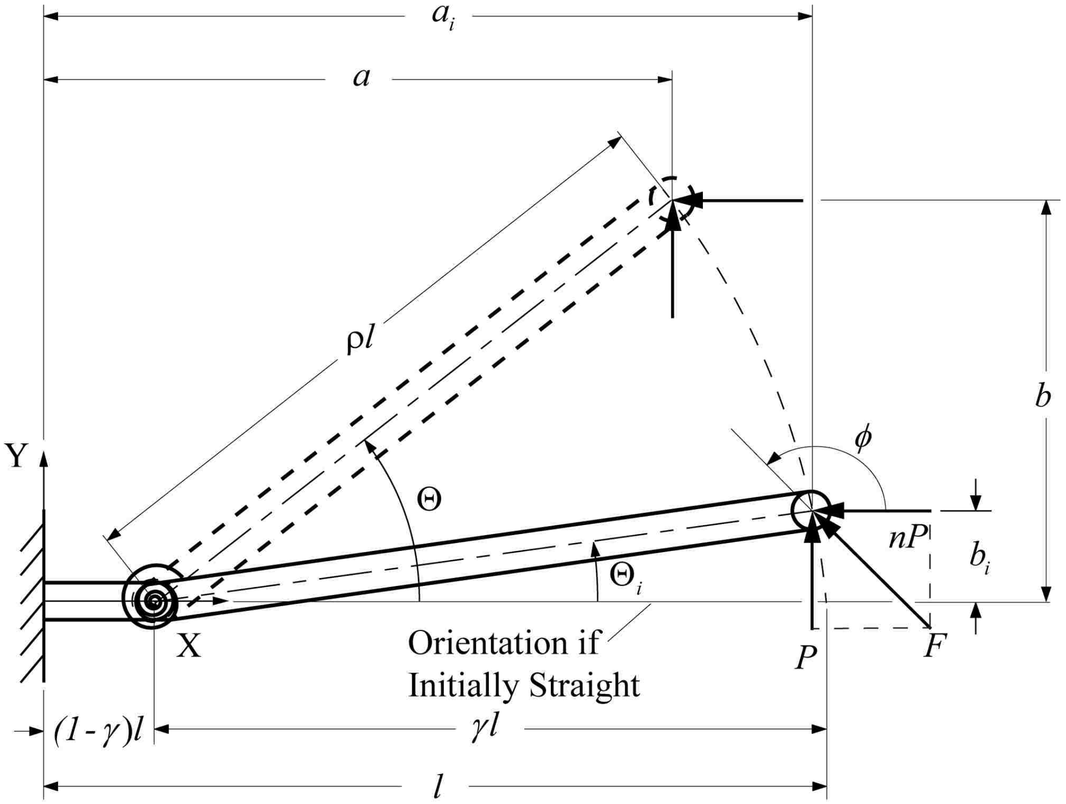

Figure 4.7. PRBM of an Initially-Curved Fixed-Free Beam with an Insert

As the beam is initially curved, the pseudo-rigid-body angle Θ will have a non-zero initial value such that,

$$\Theta_i = \tan^{-1}\frac{b_i}{a_i - l(1-\gamma)} \tag{4.50}$$

The torsional spring moment at the characteristic pivot is given by the following relationship:

$$K_t^e(\Theta - \Theta_i) = F\sin(\phi - \Theta)\,\rho l \tag{4.51}$$

where, K_t^e is the equivalent stiffness of the torsional spring given by:

$$K_t^e = K_\Theta \rho \left(\frac{E_1 I_1 + E_2 I_2}{l}\right) \tag{4.52}$$

The beam end coordinates are given by,

$$\frac{a}{l} = 1 - \gamma + \rho\cos\Theta \tag{4.53}$$

$$\frac{b}{l} = \rho\sin\Theta \tag{4.54}$$

The values of the non-dimensionalized beam tip deflection $\left(\frac{a}{l+L}, \frac{b}{l+L}\right)$ are calculated from the pseudo-rigid-body model equations (4.53) and (4.54). These are then compared favorably with the values obtained from the elliptic integral solution equations (4.39) and (4.40) and ABAQUS® as shown in Figure 4.8.

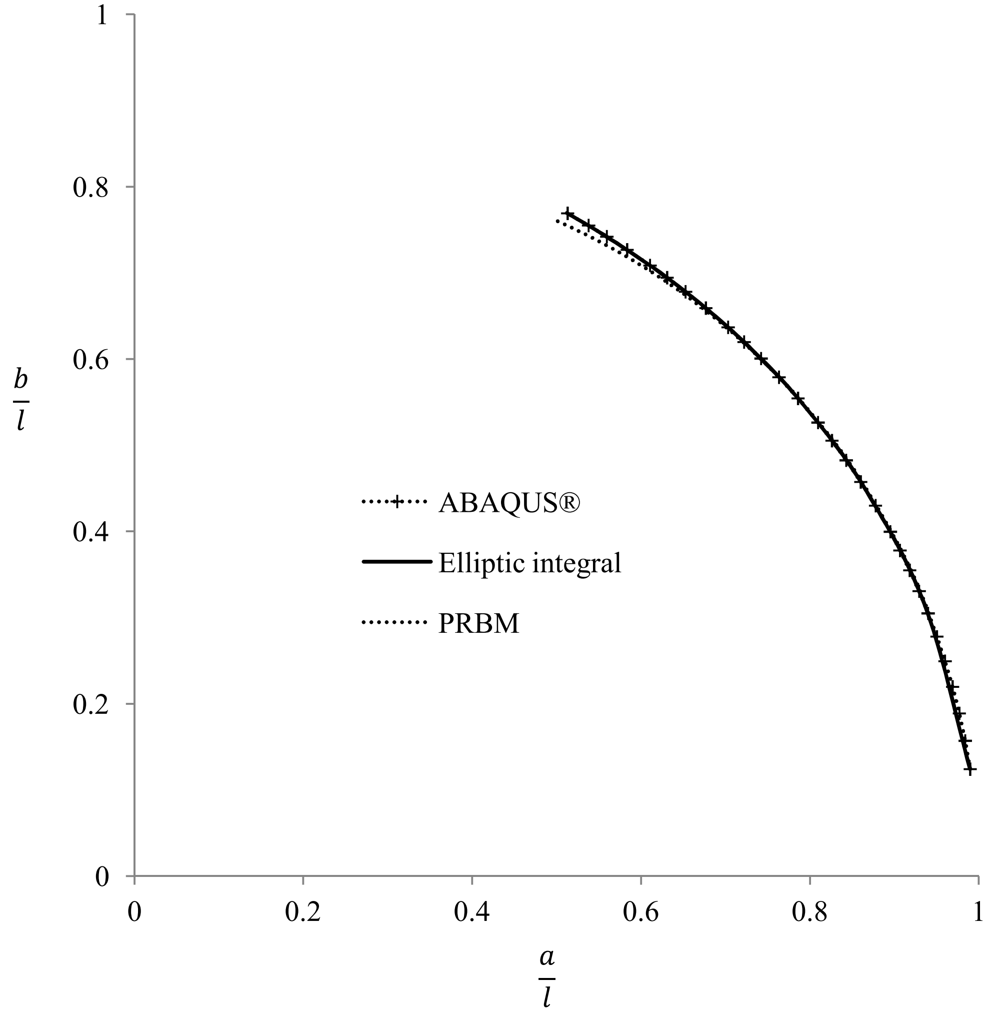

Figure 4.8. Beam End Deflection Comparison of Initially-Curved Fixed-Free Beam with an Insert for $\mathrm{n} = 0$

4.5. INITIALLY-STRAIGHT SMALL-LENGTH FLEXURAL PIVOT WITH AN INSERT

Figure 4.9 shows an initially-straight cantilever beam with a small-length flexural pivot (SLFP) subjected to non-follower combined end forces as shown. The beam has two segments; one is shorter and flexible of length *l*, and the other is longer and rigid of length L. The shorter segment has casing of flexural rigidity E_1I_1 and insert of flexural rigidity E_2I_2.

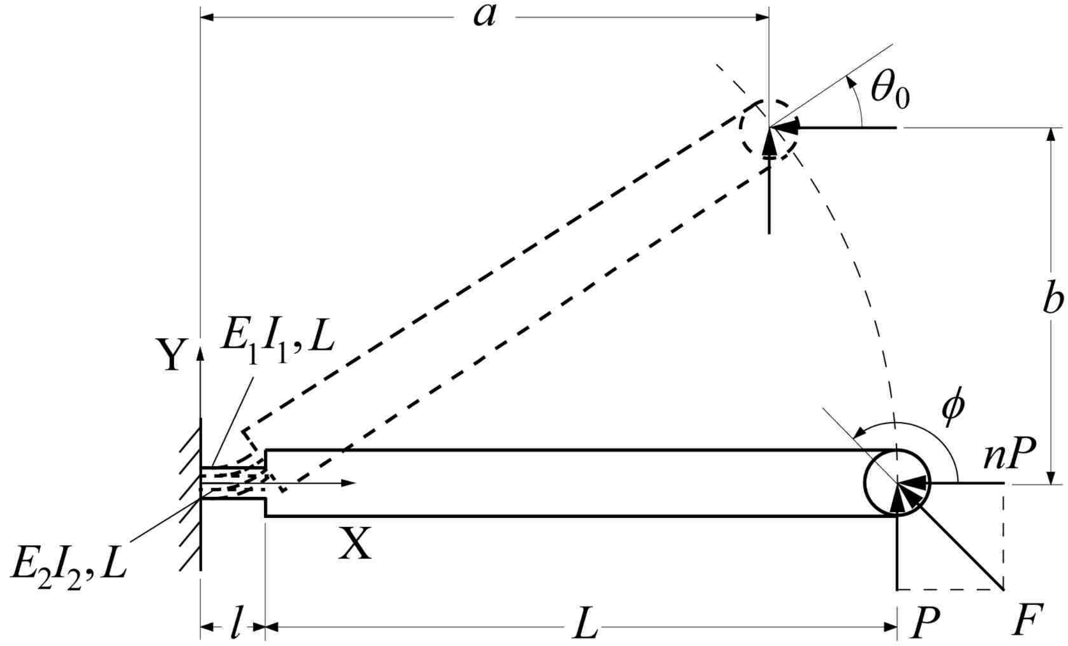

Figure 4.9. Initially-Straight Small-Length Flexural Pivot with an Insert

4.5.1. Closed-Form Elliptic Integral Solution. The beam end deflection of the entire beam, may be expressed as,

$$\alpha^e = \frac{1}{\sqrt{2}} \int_0^{\theta_0} \frac{d\theta}{\sqrt{\cos(\theta_0 - \phi) - \cos(\theta - \phi) + \lambda^e}} \tag{4.55}$$

$$\frac{\mathrm{a}}{l} = \frac{1}{\sqrt{2}\mathrm{\alpha^e}} \int_0^{\theta_0} \frac{\cos\theta \, d\theta}{\sqrt{\cos(\theta_0 - \phi) - \cos(\theta - \phi) + \lambda^e}} + L\cos\theta_0 \tag{4.56}$$

$$\frac{b}{\mathrm{l}} = \frac{1}{\sqrt{2}\mathrm{\alpha^e}} \int_0^{\theta_0} \frac{\sin\theta \, d\theta}{\sqrt{\cos(\theta_0 - \phi) - \cos(\theta - \phi) + \lambda^e}} + L\sin\theta_0 \tag{4.57}$$

where,

$$\alpha^e = \sqrt{\frac{Pl^2}{E_1 I_1 + E_2 I_2}} \tag{4.58}$$

$$\lambda^e = \frac{1}{2}\left(\frac{M_0}{E_1 I_1 + E_2 I_2}\right)^2 \left(\frac{l}{\alpha^e}\right)^2 \tag{4.59}$$

$$M_0 = FL\sin(\phi - \theta_0) \tag{4.60}$$

$$\phi = \tan^{-1}\left(-\frac{1}{n}\right) \tag{4.61}$$

4.5.2. Equivalent Pseudo-Rigid-Body Model. Figure 4.10 shows the PRBM of the initially-straight small-length flexural pivot with casing of flexural rigidity $E_1 I_1$ and insert of flexural rigidity $E_2 I_2$ subjected to combined end forces. The beam may be modeled as two rigid links joined at a characteristic pivot located at the center of the flexural pivot. The angle of the pseudo-rigid link is the pseudo-rigid-body angle Θ. For small-length flexural pivots, the pseudo-rigid-body angle is equal to the beam end angle (Howell, 2001), i.e.

$$\Theta = \theta_0 \tag{4.62}$$

The combined resistance of the casing and the insert at the compliant segment is modeled through a torsional spring at the characteristic pivot. The stiffness of the torsional spring is given by,

$$K_t^e = \frac{E_1 I_1 + E_2 I_2}{l} \tag{4.63}$$

The torsional spring moment at the characteristic pivot is given by:

$$K_t^e \Theta = \left(L + \frac{l}{2}\right) F\sin(\phi - \Theta) \tag{4.64}$$

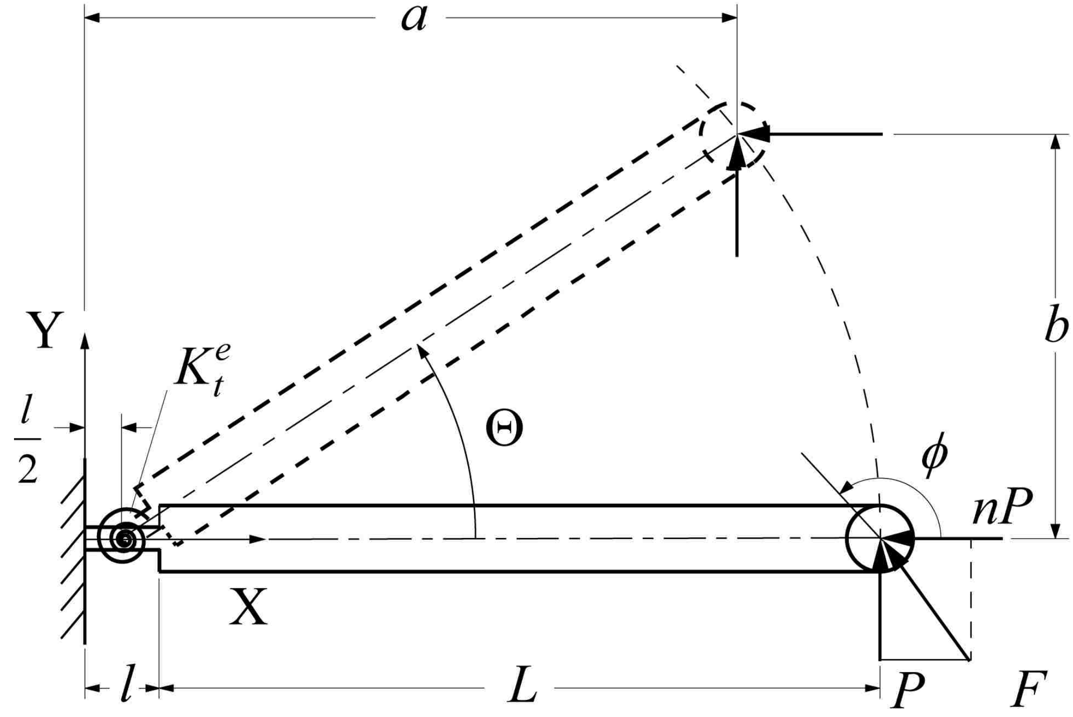

Figure 4.10. PRBM of an Initially-Straight Small-Length Flexural Pivot with an Insert

The beam end deflections are given by,

$$a = \frac{l}{2} + \left(L + \frac{l}{2}\right)\cos\Theta \tag{4.65}$$

$$b = \left(L + \frac{l}{2}\right)\sin\Theta \tag{4.66}$$

The values of the non-dimensionalized beam tip deflection $\left(\frac{a}{l+L}, \frac{b}{l+L}\right)$ are calculated from the pseudo-rigid-body model equations (4.65) and (4.66). These are then compared favorably with the values obtained from the elliptic integral solution equations (4.56) and (4.57) and ABAQUS® as shown in Figure 4.11.

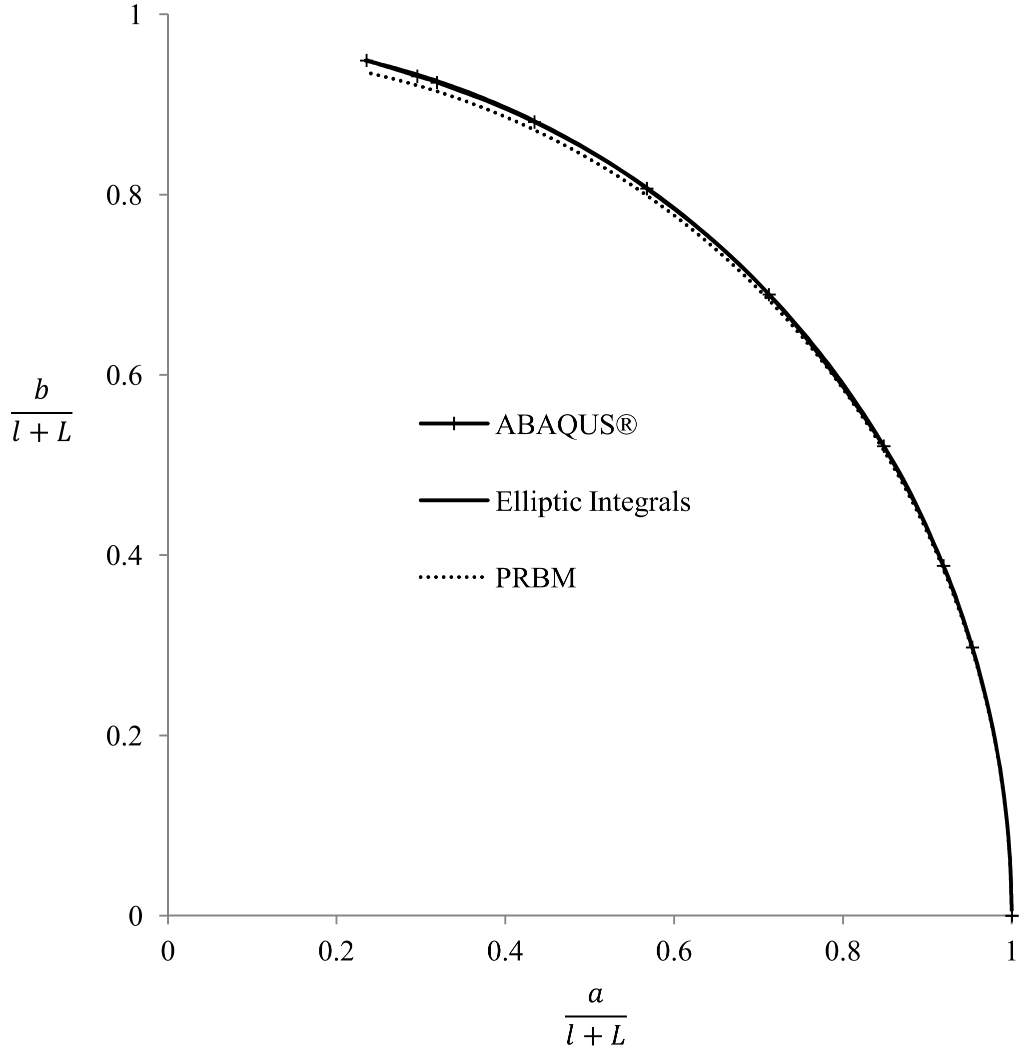

Figure 4.11. Beam End Deflection Comparison of Initially-Straight SLFP with an Insert for $\mathrm{n} = 0$

4.6. INITIALLY-CURVED SMALL-LENGTH FLEXURAL PIVOT WITH AN INSERT

Figure 4.12 shows an initially-curved small-length flexural pivot subjected to non-follower horizontal and vertical end forces *nP* and *P*, respectively. The beam has two segments, one is compliant and shorter of length *l*, and the other is rigid and longer of length *L*. The shorter segment has casing of flexural rigidity $E_1 I_1$ with an insert of flexural rigidity E_2I_2. The flexural pivot has an initial radius of curvature R_i and hence a curvature of $1/R_i$.

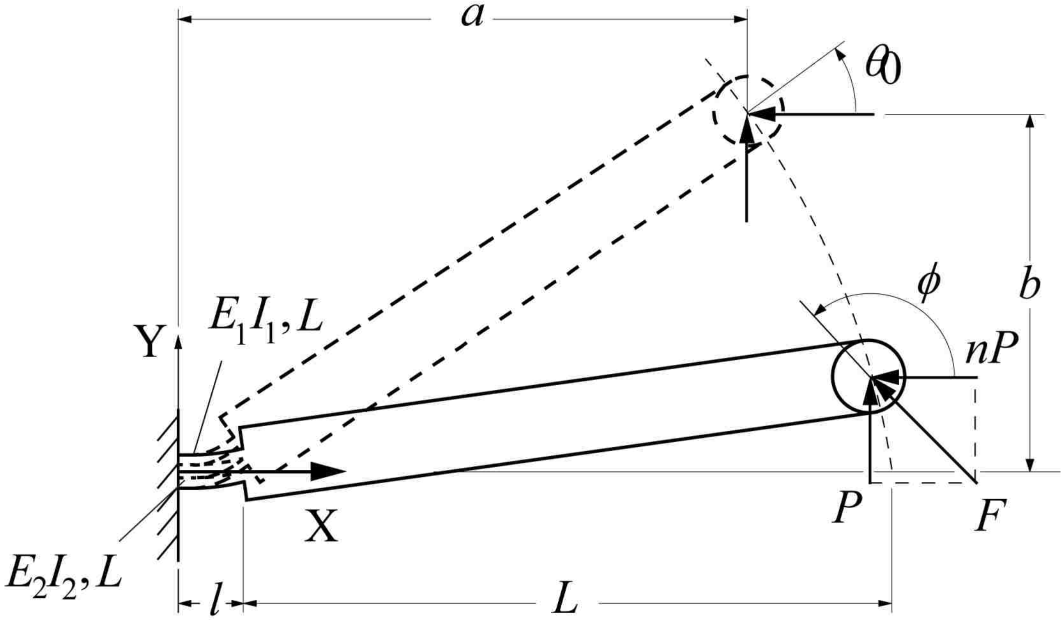

Figure 4.12. Initially-Curved Small-Length Flexural Pivot with an Insert

4.6.1. Closed-Form Elliptic Integral Solution. The coordinates of the beam end in the deformed position may be expressed as:

for $|\lambda^e| < \eta; \phi - \cos^{-1}(-\lambda^e/n) \leq -\theta_0 < \phi'$ and $\alpha^e \neq 0$,

$$\alpha^e = \frac{1}{\sqrt{\eta}}[F[\gamma_2, t] - F[\gamma_1, t]] \tag{4.67}$$

$$\frac{a}{l} = \frac{1}{\alpha^e \eta^{5/2}}\Big\{-n\eta\,\Big[[F[\gamma_2, t] - F[\gamma_1, t]] + 2[E[\gamma_1, t] - E[\gamma_2, t]]\Big] + \sqrt{2\eta(\eta + \lambda^e)}(\cos\gamma_1 - \cos\gamma_2)\Big\} + L\cos\theta_0 \tag{4.68}$$

$$\begin{aligned}\frac{b}{l} &= \frac{1}{\alpha^e \eta^{5/2}} \left\{ \eta \left[[F[\gamma_2, t] - F[\gamma_1, t]] \right. \right. \\ &\quad \left. + 2\left[E[\gamma_1, t] - E[\gamma_2, t]\right] \right] \\ &\quad \left. + n\sqrt{2\eta(\eta + \lambda^e)}(\cos\gamma_1 - \cos\gamma_2) \right\} + L\sin\theta_0\end{aligned} \tag{4.69}$$

for $\lambda^e > \eta;\ \phi - \pi \leq -\theta_0 < \phi' and\ \alpha^e \neq 0,$

$$\alpha^e = \sqrt{\frac{2}{\lambda^e + \eta}}\,[F[\psi_2, r] - F[\psi_1, r]] \tag{4.70}$$

$$\begin{aligned}\frac{a}{l} &= \frac{\sqrt{2(\eta + \lambda^e)}}{\alpha^e \eta^2} \left\{ -n \left[\frac{\lambda}{\eta + \lambda^e}[F[\psi_2, r] - F[\psi_1, r]] + \left[E[\psi_1, r] - E[\psi_2, r]\right] \right] \right. \\ &\quad \left. + \left[\sqrt{1 - \frac{\eta - n}{\eta + \lambda^e}} - \sqrt{1 - \frac{\eta + \sin\theta_0 - n\cos\theta_0}{\eta + \lambda^e}} \right] \right\} + L\cos\theta_0\end{aligned} \tag{4.71}$$

$$\begin{aligned}\frac{b}{l} &= \frac{\sqrt{2(\eta + \lambda^e)}}{\alpha^e \eta^2} \left\{ \frac{\lambda}{\eta + \lambda^e}[F[\psi_2, r] - F[\psi_1, r]] + \left[E[\psi_1, r] - E[\psi_2, r]\right] \right. \\ &\quad \left. + n\left[\sqrt{1 - \frac{\eta - n}{\eta + \lambda^e}} - \sqrt{1 - \frac{\eta + \sin\theta_0 - n\cos\theta_0}{\eta + \lambda^e}} \right] \right\} + L\sin\theta_0\end{aligned} \tag{4.72}$$

where,

$$M_0 = FL\sin(\phi - \theta_0) \tag{4.73}$$

$$\phi = \tan^{-1}\left(-\frac{1}{n}\right) \tag{4.74}$$

$$\alpha^e = \sqrt{\frac{Pl^2}{E_1 I_1 + E_2 I_2}} \tag{4.75}$$

$$\lambda^e = \frac{1}{2}\left(\frac{M_0}{E_1 I_1 + E_2 I_2} + \frac{1}{R_i}\right)^2 \left(\frac{l}{\alpha^e}\right)^2 + \sin\theta_0 - n\cos\theta_0 \tag{4.76}$$

$$\eta = \sqrt{1+n^2}; \qquad \phi' = \tan^{-1}\left(\frac{1}{n}\right) \tag{4.77}$$

$$\gamma_1 = \sin^{-1}\sqrt{\frac{\eta - n}{\eta + \lambda^e}}; \qquad \gamma_2 = \sin^{-1}\sqrt{\frac{\eta + \sin\theta_0 - n\cos\theta_0}{\eta + \lambda^e}} \tag{4.78}$$

$$\psi_1 = \sin^{-1}\sqrt{\frac{\eta - n}{2\eta}}; \qquad \psi_2 = \sin^{-1}\sqrt{\frac{\eta + \sin\theta_0 - n\cos\theta_0}{\psi_1}} \tag{4.79}$$

$$t = \sqrt{\frac{\eta + \lambda^e}{2\eta}}; \qquad r = \sqrt{\frac{2\eta}{\eta + \lambda^e}} \tag{4.80}$$

4.6.2. Equivalent Pseudo-Rigid-Body Model. Figure 4.13 shows the PRBM of the initially-curved small-length flexural pivot with casing of flexural rigidity E_1I_1 and insert of flexural rigidity E_2I_2 subjected to combined end forces. The beam has an initial radius of curvature R_i and hence a curvature of $1/R_i$. The initial curvature can be related to the beam length using the non-dimensional parameterκ_0 as,

$$\kappa_0 = \frac{l}{R_i} \tag{4.81}$$

The beam is modeled as two rigid links joined at a characteristic pivot located at the center of the flexural pivot along the undeformed curvature. The angle of the pseudo-rigid link is the pseudo-rigid-body angle Θ. For small-length flexural pivots, the pseudo-rigid-body angle is equal to the beam end angle, i.e.

$$\Theta = \theta_0 \tag{4.82}$$

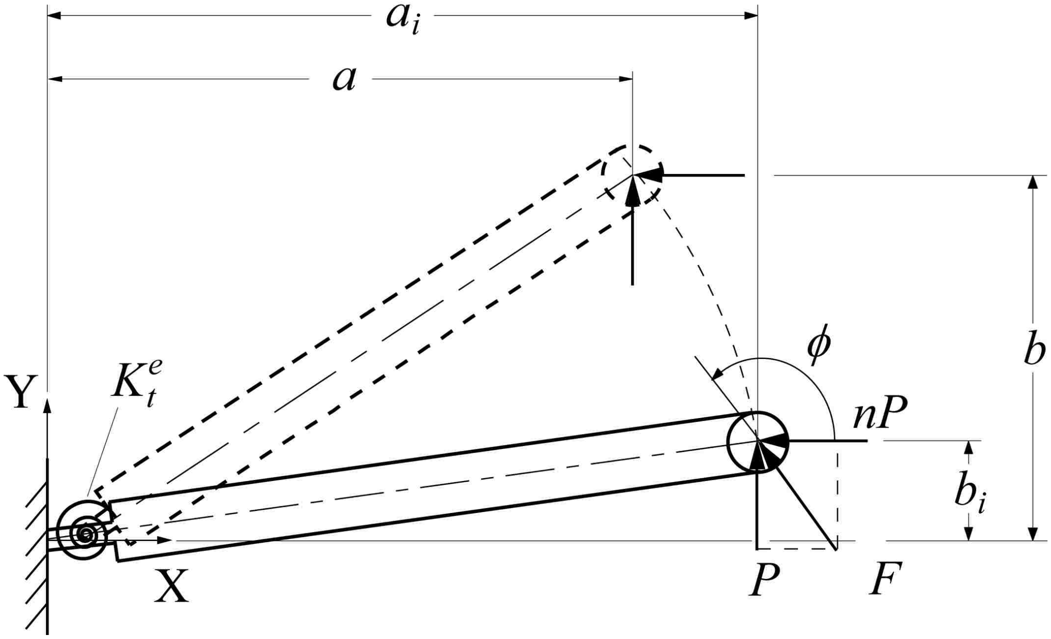

Figure 4.13. PRBM of an Initially-Curved Small-Length Flexural Pivot with an Insert

The initial beam end coordinates a_i and $b_i$are,

$$a_i = \frac{l}{\kappa_0}\sin\kappa_0 + L\cos\kappa_0 \tag{4.83}$$

$$b_i = \frac{l}{\kappa_0}(1-\cos\kappa_0) + L\sin\kappa_0 \tag{4.84}$$

As the beam is initially curved, the pseudo-rigid-body angle Θ will have a non-zero initial value such that,

$$\Theta_i = \tan^{-1}\left(\frac{b_i - \frac{l}{2\kappa_0}(1-\cos\kappa_0)}{a_i - \frac{l}{2\kappa_0}\sin\kappa_0}\right) \tag{4.85}$$

The combined resistance of the casing and insert at the compliant segment is modeled through a torsional spring at characteristic pivot whose equivalent stiffness is given by,

$$K_t^e = \frac{E_1 I_1 + E_2 I_2}{l} \tag{4.86}$$

The torsional spring moment at the characteristic pivot is given by,

$$K_t^e(\Theta - \Theta_i) = \left(L + \frac{l}{2}\right) F \sin(\phi - \Theta) \tag{4.87}$$

The beam end deflections are given by,

$$a = \frac{l}{2\kappa_0} \sin \kappa_0 + \left(L + \frac{l}{2}\right) \cos \Theta \tag{4.88}$$

$$b = \frac{l}{2\kappa_0}(1 - \cos \kappa_0) + \left(L + \frac{l}{2}\right) \sin \Theta \tag{4.89}$$

Figure 4.14 shows the beam end coordinate comparison calculated using ABAQUS®, elliptic integrals and PRBM.

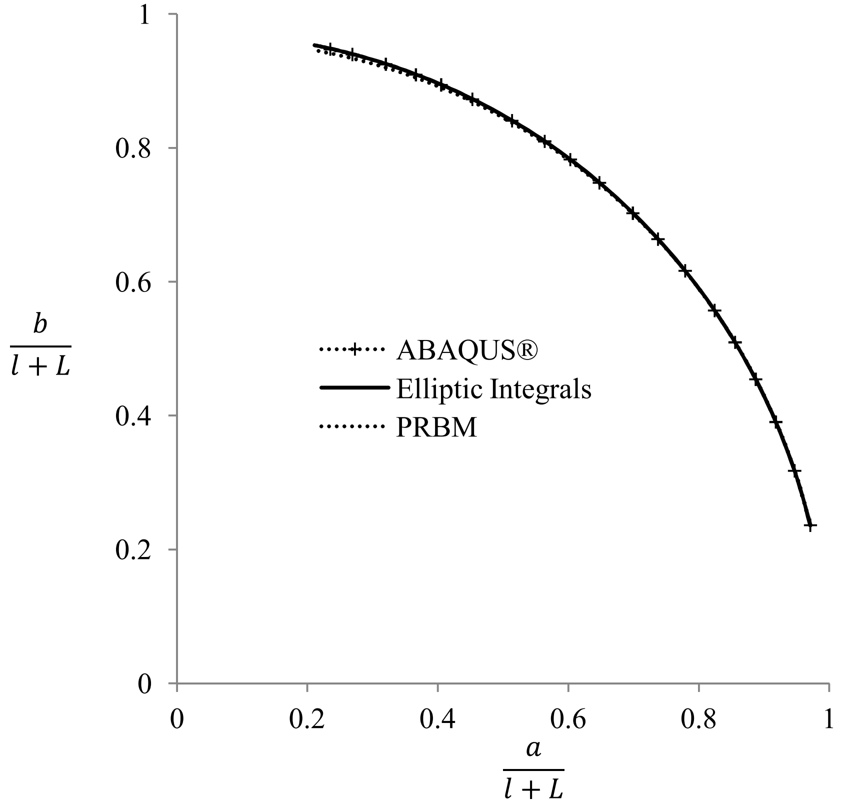

Figure 4.14. Beam End Deflection Comparison of Initially-Curved SLFP with an Insert for n = 0

4.7. INITIALLY CURVED PINNED-PINNED SEGMENT WITH AN INSERT

Figure 4.15 shows an initially-curved pinned-pinned flexible segment of length l with casing of flexural rigidity E_1I_1 and insert of flexural rigidity E_2I_2 subjected to non-follower horizontal force P. The beam has an initial curvature κ_0 where,

$$\kappa_0 = \frac{1}{R_i} \tag{4.90}$$

Following sections discuss the elliptic and PRBM solutions for an initially-curved pinned-pinned flexible beam with an insert.

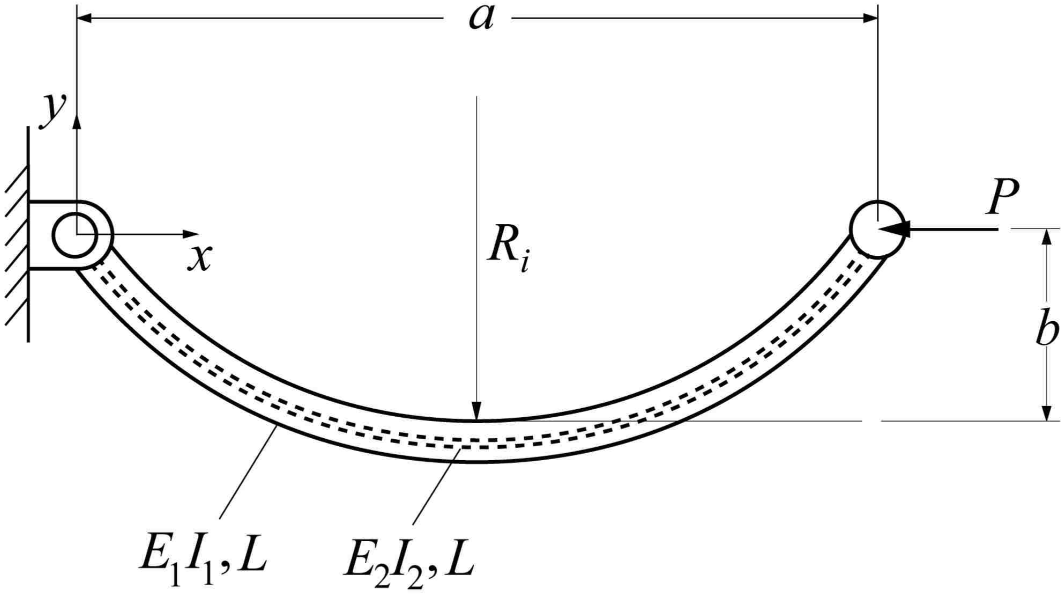

Figure 4.15. Initially-Curved Pinned-Pinned Segment with an Insert

4.7.1. Closed-Form Elliptic Integral Solution. The closed-form elliptic integral solution for a pinned-pinned segment with an insert subject to a non-follower horizontal force may be given as follows:

For $\lambda > 1$

$$\frac{a}{l} = \frac{1}{\alpha^e t}\left[(t^2 - 2)F(\beta, t) + 2E(\beta, t)\right] \tag{4.91}$$

$$\frac{b}{l} = \frac{\sqrt{2}}{\alpha^e}\left(\sqrt{\lambda + 1} - \sqrt{\lambda + \cos\theta_0}\right) \tag{4.92}$$

$$\alpha^e = tF(\beta, t) \tag{4.93}$$

$$\alpha^e = \sqrt{\frac{Pl^2}{E_1 I_1 + E_2 I_2}} \tag{4.94}$$

$$\lambda = \frac{k_0^2}{2\alpha^{e^2}} - \cos\theta_0 \tag{4.95}$$

$$\beta = \frac{\theta_0}{2} \tag{4.96}$$

$$t = \sqrt{\frac{2}{\lambda + 1}} \tag{4.97}$$

For $|\lambda| < 1$

$$\frac{a}{l} = \frac{1}{\alpha^e}\left[2E(\psi, r) - F(\psi, r)\right] \tag{4.98}$$

$$\frac{b}{l} = \frac{\sqrt{2}}{\alpha^e}\left(\sqrt{\lambda + 1} - \sqrt{\lambda + \cos\theta_0}\right) \tag{4.99}$$

$$\alpha^e = F(\psi, r) \tag{4.100}$$

$$\psi = \sin^{-1}\sqrt{\frac{1 - \cos\theta_0}{\lambda + 1}} \tag{4.101}$$

$$r = \sqrt{\frac{\lambda + 1}{2}} \tag{4.102}$$

4.7.2. Equivalent Pseudo-Rigid-Body Model. The equivalent pseudo-rigid-body model of an initially-curved pinned-pinned flexible segment of length l with casing of flexural rigidity E_1I_1 and insert of flexural rigidity E_2I_2 subjected to non-follower horizontal force P may be represented as shown in Figure 4.17. The symmetry of the beam is used to divide the complete segment into two equivalent half-segments which are conceptually equal to initially-curved fixed-free segments as shown in Figure 4.16 in its PRBM form. Thus, the entire pinned-pinned segment shown in Figure 4.15 may be represented in terms of an identical PRBM on each side of the segment midpoint. The equivalent resistance of the casing and the insert to the deflection is modeled through nonlinear torsional springs which are identical due to symmetry.

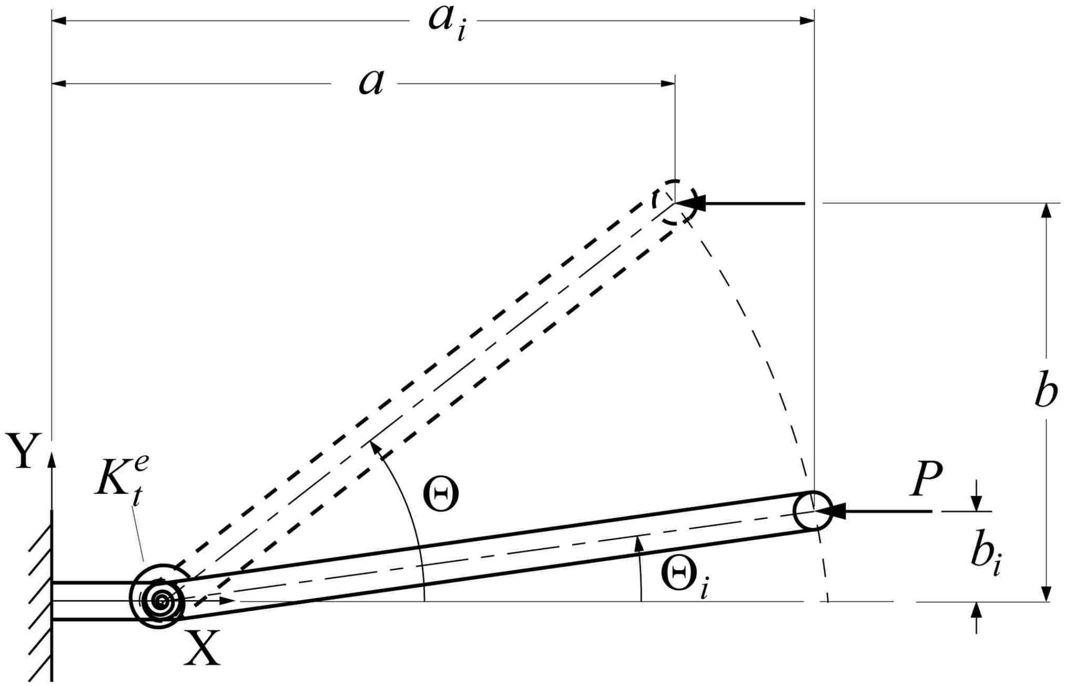

Figure 4.16. PRBM in Deflected Position

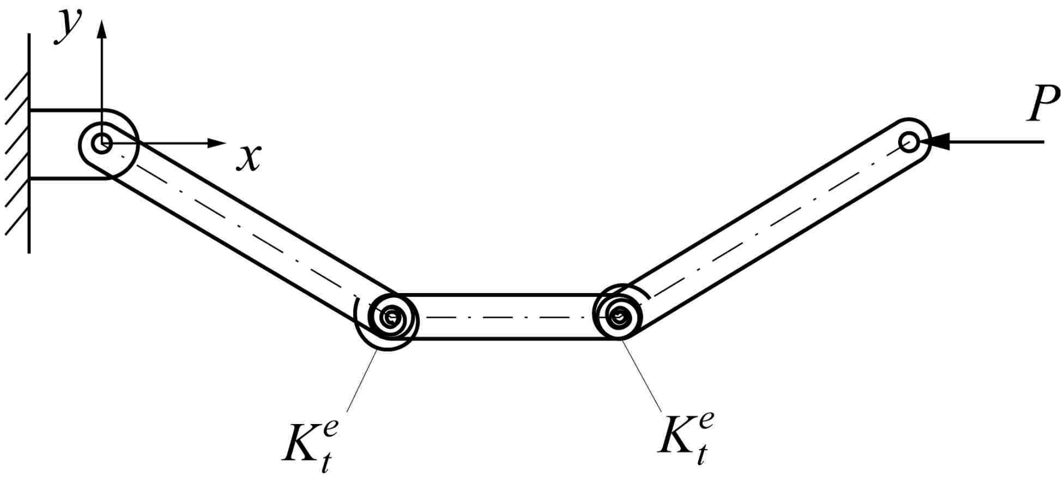

Figure 4.17. PRBM of Entire Pinned-Pinned Segment with an Insert

The initial non-dimensional horizontal and vertical coordinates of the beam are,

$$a_i = \frac{l}{\kappa_0} \sin \kappa_0 \tag{4.103}$$

$$b_i = \frac{l}{\kappa_0} (1 - \cos \kappa_0) \tag{4.104}$$

And the initial value of the pseudo-rigid-body angle $\Theta_i$is,

$$\Theta_i = \tan^{-1} \frac{b_i}{a_i - l(1-\gamma)} \tag{4.105}$$

To account for the curvature, the length of rigid-body link is ρl where ρ is given by,

$$\rho = \left\{ \left[\frac{a_i}{l} - (1-\gamma) \right]^2 + \left(\frac{b_i}{l} \right)^2 \right\}^{\frac{1}{2}} \tag{4.106}$$

And the value of the equivalent stiffness of spring constant is given by,

$$K_t^e = \rho K_\Theta \frac{E_1 I_1 + E_2 I_2}{l} \tag{4.107}$$

The torsional spring moment at the characteristic pivot is given by,

$$K_t^e(\Theta - \Theta_i) = F\sin(\Theta)\,\gamma l \tag{4.108}$$

The beam end coordinates are given by,

$$\frac{a}{l} = 2(1 - \gamma + \rho\cos\theta) \tag{4.109}$$

$$\frac{b}{l} = \rho\sin\theta \tag{4.110}$$

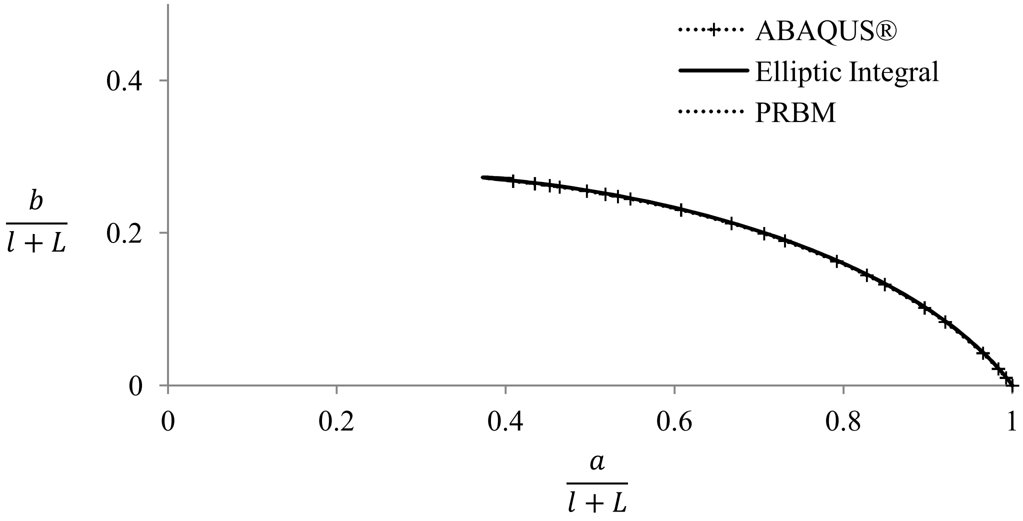

Figure 4.18. Beam End Deflection Comparison of Initially-Curved Pinned-Pinned Segment with an Insert

4.8. FIXED-GUIDED COMPLIANT BEAM WITH AN INSERT AND AN INFLECTION POINT

A fixed-guided compliant beam of length L with casing of flexural rigidity E_1I_1 and insert of flexural rigidity E_2I_2 subjected with end forces and moment is shown in Figure 4.19, where, P is the transverse force, nP the axial force, and M the moment. Table 4.1 summarizes the conditions on these loads that will yield an inflection point (Pi).

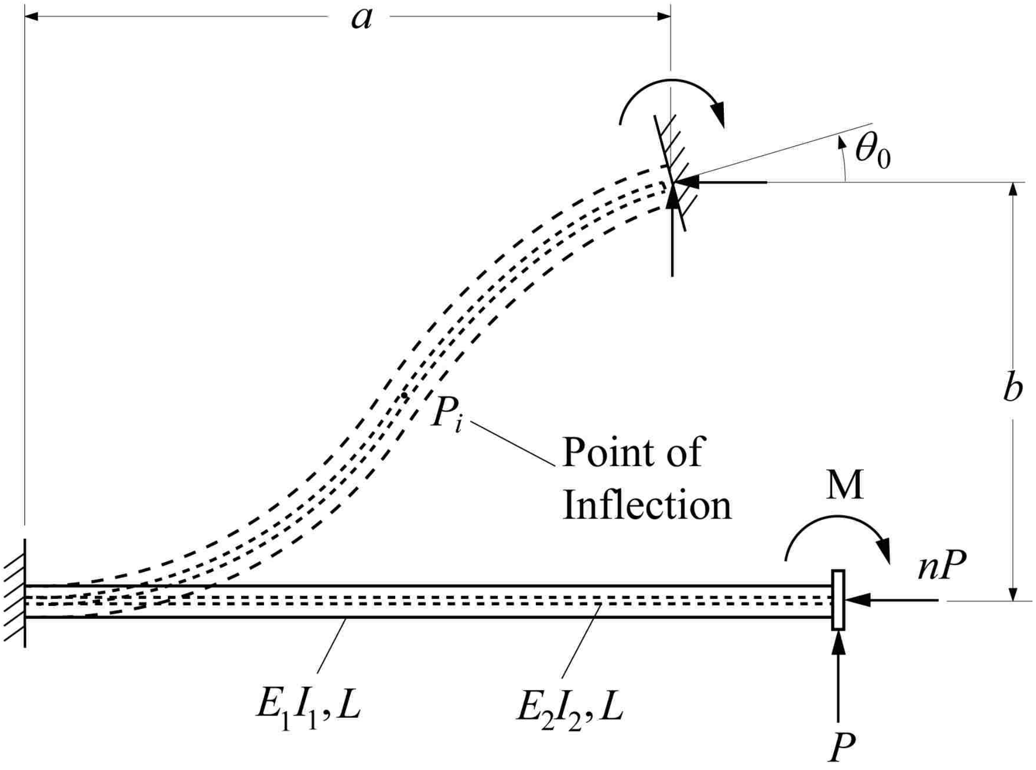

Figure 4.19. Fixed-Guided Compliant Beam with an Insert and End Forces and Opposing Moment

Table 4.1. Dependence of P_i on P and M

P	M	Point of Inflection (Pi)
+	+	Not Possible
+	−	Possible
−	+	Possible
−	−	Not Possible

4.8.1. Closed-Form Elliptic Integral Solution. The non-dimensionalized beam tip deflections from the elliptic integral solution for a fixed guided beam with an inflection point may be given as follows:

$$\frac{a}{l}=\frac{1}{\alpha^{e}\eta^{5/2}}\left[-n\eta f^{*}+2n\eta e^{*}+\sqrt{2\eta}c_{x}^{*}\right] \tag{4.111}$$

$$\frac{b}{l}=\frac{1}{\alpha^{e}\eta^{5/2}}\left[\eta f^{*}-2\eta e^{*}+\sqrt{2\eta}c_{y}^{*}\right] \tag{4.112}$$

where,

$$\eta=\sqrt{1+n^{2}} \tag{4.113}$$

$$\alpha^{e}=\sqrt{\frac{Pl^{2}}{E_{1}I_{1}+E_{2}I_{2}}} \tag{4.114}$$

$$\alpha^{e}=\sqrt{\frac{1}{\eta}f^{*}} \tag{4.115}$$

$$f^{*}=F(\gamma_{1},k)+F(\gamma_{2},k) \tag{4.116}$$

$$e^{*}=E(\gamma_{1},k)+E(\gamma_{2},k) \tag{4.117}$$

$$c_{x}^{*}=c_{x1}+c_{x2} \tag{4.118}$$

$$c_{y}^{*}=c_{y1}+c_{y2} \tag{4.119}$$

$$c_{x1}=-\sqrt{\lambda+\eta}\left(n\sqrt{\frac{\eta-n}{\eta+n}}-1\right) \tag{4.120}$$

$$c_{x2}=-\sqrt{\kappa}\left(n\sqrt{\frac{\eta+\sin\theta_{0}-n\cos\theta_{0}}{\eta-\sin\theta_{0}+n\cos\theta_{0}}}-1\right) \tag{4.121}$$

$$c_{y1}=\sqrt{\lambda+\eta}\left(n+\sqrt{\frac{\eta-n}{\eta+n}}\right) \tag{4.122}$$

$$c_{y2}=\sqrt{\kappa}\left(n+\sqrt{\frac{\eta+\sin\theta_{0}-n\cos\theta_{0}}{\eta-\sin\theta_{0}+n\cos\theta_{0}}}\right) \tag{4.123}$$

$$\gamma_1 = \sin^{-1}\sqrt{\frac{2\eta}{\lambda+\eta}\left(\frac{\lambda+n}{\eta+n}\right)} \tag{4.124}$$

$$\gamma_2 = \sin^{-1}\sqrt{\frac{2\eta}{\lambda+\eta}\left(\frac{\kappa}{\eta-\sin\theta_0+n\cos\theta_0}\right)} \tag{4.125}$$

$$\kappa = \sqrt{\frac{\lambda+n}{2\eta}} \tag{4.126}$$

4.8.2. Equivalent Pseudo-Rigid-Body Model. Figure 4. (a) shows a fixed-guided compliant beam of length L with casing of flexural rigidity E_1I_1 and an insert of flexural rigidity E_2I_2 in its deformed state with a positive beam end angle. The beam is subjected to a transverse force *P*, an axial force *nP,* and moment *M.* According to table 4.1, this type of loading will cause an inflection point in the beam.

In its PRBM form, the beam is modeled as two fixed-free compliant segments, pinned at the inflection point, P_i, which is characterized by zero curvature and, therefore, a zero moment (Midha 2012). Both the compliant segments and their respective pseudo-rigid-body models are shown in Figure 4.(b), 4.20 (c), 4.20 (d) and 4.20 (e) respectively.

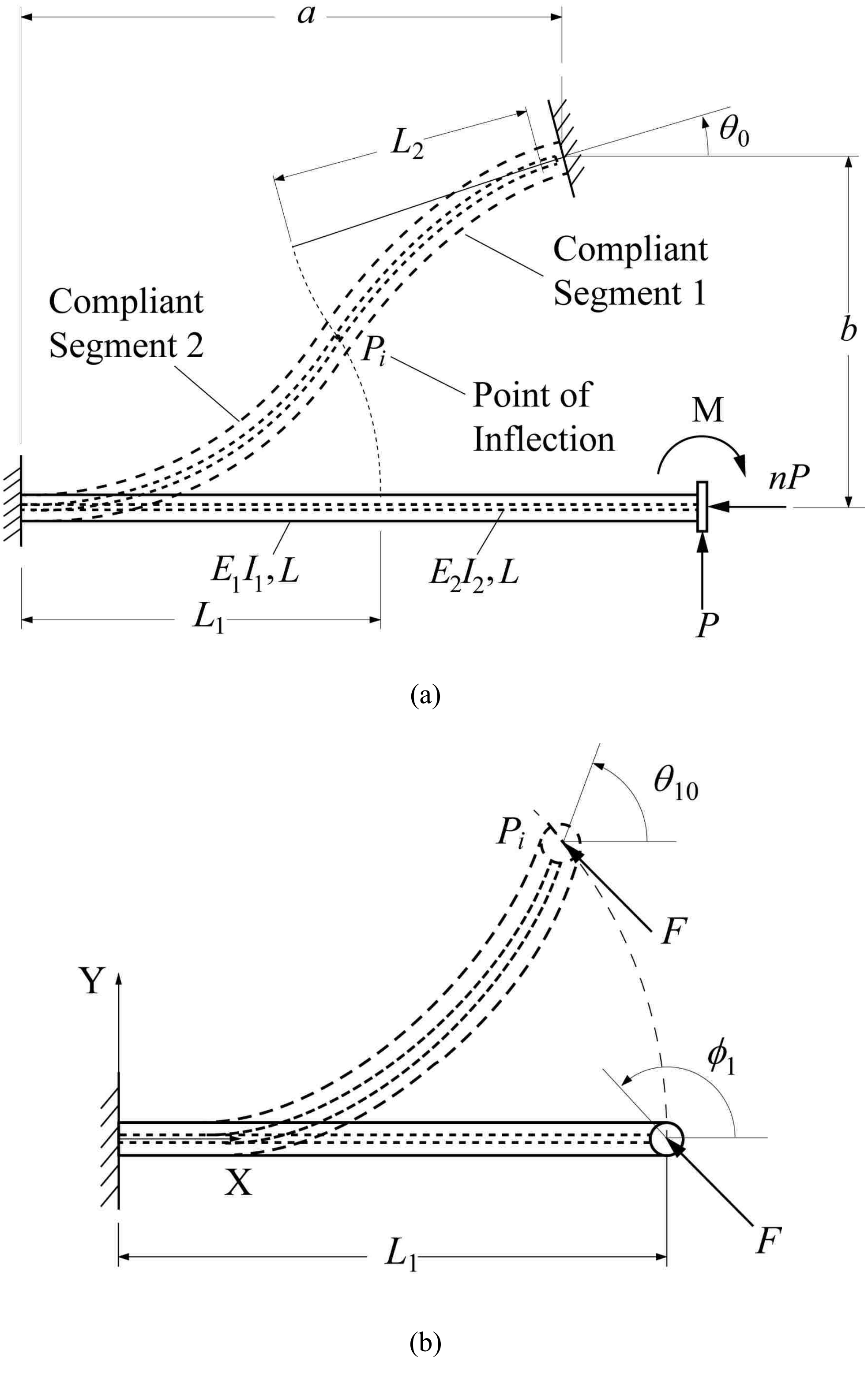

Figure 4.20. Deformed State of Fixed-Guided Compliant Beam with an Insert (a) Considered as Two Compliant Segments; (b) Compliant Segment 1; (c) Compliant Segment 2; (d) PRBM of Segment 1; and (e) PRBM of Segment 2

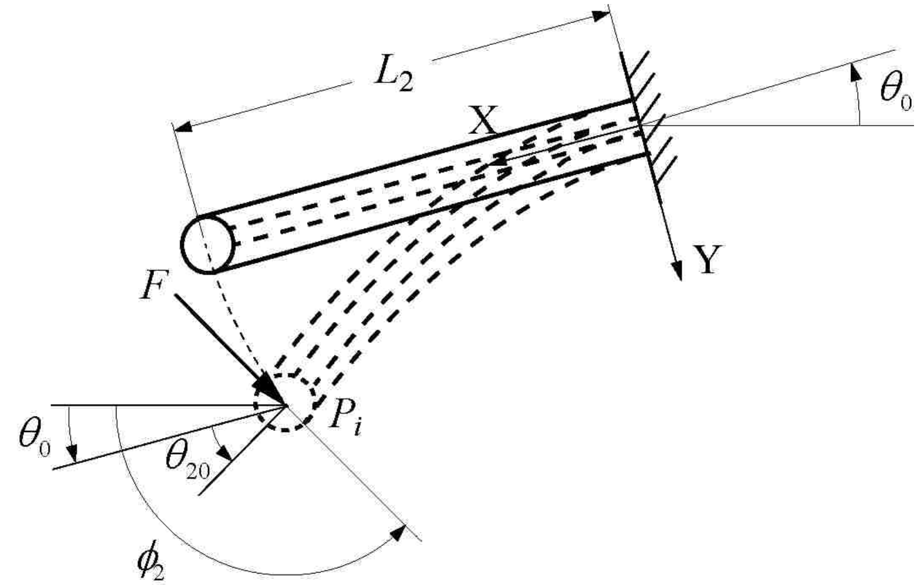

(c)

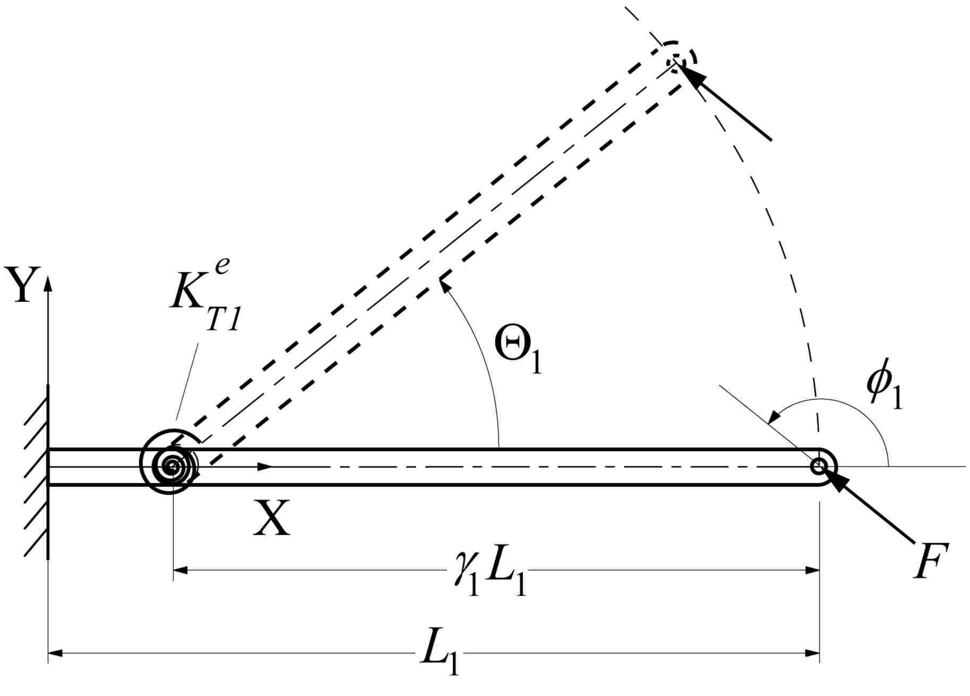

(d)

Figure 4.20. Deformed State of Fixed-Guided Compliant Beam with an Insert (a) Considered as Two Compliant Segments; (b) Compliant Segment 1; (c) Compliant Segment 2; (d) PRBM of Segment 1; and (e) PRBM of Segment 2 (cont.)

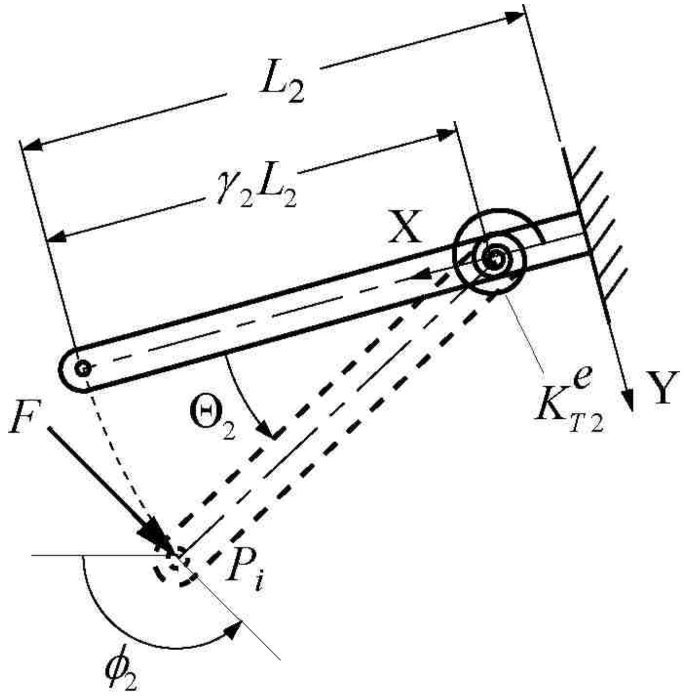

(e)

Figure 4.20. Deformed State of Fixed-Guided Compliant Beam with an Insert (a) Considered as Two Compliant Segments; (b) Compliant Segment 1; (c) Compliant Segment 2; (d) PRBM of Segment 1; and (e) PRBM of Segment 2 (cont.)

The equations are summarized below comprising of three distinct sets of equations in the analysis of the fixed-guided compliant beam with an insert, subjected to a variety of beam end load and/or displacement boundary conditions.

Based on the parametric expressions, equations (4.127) through (4.132) and are referred to as *Parametric Equations* (Midha, 2012). It should be noted that the beam stiffness coefficient K_Θ is calculated using the following improved equations discussed in Section 3.2 and 3.3:

$$\begin{gathered}\gamma_1 = 0.855651 - 0.016438n_1, \mathit{for} \ -4 \ < n_1 \ \leq \ -1.5 \\ \gamma_1 = 0.852138 - 0.018615n_1, \mathit{for} \ -1.5 \ < n_1 \ \leq \ -0.5 \\ \gamma_1 = 0.851892 - 0.020805n_1 \ + 0.005867n_1^2 - 0.000895n_1^3 + \\ 0.000069n_1^4 - 0.000002n_1^5, \mathit{for} \ -0.5 \ < n_1 \ \leq \ 10\end{gathered} \tag{4.127}$$

$$\begin{gathered}\gamma_2 = 0.855651 - 0.016438n_2, \mathit{for} \ -4 \ < n_2 \ \leq \ -1.5 \\ \gamma_2 = 0.852138 - 0.018615n_2, \mathit{for} \ -1.5 \ < n_2 \ \leq \ -0.5 \\ \gamma_2 = 0.851892 - 0.020805n_2 \ + 0.005867n_2^2 - 0.000895n_2^3 + \\ 0.000069n_2^4 - 0.000002n_2^5, \mathit{for} \ -0.5 \ < n_2 \ \leq \ 10\end{gathered} \tag{4.128}$$

$$\begin{gathered}c_{\theta_1} = 1.238945 + 0.012035n_1 + 0.00454n_1^2, \mathit{for} \ -4 < n_1 \leq \ -0.5 \\ c_{\theta_1} = 1.238845 + 0.009113n_1 - 0.001929n_1^2 + 0.000191n_1^3 + \\ 0.000390n_1^4 - 0.000013n_1^5, \mathit{for} \ -0.5 \ < n_1 \leq \ 10\end{gathered} \tag{4.129}$$

$$\begin{gathered}c_{\theta_2} = 1.238945 + 0.012035n_2 + 0.00454n_2^2, \mathit{for} \ -4 < n_2 \leq \ -0.5 \\ c_{\theta_2} = 1.238845 + 0.009113n_2 - 0.001929n_2^2 + 0.000191n_2^3 + \\ 0.000390n_2^4 - 0.000013n_2^5, \mathit{for} \ -0.5 \ < n_2 \leq \ 10\end{gathered} \tag{4.130}$$

$$\begin{aligned}K_{\Theta_1} = \frac{1}{\Theta_1}(&0.004233 - 0.012972n_1 + 2.567095\Theta_1 + 0.003993\mathrm{n}_1^2 \\ &- 0.037173\Theta_1^2 - 0.000297\mathrm{n}_1^3 + 0.179970\Theta_1^3 - 0.034678n_1\Theta_1 \\ &+ 0.003467\mathrm{n}_1^2\Theta_1 - 0.009474n_1\Theta_1^2) \ \mathit{for} \ 0 \leq n_1 \leq 10, 0 < \Theta_1 \\ &\leq 65^0\end{aligned} \tag{4.131}$$

$$K_{\Theta_1} = \frac{1}{\Theta_1}(0.000651 - 0.008244n_1 + 2.544577\Theta_1$$

$$- 0.004764\mathrm{n}_1^2 + 0.071215\Theta_1^2 - 0.000104\mathrm{n}_1^3$$

$$+ 0.079696\Theta_1^3 + 0.069274n_1\Theta_1 + 0.061507\mathrm{n}_1^2\Theta_1$$

$$- 0.347588n_1\Theta_1^2),$$

$$for - 4 < n_1 < 0, 0 < \Theta_1 < 0.8\phi_1$$

$$K_{\Theta_2} = \frac{1}{\Theta_2}(0.004233 - 0.012972n_2 + 2.5670095\Theta_2 + 0.003993\mathrm{n}_2^2$$

$$- 0.037173\Theta_2^2 - 0.000297\mathrm{n}_2^3 + 0.179970\Theta_2^3 - 0.034678n_2\Theta_2$$

$$+ 0.003467\mathrm{n}_2^2\Theta_2 - 0.009474n_2\Theta_2^2)\ for\ 0 \le n_2 \le 10, 0 < \Theta_2$$

$$\le 65^0$$

$$K_{\Theta_2} = \frac{1}{\Theta_2}(0.000651 - 0.008244n_2 + 2.544577\Theta_2 \tag{4.132}$$

$$- 0.004764\mathrm{n}_2^2 + 0.071215\Theta_2^2 - 0.000104\mathrm{n}_2^3$$

$$+ 0.079696\Theta_2^3 + 0.069274n_2\Theta_2 + 0.061507\mathrm{n}_2^2\Theta_2$$

$$- 0.347588n_2\Theta_2^2),$$

$$for - 4 < n_2 < 0, 0 < \Theta_2 < 0.8\phi_2$$

Equations (4.133) through (4.137) are derived from force and moment equilibrium using the free-body diagrams, and are referred to as the *Static Equilibrium Equations.*

$$\frac{FL_1^2}{E_1I_1 + E_2I_2}\sin\left(\phi_1 - \frac{\theta_{10}}{c_{\theta_1}}\right) - K_{\Theta_1}\frac{\theta_{10}}{c_{\theta_1}} = 0 \tag{4.133}$$

$$\frac{FL_2^2}{E_1I_1+E_2I_2} sin\left(\phi_2 - \frac{\theta_{20}}{c_{\theta_2}}\right) - K_{\Theta_2}\frac{\theta_{20}}{c_{\theta_2}} = 0 \tag{4.134}$$

$$n_1 = \frac{-1}{tan\ (\phi_1)} \tag{4.135}$$

$$n_2 = \frac{-1}{tan\ (\phi_2)} \tag{4.136}$$

$$\begin{aligned} M + &\left\{[nPcos(\theta_0) - Psin(\theta_0)]\gamma_2 L_2 sin\left(\frac{\theta_{10}-\theta_0}{c_{\theta_2}}\right)\right\} \\ + &\left\{[Pcos(\theta_0) + nPsin(\theta_0)]\left[(1-\gamma_2)L_2 + \gamma_2 L_2 sin\left(\frac{\theta_{10}-\theta_0}{c_{\theta_2}}\right)\right]\right\} = 0 \end{aligned} \tag{4.137}$$

Equations (4.138) through (4.142) reflect constraints of length, slope, and displacements, and are referred to as the *Compatibility Equations*.

$$L_1 + L_2 = L \tag{4.138}$$

$$\theta_{10} = \theta_{20} + \theta_0 \tag{4.139}$$

$$\phi_1 = \phi_2 + \theta_0$$

$$\begin{aligned} b = \gamma_1 L_1 \sin\left(\frac{\theta_{10}}{c_{\theta_1}}\right) + \gamma_2 L_2 \sin\left(\frac{\theta_{20}}{c_{\theta_2}} + \theta_0\right) \\ +(1-\gamma_2)L_2 \sin\ (\theta_0) \end{aligned} \tag{4.141}$$

$$\begin{aligned} a = (1-\gamma_1)L_1 + \gamma_1 L_1 \cos\left(\frac{\theta_{10}}{c_{\theta_1}}\right) + \gamma_2 L_2 \cos\left(\frac{\theta_{20}}{c_{\theta_2}} + \theta_0\right) \\ + (1-\gamma_2)L_2 cos\ (\theta_0) \end{aligned} \tag{4.142}$$

Table 4.2 compares the beam end coordinates calculated from PRBM, elliptic integral solution and ABAQUS®. The fixed-guided compliant beam considered in the example has following geometric and material properties:

Casing: Length, L = 20 inches; Width, w_1 = 1 inch; Height, h_1 = 0.3 inches;

Material = Polypropylene; Modulus of Elasticity, E = 200,000 psi.

Insert: Length, L = 20 inches; Width, w_2 = 0.8 inches; Height, h_2 = 0.1 inches;

Material = Steel; Modulus of Elasticity, E = 30 x 10^6 psi.

The following sign conventions are followed for the applied loads, F_x: Positive for compressive axial force; F_y: Positive for vertically upward force; M: Positive for counter-clockwise moment.

Table 4.2. Analysis of a Fixed-Guided Compliant Segment with an Insert Subjected to Load Boundary Conditions

Beam End Loads Specified	Beam End Displacement Results from		
	PRBM	Elliptic integral Solution	ABAQUS®
nP = 1.5 P = 15 M = -15	a = 15.985 b = 11.02 θ_0 = 48.392	a = 15.941 b = 10.987 θ_0 = 48.979	a = 15.956 b = 11.12 θ_0 = 49.173
nP = -3 P = 8 M = -20	a = 17.414 b = 9.113 θ_0 = 38.052	a = 17.398 b = 9.051 θ_0 = 38.297	a = 17.414 b = 9.113 θ_0 = 38.378
nP = 0 P = 4 M = -20	a = 16.382 b = 10.545 θ_0 = 45.705	a = 16.346 b = 10.506 θ_0 = 46.206	a = 16.401 b = 10.616 θ_0 = 46.424

Note: The units are: P in lb; M in-lb; b in.; a in. and θ_0 in deg.

4.9. SUMMARY

In this Section, the pseudo-rigid-body models for compliant segments with inserts subject to various boundary conditions and cases have been presented. Such beams may offer an alternative to the existing materials by overcoming their limitations of creep and strength. The compliant beam with insert is modeled as two beams in parallel. The PRBMs have been validated with the closed-form elliptic integral solution and finite element analysis solutions.

5. EXPERIMENTAL SETUP AND RESULTS

5.1. INTRODUCTION

It has been shown in previous Section that the analytical results from the pseudo-rigid-body model for the compliant beams with inserts for various boundary conditions and cases compare closely with the elliptic integral solution and the finite element analysis Software ABAQUS®. To further validate the PRBM, three experiments for the fixed-free cantilever beam with an insert were performed. For the first experiment, the beam was subject to vertical load at the free end, whereas, for the second and third experiment the beam was subject to vertical and compressive, and vertical and tensile loads. Another experiment was performed to compare the creep behavior of plastic beams with and without insert. Following sections discuss the experimental setup, procedure and the results in detail.

5.2. EXPERIMENTAL SETUP

Figure 5.1 shows the solid model of the experimental setup for the testing of the fixed-free cantilever beam with an insert. The setup is made up of two parts, the upper part is for the testing of a cantilever beam and the lower part is to be utilized for a compliant four-bar mechanism for another research effort. The entire setup is mounted on two wooden blocks which are securely fastened to a table by means of four C-clamps. Since this thesis is concerned with the cantilever beam, only the upper part of the setup will be discussed.

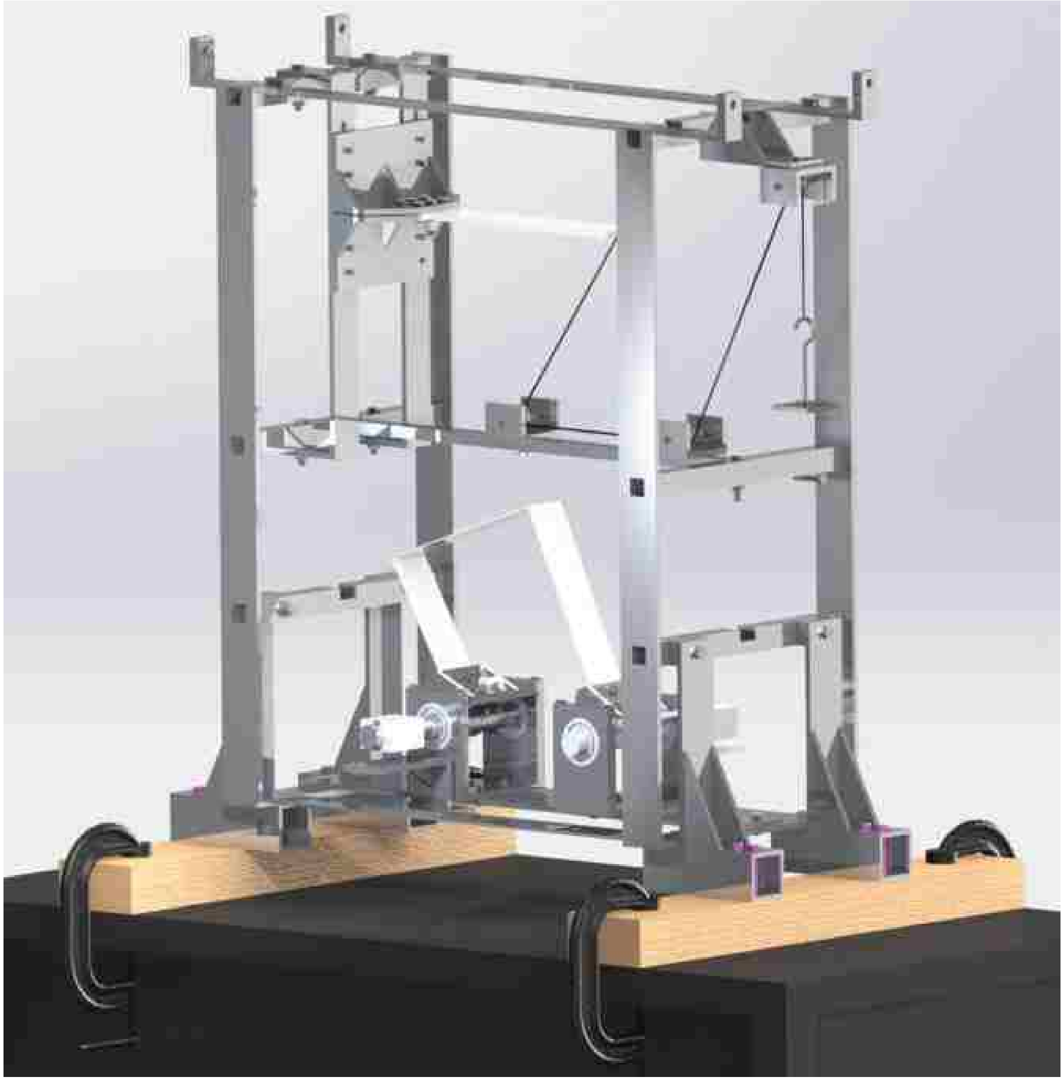

Figure 5.1. The Experimental Setup - CAD

Figure 5. (a) shows the close-up of the upper part where a cantilever beam is fixed at one end and connected to a lightweight loading rope at the other end. The beam is fixed at one end by a clamp which securely fastens the beam using six bolts passing through the holes in the beam as shown in Figure 5. (b) to ensure perfect cantileverage. The loading rope passes over three frictionless pulleys. One pulley is free to slide and lock in place in the rectangular slot as shown in Figure 5. (c) to allow for loading at an

angle. The beam is loaded by adding weights to a pan attached at the other end of the loading rope shown in Figure 5. (d).

(a)

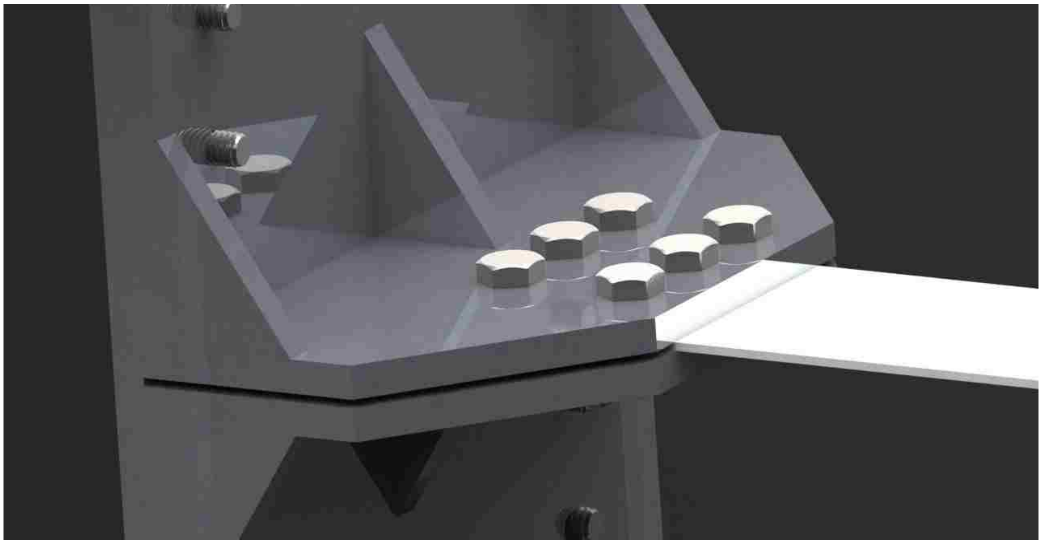

(b)

Figure 5.2. Experimental Setup (a) Test Beam; (b) The Fixture; (c) The Pulley and Rope; and (d) The Loading Arrangement

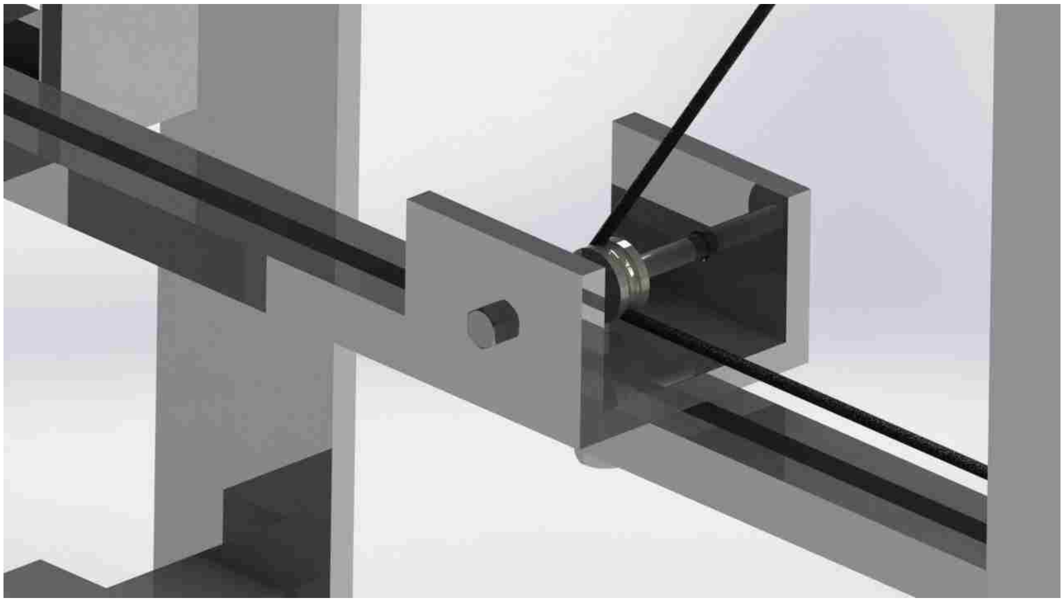

(c)

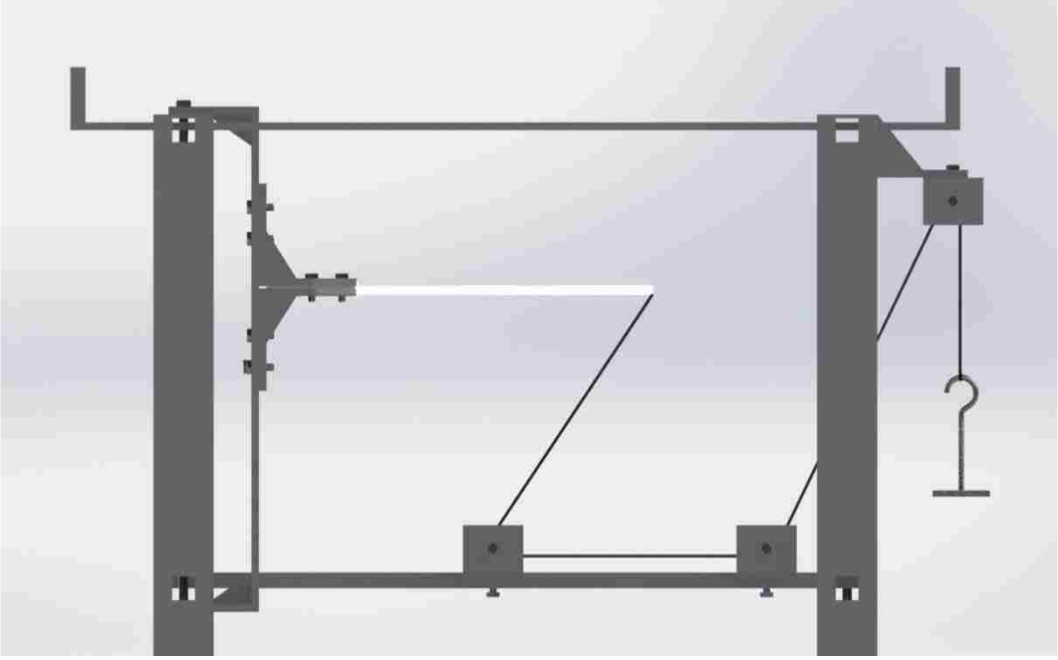

(d)

Figure 5.2. Experimental Setup (a) Test Beam; (b) The Fixture; (c) The Pulley and Rope; and (d) The Loading Arrangement (cont.)

5.3. TESTING AND RESULTS

The experimental setup discussed above was manufactured and assembled as shown in Figure 5.3.

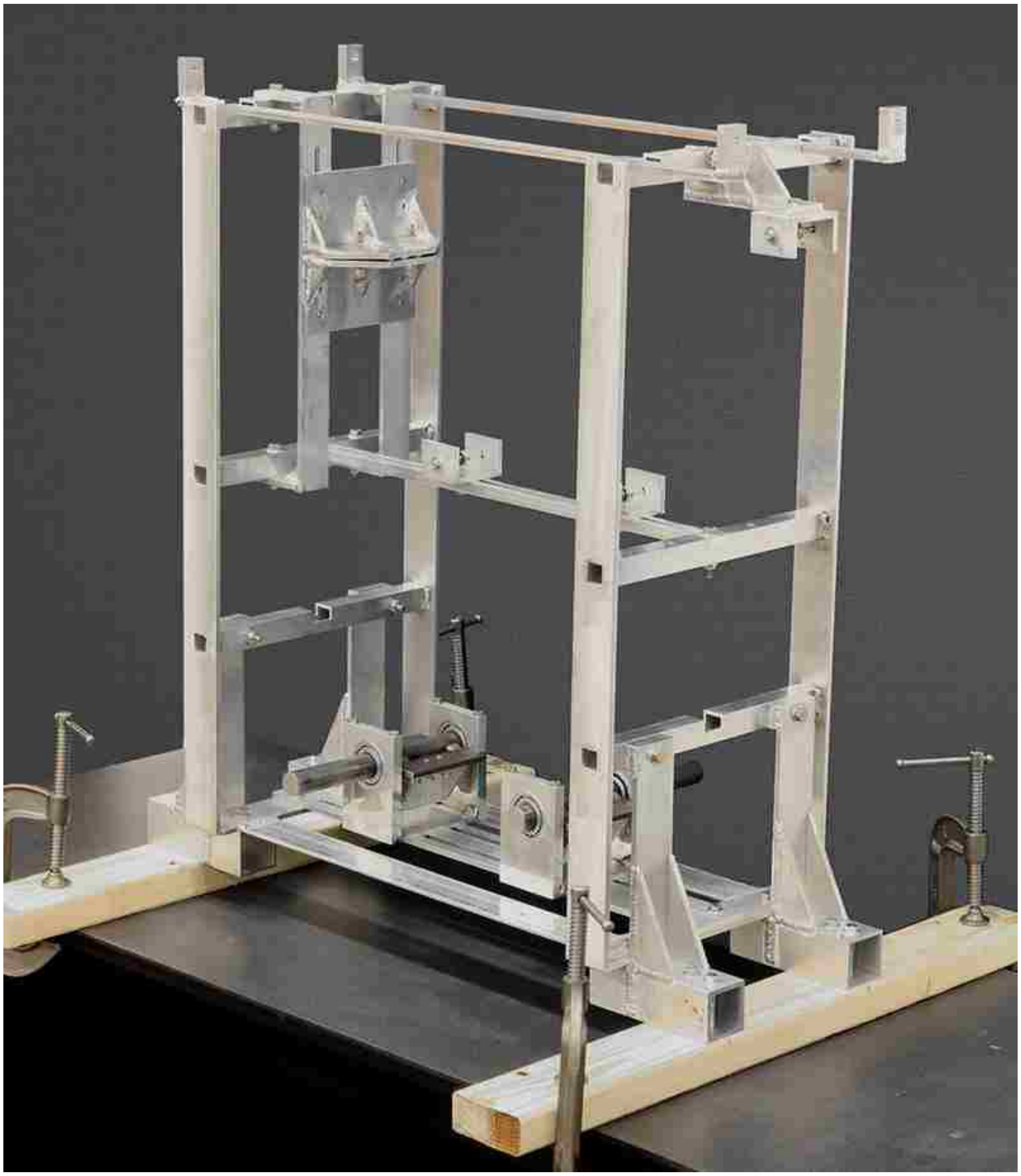

Figure 5.3. The Experimental Setup

In the example chosen for the experiment, the insert material was sandwiched between two layers of casing material, as shown in Figure 5.4. The three beams were held together by using plastic binding posts and slots were made in the lower beam to simulate no bonding and allow for lateral sliding upon deflection.

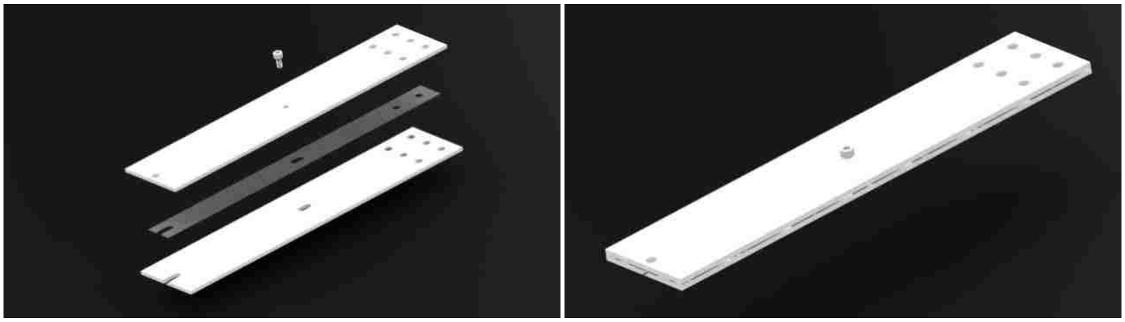

(a) (b)

Figure 5.4. The Test Beams – CAD (a) Exploded View; and (b) Assembly

The casing and the insert exhibit following material and geometric properties:

Plastic Beams (Casing) 1 and 2:

Length, L = 10 inches; Width, $w_1 = w_3$=2.5 inch; Height, $h_1 = h_3 = 0.125$ inch;

Material = Delrin®; Modulus of Elasticity, E = 550,000 psi.

Insert:

Length, L =10 inches; Width, $w_2 = 1$ inches; Height, $h_2 = 0.025$ inch;

Material = Spring Steel; Modulus of Elasticity, $E = 30 \times 10^6$ psi.

Figure 5.5 (a), (b) and (c) show the casing and insert beams used for the experiment. The assembly of the beams was then securely clamped at one end in the experimental setup using bolts as shown in Figure 5.6. A graph paper was placed at the back of the beam to record the beam end deflections of the beam.

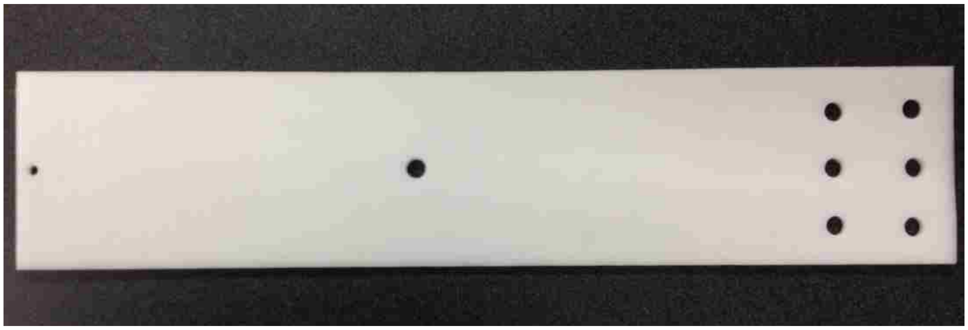

(a)

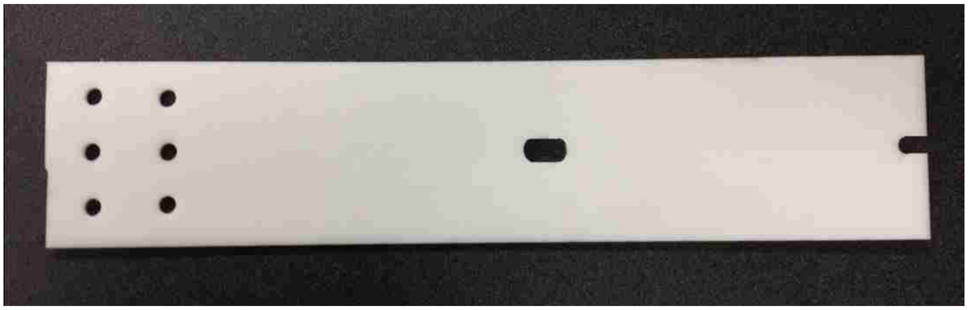

(b)

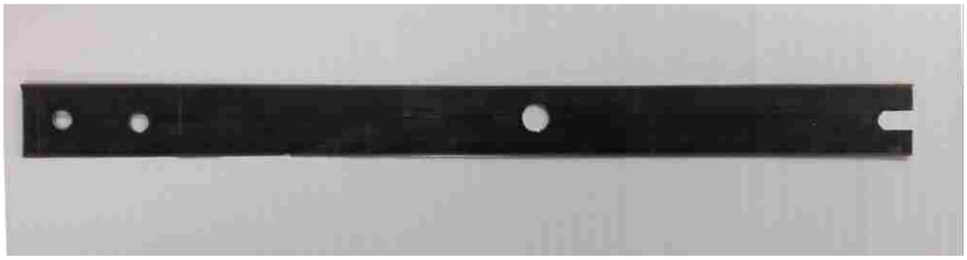

(c)

Figure 5.5. Test Beams (a) Plastic Beam 1; (b) Plastic Beam 2; and (c) Insert Beam

Figure 5.6. The Clamping

5.3.1. Experiment 1 – Vertical Loading. In the first experiment, a vertically downward force was applied at the end of the beam using a lightweight steel rope which holds the weight hanger as shown in Figure 5.7. The weight of the hanger was found to be 0.34 lbs. The weight in the hanger was increased gradually from 4 lb to 8.5 lb (excluding the weight of hanger) and the corresponding beam end points are marked on the graph paper. The measurements were then taken using a vernier caliper to capture the x and y coordinates of the beam end. The vernier caliper used for the measurement was Craftsman® mechanical caliper with a least count of 0.001 in.

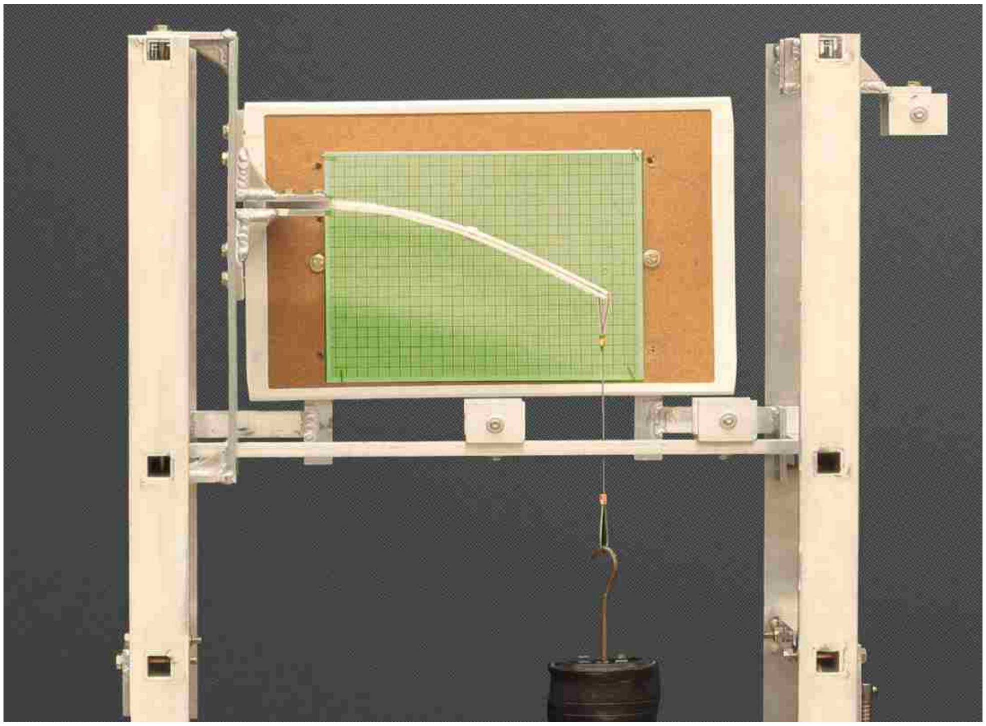

Figure 5.7. Experiment 1 – Vertical Loading

The x and y coordinates were then plotted to obtain the experimental beam end deflection for a vertically downward force. The beam end coordinates a and b calculated from experimental and PRBM results are tabulated in Table 5.1. It can be seen that the experimental results match closely with the PRBM results exhibiting a maximum relative error of 0.87%.

Figure 5.8 shows the experimental beam end points as compared with the results from pseudo-rigid-body model equations. The Maple code for this experiment is given in Appendix B.

Table 5.1 Beam End Coordinate Comparison for Vertical Loading

	Experimental		PRBM		
$F_{applied}$	b_e	a_e	b_{PRBM}	a_{PRBM}	Relative error (%)
0	0	10	0	10	-
4	2.735	9.56	2.732	9.549	0.2173
5	3.243	9.341	3.25	9.355	0.2728
6	3.677	9.148	3.717	9.146	0.6505
7	4.088	8.962	4.134	8.929	0.8685
8	4.467	8.731	4.505	8.711	0.6283
8.5	4.626	8.624	4.676	8.602	0.7826

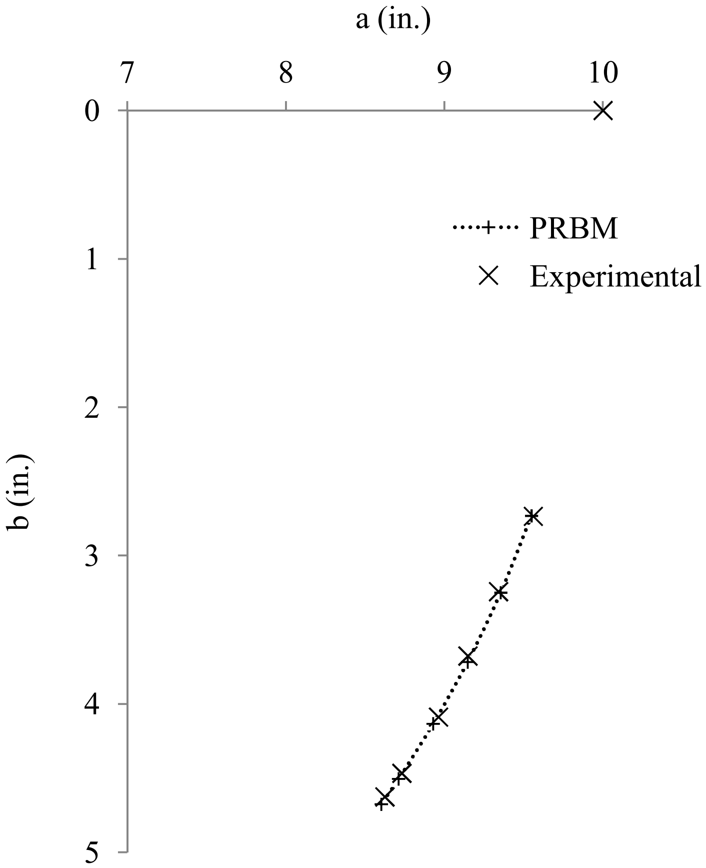

Figure 5.8. PRBM vs. Experimental Beam End Coordinate Comparison for Vertical Loading

5.3.2. Experiment 2 – Vertical and Compressive Loading: In the second experiment, the same procedure as the first experiment was repeated for vertical and compressive loads. To apply the compressive loads, the steel rope was passed over three pulleys as shown in Figure 5.9. The same load steps as used in first experiment were applied at angle of 58^0 measured from the right horizontal in the anticlockwise direction. To account for follower loading, the actual load angle after deflection was calculated and used in the theoretical analysis. The steel rope was properly lubricated at the contact point of the pulleys to reduce the friction. Even with the lubrication, some amount of friction was present due to the rubbing of steel pulley on the steel rope.

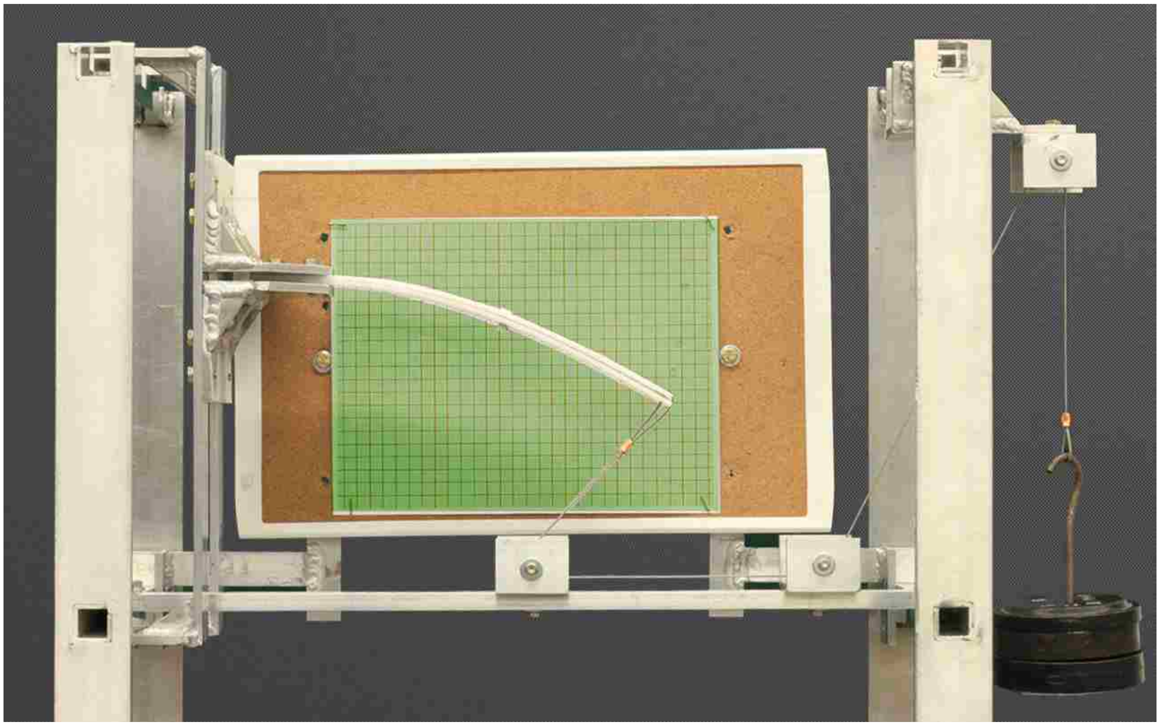

Figure 5.9. Experiment 2 – Vertical and Compressive Loading

To account for the friction, the coefficient of friction between the rope end the pulley was calculated by performing a simple experiment as shown in Figure 5.10 and using the Capstan friction equation (Meriam, 1978) mentioned below:

$$T_2 = T_1 e^{\mu\beta} \tag{5.1}$$

where, T_1 is the tension force in the low tension rope and T_2 is the tension force in the high tension rope, β is the angle of contact between the rope and the pulley.

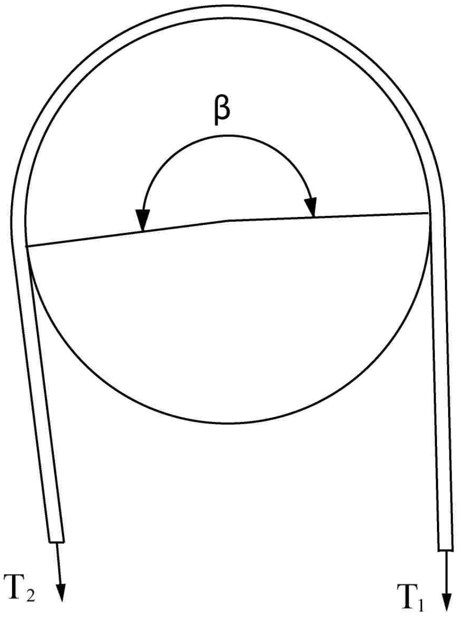

Figure 5.10. The Capstan Friction Equation Experiment

From the experiment, the coefficient of friction between the rope and pulley was determined to be 0.01. This factor was then used in the PRBM calculations to calculate the actual load acting on the beam. Figure 5.11 shows the calculation of the actual force acting on the beam considering the effect of friction between the rope and pulley. The contact angles between the rope and pulleys are denoted by β_1, β_2 and β_3; $F_{applied}$ is the load applied at the end of the rope, including the weight of the hanger and F_{actual} is the actual load acting at the beam end. The Maple code for this experiment can be found in Appendix B. The x and y coordinates of the beam end were then recorded and plotted. The beam end coordinates calculated from the PRBM and the experimental testing are listed in Table 5.2. Figure 5.12 shows the experimental beam end points comparing closely with the results from PRBM with a maximum relative error of 0.95%.

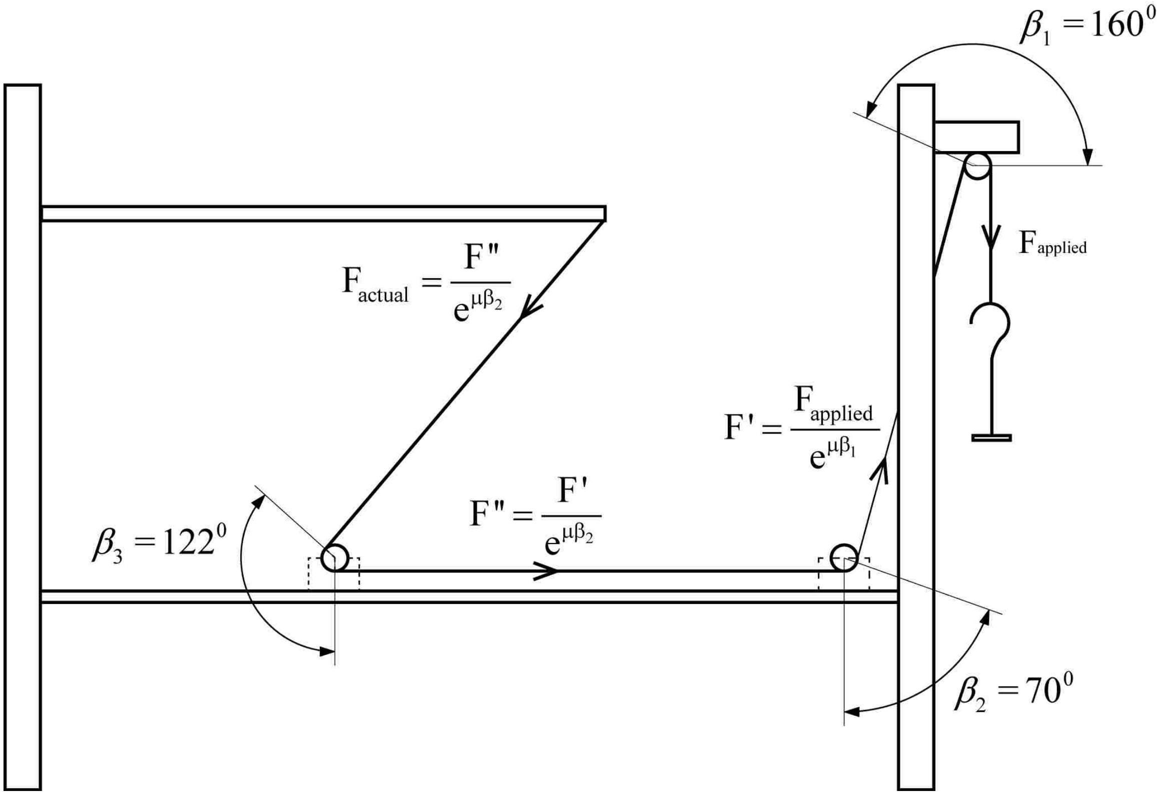

Figure 5.11 Calculation of the Actual Force Acting on the Beam for Experiment 2

Table 5.2 Beam End Coordinate Comparison for Vertical and Compressive Loading

	Experimental		PRBM		
$F_{applied}$	b_e	a_e	b_{PRBM}	a_{PRBM}	Relative error (%)
0	0	10	0	10	-
4	2.481	9.629	2.489	9.621	0.2261
5	3.09	9.422	3.089	9.408	0.2511
6	3.592	9.182	3.644	9.162	0.9141
7	4.127	8.911	4.168	8.882	0.7664
8	4.614	8.588	4.675	8.562	0.9490
8.5	4.873	8.423	4.912	8.392	0.6928

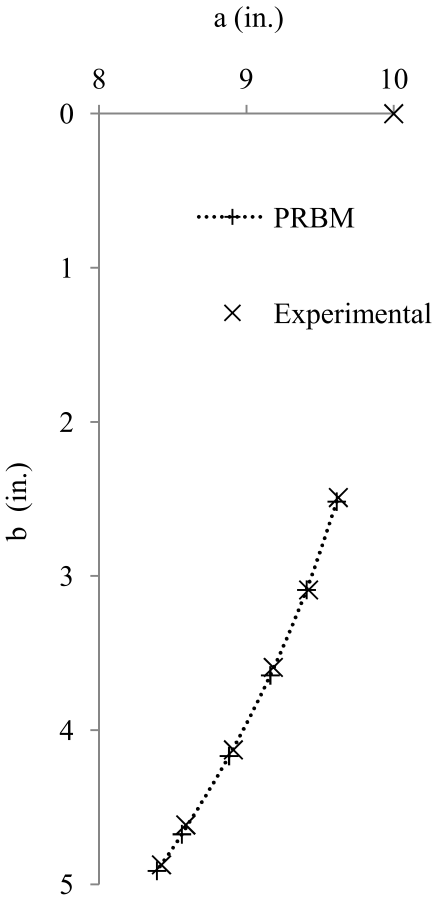

Figure 5.12. PRBM vs. Experimental Beam End Coordinate Comparison for Vertical and Compressive Loading

5.3.3. Experiment 3 – Vertical and Tensile Loading. For the third and final experiment, the beam was subjected to vertical and tensile loads as shown in Figure 5.13. To apply tensile loads, the rope was passed over two pulleys and the loads were applied at an angle of 117^0 measured from the right horizontal in the anticlockwise direction. Figure 5.14 shows the calculation of the actual force acting on the beam, considering the effect of friction at the pulleys. Table 5.3 lists the beam end coordinates as calculated from PRBM and experimental testing for the applied loads. The x and y coordinates from the experiment were recorded and plotted against the PRBM results as shown in Figure 5.15. The results compared favorably with a maximum error of 0.87%. The Maple code for this experiment can be found in Appendix C.

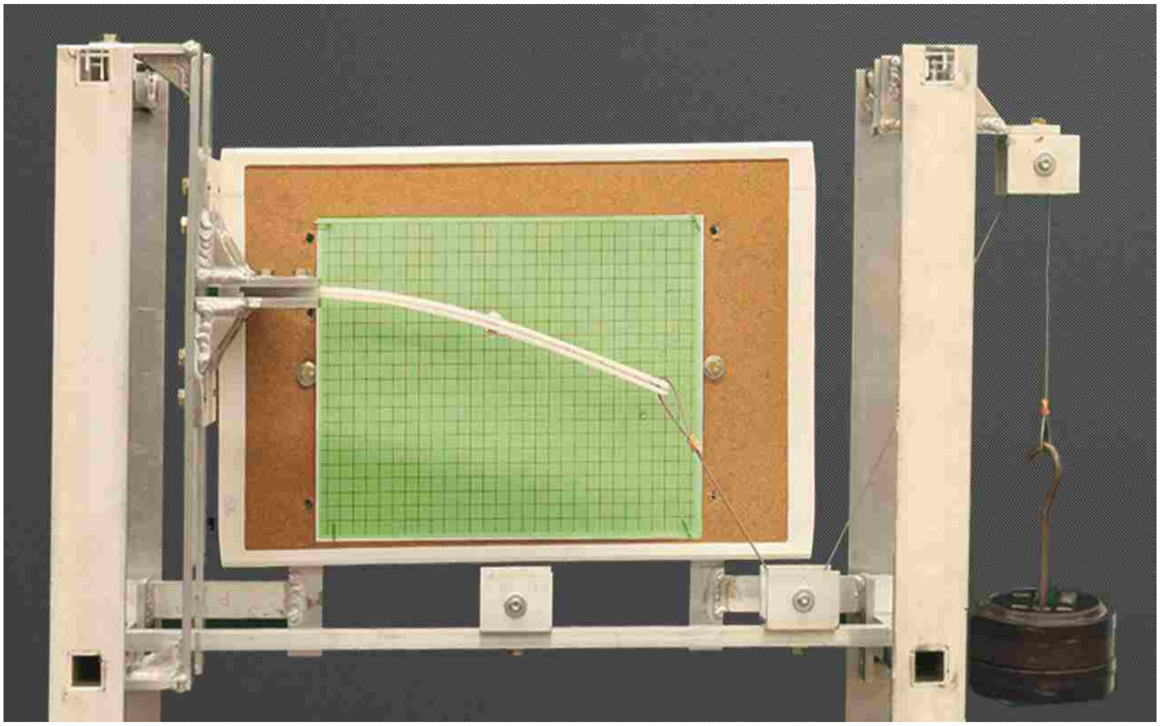

Figure 5.13. Experiment 3 – Vertical and Tensile Loading

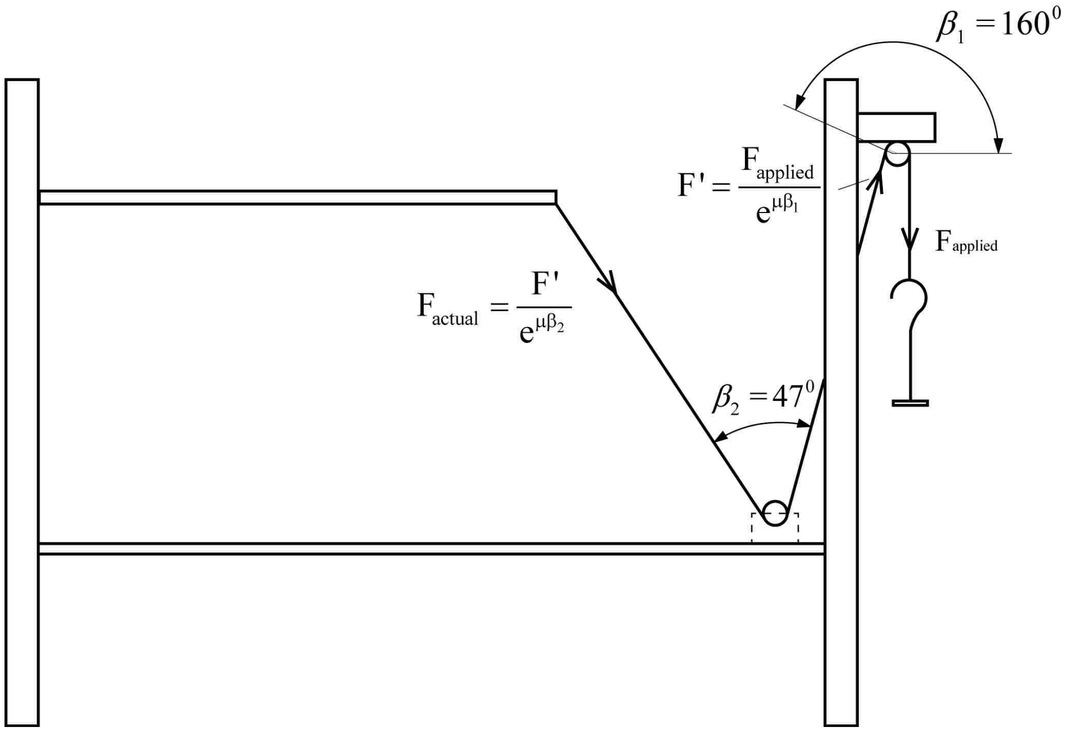

Figure 5.14. Calculation of the Actual Force Acting on the Beam for Experiment 3

Table 5.3 Beam End Coordinate Comparison for Vertical and Tensile Loading

	Experimental		PRBM		
$F_{applied}$	b_e	a_e	b_{PRBM}	a_{PRBM}	Relative error (%)
0	0	10	0	10	-
4	1.902	9.791	1.933	9.781	0.7399
5	2.197	9.734	2.213	9.712	0.5772
6	2.421	9.652	2.45	9.647	0.5930
7	2.621	9.596	2.664	9.582	0.8733
8	2.819	9.539	2.859	9.515	0.8688
8.5	2.898	9.508	2.938	9.488	0.8214

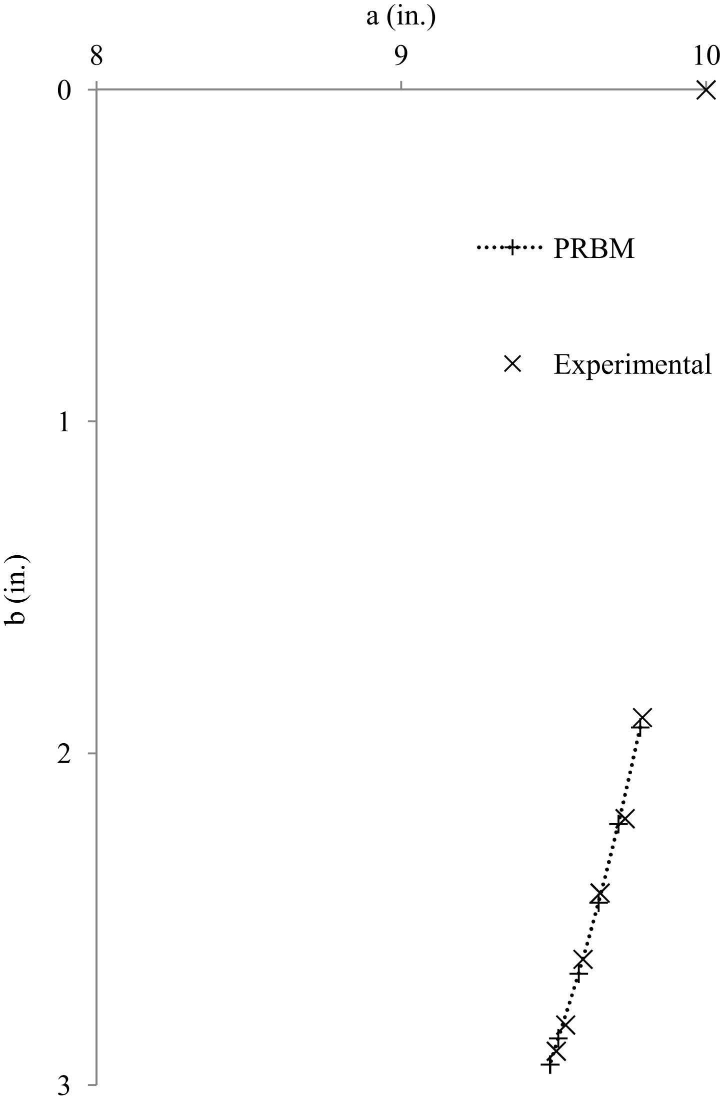

Figure 5.15. PRBM vs. Experimental Beam End Coordinate Comparison for Vertical and Tensile Loading

5.4. CREEP TEST

To validate the proposed methodology for creep alleviation, two simple experiments were performed to compare the creep behavior of plastics in bending, with and without inserts. For this experiment, polypropylene was chosen over Delrin®

because Polypropylene showed more dramatic response to creep. The beams used for this experiment exhibit following geometric and material properties:

Plastic Beams 1 and 2:

Length, L = 10 inches; Width, $w_1 = w_3$=1.5 inch; Height, $h_1 = h_3$ = 0.0625 inches;

Material =Polypropylene; Modulus of Elasticity, E = 250,000 psi.

Insert:

Length, L =10 inches; Width, w_2 = 1 inches; Height, h_2 = 0.025 inches;

Material = Spring Steel; Modulus of Elasticity, E = 30 x 10^6 psi.

5.4.1. Creep. For the first experiment, the two polypropylene beams, without insert, were subjected to stress levels of 2800 psi by applying a calculated load for a period of one hour. After unloading, the readings of the deflection retained due to creep were recorded.

Figure 5.16 (a) shows the beams without insert in loaded position and 5.16 (b) shows the deformation in the beams due to creep after unloading. The beams without insert were subject to a vertical deflection of 6.487 inches. After unloading, the beams retained a vertical deflection of 2.637 inches due to creep. Hence, the creep in the beams immediately after unloading was 36.49% of the deflection.

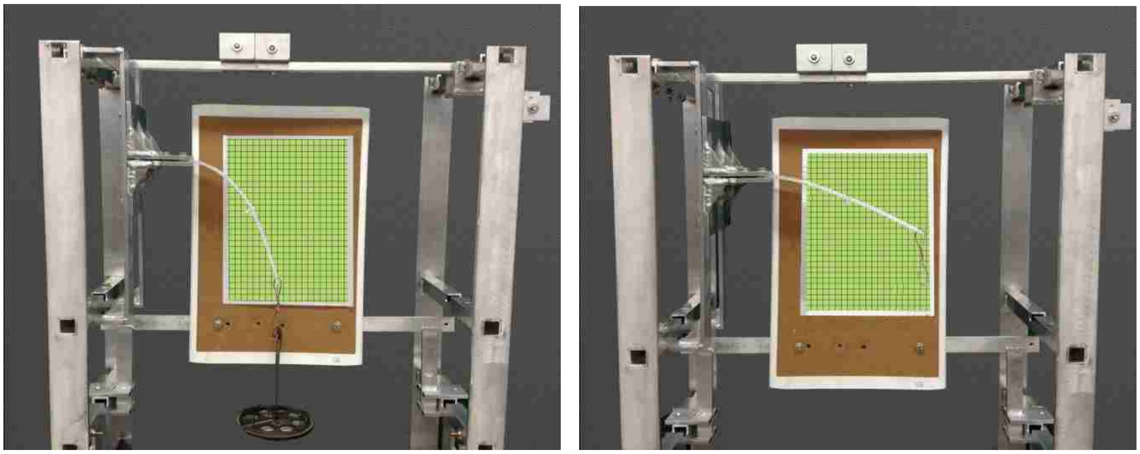

(a) (b)

Figure 5.16. Creep Test – Without Insert (a) Loaded; and (b) Unloaded

The second experiment was performed by placing the spring steel insert between two layers of polypropylene. The plastic beams were subjected to similar stresses of 2800 psi by applying suitable loads for a period of one hour. Readings of the deflection due to creep after unloading were recorded similar to the first experiment.

Figure 5.17 (a) shows the beams with insert in loaded position and 5.17 (b) shows the deformation in the beams due to creep after one hour of loading. The beams with insert were subject to a vertical deflection of 6.26 inches. The beams retained a vertical deflection of 0.65 inches due to creep, after unloading. Hence, the beams with insert showed a creep of 10.40% of the deflection after unloading.

(a) (b)

Figure 5.17. Creep Test – With Insert (a) Loaded; and (b) Unloaded

5.4.2. Creep Recovery: Creep recovery is defined as the rate of decrease in the deformation that occurs when load is removed after prolonged application in a creep test. The amount of recovery depends on the stress levels, loading time and the time allowed for recovery; some plastics may exhibit full recovery if sufficient time is allowed for recovery (Findley, 1989). For the stress levels observed in this experiment (2800 psi), approximately 35-40% creep deformation is recovered in first five minutes (Flinn, 1995).

To observe the effect of creep recovery, further two readings of the deflection were taken after every five minutes. The beams without insert recovered 30.62% of the deflection due to creep in first five minutes and 40% in ten minutes after unloading, whereas, the beams with insert showed a steep recovery of 63.95% of the deflection due to creep in first five minutes and 74% in ten minutes after unloading.

5.5. DISCUSSION OF RESULTS

The experimental testing of a fixed-free compliant beam with an insert yielded very close results compared to the theoretical PRBM results, exhibiting a maximum relative error of 0.95%. The error present may have occurred due to following reasons:

(1) Difference in the approximated value of the elastic modulus of the plastic and insert material.
(2) Error in measurement.
(3) Unaccounted friction between the beams.
(4) Axial stiffening of the beams.

Attempts were made to accommodate most of the points mentioned above in the theoretical calculations as explained in the previous sections, which have helped in achieving fairly accurate results. More research into considerations of the factors contributing to the errors would help to reduce the errors further.

The results from the creep test showed that the deformation due to creep in the beams with insert was reduced significantly from 36.49% to 10.40% of the deflection. Creep resistance is defined as a polymer's ability to resist any kind of deformation when under a load over an extended period of time. Hence, it can be said that the creep resistance of the beams with inserts was significantly improved as compared to the beams without inserts.

As discussed earlier, creep recovery is the rate of decrease in the deformation that occurs when load is removed after prolonged application in a creep test. Hence, it would be desirable to achieve a faster recovery to reduce the creep deformation in the material in a shorter period of time. The experimental results showed that the beams without insert had recovered 30.62% of in first five minutes and 40% after ten minutes after unloading, whereas, the beams with insert had recovered 63.95% in first five minutes and 74% after ten minutes after unloading. This shows that the recovery rate is significantly improved with the insert. To achieve near-full recovery, the resistance force of the plastic must be much smaller than the restoring force of the insert material. If a faster and better recovery is required, higher rigidity (EI) of the metal insert could be utilized.

5.6. SUMMARY

In this Section, the pseudo-rigid-body-model for a fixed free beam with an insert has been validated using experimental testing. Three experiments have been performed by subjecting the beam to vertical, compressive and tensile loading. The comparison of the experimental results with the theoretical PRBM model has been presented by showing plots of the beam end coordinates. An experiment comparing the creep behavior of the plastic with and without insert material was performed and discussed. The results are discussed briefly providing a rationale for the causes of error in the experimental testing and an insight on the results from creep test.

6. CONCLUSIONS AND RECOMMENDATIONS

6.1. CONCLUSIONS

Compliant mechanisms offer many potential advantages over their traditional rigid-body counterparts in engineering designs, such as, reduction in the number of parts, cost, wear; ease of assembly; increased mechanical precision, etc., as mentioned in Section 1. Pseudo-rigid-body model offers a simple method of large deflection analysis, and helps expedite the compliant mechanism design process. PRBMs give fairly accurate results in the analysis of large deflection members. A method to improve the accuracy of the PRBM of a fixed-free beam has been presented in Section 3. The results from the improved method and the old method are compared with the elliptic integral method, and elaborate results may be found in Appendix A.

In spite of the inherent advantages of compliant mechanisms, their use has been limited whenever fabricated from thermoplastic materials, and subjected to forces over sustained periods of time. They are likely to experience creep, rendering them ineffective. A methodology to reduce the creep and effectively increase the strength of materials by using an insert of a stronger material between plastic layers has been explored in Section 4. The pseudo-rigid-body models for compliant links with inserts for various boundary conditions and cases were satisfactorily developed and validated with the elliptic integrals and finite element analysis. The experimental validation of the pseudo-rigid-body model of the fixed-free compliant beam with an insert has been presented in Section 5. Three different experiments with vertical, vertical and compressive, and vertical and tensile loading were conducted to reproduce the theoretical results from the PRBM in an attempt to give the reader confidence in its accuracy. The results of all the three experiments compared very well with the PRBM results exhibiting a maximum error of 0.95%. The consistency of the results in all three experiments provides confidence in the repeatability of the experiment. An experiment comparing the creep behavior of the plastic with and without the insert material was performed and discussed. The experimental results showed that the creep resistance and the creep recovery time were significantly improved in the plastic beams with insert as compared to the beams without insert.

6.2. FUTURE WORK

The area of compliant mechanisms is relatively newer compared to the large knowledge base in existence for rigid-body mechanisms. It is hoped that the ideas presented in this thesis will help to advance further research and development in this field, by presenting new alternatives in material selection and fabrication, to overcome what has been a limiting factor in the use of compliant mechanisms. The proposed methodology, of using inserts to alleviate creep and increase strength of compliant segments, is a preliminary step towards accomplishing the objective of addressing the problems associated with the use of thermoplastic materials in compliant mechanisms.

The use of pseudo-rigid-body models (PRBMs) presented in this work plays a vital role in expediting the design process of compliant mechanisms. The improved K_Θ expressions presented in Section 3 provide a method to increase the accuracy of PRBM for a fixed-free beam. With further insight into this topic, similar expressions may be developed for other boundary conditions which would help improve the slate of PRBMs.

The work presented in Section 4 provides PRBMs for compliant segments with inserts subject to varied boundary conditions and cases. This methodology of PRBMs for compliant segments with inserts may be extended to the more complex compliant mechanisms and their applications, with various force and displacement boundary conditions. In the future, another possible area of research could be exploring the manufacturing possibilities of the compliant beams with inserts and exploring real-life applications of the same.

The experimental validation of the fixed-free compliant beam with insert, and creep test results with and without the insert, are presented in Section 5. Similar experimental validations may be conducted for more cases of the PRBMs of compliant segment types with inserts, as well as the more complex compliant mechanisms composed therefrom.

Recent advances in the compliant mechanism theory have led to the development of superior products that help reduce cost and part count, and improve their quality and reliability. Further research in this area should investigate viable manufacturing techniques for the compliant segments and mechanisms with inserts, as well as applications thereof to render them more practical and develop newer and more efficient products that offer significant and distinct benefits to society.

BIBLIOGRAPHY

Bisshopp, K.E., and Drucker, D.C., 1945, “Large Deflection of Cantilever Beams,” *Quarterly of Applied Mathematics,* Vol. 3, No. 3, pp. 272-275.

Burns, R.H., 1964, “The Kinetostatic Synthesis of Flexible Link Mechanisms,” Ph.D. Dissertation, Yale University.

Burns, R.H., and Crossley, F.R.E., 1966, “Structural Permutations of Flexible Link Mechanisms,” ASME Paper No. 66-Mech-5.

Byers, F.K., 1990, “Design of a Compliant Gripper Mechanism,” B.S. Honors Thesis, Purdue University.

Byers, F.K., and Midha, A., 1991, “Design of a Compliant Gripper Mechanism,” *Proceedings of the 2nd National Applied Mechanism and Robotics Conference*, Cincinnati, Ohio, pp. XC.1-1 – XC.1-12.

Coulter, B. A., and Miller, R.E., 1988, “Numerical Analysis of a Generalized Plane Elastica with Non-Linear Material Behavior,” *International Journal for Numerical Methods in Engineering*, Vol. 26, pp. 617-630.

Dixon-Stubbs, P. J, 1981, “Creep Behavior of Polyethylene and Polypropylene,” *Journal of Material Science*, Vol. 16, pp. 389-396.

Edwards, B.J., 1996, “Functionally Binary Pinned-Pinned Segments,” M.S. Thesis, Brigham Young University.

Erdman, A.G., and Sandor, G.N., 1991, *Mechanism Design: Analysis and Synthesis*, Vol. 1, Second Edition, Prentice-Hall, Englewood Cliffs, New Jersey.

Findley, W. N., Lai, J. S. and Onaran, K., 1989, *Creep and Relaxation of Nonlinear Viscoelastic Materials,* North-Holland Publishing Company, Amsterdam.

Flinn, R. A. and Trojan P. K., 1995, *Engineering Materials and Their Applications*, Houghton Mifflin Company, Boston, MA.

Frisch-Fay, R., 1962, *Flexible Bars*, Butterworth, Washington, DC.

Harrison, H.B., 1973, “Post-Buckling Analysis of Non-Uniform Elastic Columns,” *International Journal for Numerical Methods in Engineering*, Vol. 7, pp. 196-210.

Her, I., 1986, “Methodology for Compliant Mechanism Design,” Ph.D. Dissertation, Purdue University.

Her, I., and Midha, A., 1987, “A Compliance Number Concept for Compliant Mechanism, and Type Synthesis,” *Journal of Mechanisms, Transmissions, and Automation in Design*, Trans. ASME, Vol. 109, No. 3, pp. 348-355.

Her, I., Midha, A., and Salaon, B.A., 1992, “A Methodology for Compliant Mechanisms Design: Part II – Shooting Method and Application,” *Advances in Design Automation*, (Ed.: D.A. Hoeltzel), DE-Vol. 44-2, 18th ASME Design Automation Conference, pp. 39-45.

Hill, T.C., 1987, “Applications in the Design and Analysis of Compliant Mechanisms,” M.S. Thesis, Purdue University.

Hill, T.C., and Midha, A., 1990, “A Graphical User-Driven Newton-Raphson Technique for the use in the Analysis and Design of Compliant Mechanisms,” *Journal of Mechanical Design*, Trans. ASME, Vol. 112, No. 1, pp. 123-130.

Howell, L. L., A. Midha and T. W. Norton, 1996, "Evaluation of Equivalent Spring Stiffness for Use in a Pseudo-Rigid-Body Model of Large-Deflection Compliant Mechanisms," *Journal of Mechanical Design*, Trans. ASME, Vol. 118, No. 1, pp. 126-131.

Howell, L. L., and A. Midha, 1994, "A Method for the Design of Compliant Mechanisms with Small-Length Flexural Pivots," *Journal of Mechanical Design*, Trans. ASME, Vol. 116, No. 1, pp. 280-290.

Howell, L. L., and A. Midha, 1995, "Parametric Deflection Approximations for End-Loaded, Large-Deflection Beams in Compliant Mechanisms," *Journal of Mechanical Design*, Trans. ASME, Vol. 117, No. 1, pp. 156-165.

Howell, L.L., 1991, "The Design and Analysis of Large-Deflection Members in Compliant Mechanisms," MS Thesis, Purdue University.

Howell, L.L., 1993, "A Generalized Loop-Closure Theory for the Analysis and Synthesis of Compliant Mechanisms," Ph.D. Dissertation, Purdue University.

Howell, L.L., 2001, *Compliant Mechanisms,* John Wiley and Sons, Inc., New York, New York.

Howell, L.L., and Midha, A., 1991, "The Effects of a Compliant Workpiece on the Input/Output Characteristics of Rigid-Link Toggle Mechanisms," *Proceedings of the 2nd National Applied Mechanisms and Robotics Conference*, Vol. II, Cincinnati, Ohio, pp. IXB.3-1 – IXB.3-6.

Howell, L.L., and Midha, A., 1993, "Compliant Mechanisms," Section 9.10, *Modern Kinematics: Development in the last Forty years*, (Ed.: A.G. Erdman), John Wiley and Sons, Inc., New York, New York.

Howell, L.L., and Midha, A., 1994, " A Generalized Loop-Closure Theory for the Analysis and Synthesis of Compliant Mechanisms," *Machine Elements and Machine Dynamics*, (Eds.: G.R. Pennock et al.), DE-Vol. 71, 23rd Biennial ASME Mechanisms Conference, pp. 491-500.

Howell, L.L., and Midha, A., 1996, "A loop-Closure Theory for the Analysis and Synthesis of Compliant Mechanisms," *Journal of Mechanical Design,*Trans. ASME, Vol. 118, No. 1, March, pp. 121-125.

James, M.L., Smith, G.M. Wolford, J.C. Whaley, P.W., 1994, *Vibration of Mechanical and Structural Systems*, Second Edition, Harper Collins College Publishers, New York, New York.

Khanuja, S.S., Mettlach, G.A., and Midha, A., 1994, "Graphical Synthesis of Optimal High-Performance Four-Bar Mechanisms," 23rd *Biennial Mechanisms Conference*, DE-Vol.70, Mechanism Synthesis and Analysis, (Eds.: G.R. Pennock et al.) pp. 229-237.

Kimball, C., and W. Tsai, June 2002, "Modeling of Flexural Beams Subjected to Arbitrary Ends Loads," *ASME Journal of Mechanical Design*, Trans. ASME, Vol. 124, No. 2, pp. 223-235.

Mavanthoor, A., 2002, “Design and Stability Analysis of Compliant Mechanisms,” M.S. Thesis, University of Missouri-Rolla.

Meriam, J. L., 1978, *Engineering Mechanics Volume 1, STATICS*, J. Wiley & Sons, pp 301-302.

Mettlach, G.A., and Midha, A., 1995, “Four-Precision-Point-Synthesis of Compliant Mechanisms using Burmester Theory,” *Proceedings of the 4th National Applied Mechanism and Robotics Conference*, Vol. II, Cincinnati, Ohio, December, pp. 63-01-61-08.

Mettlach, G.A., and Midha, A., 1996, “Using Burmester Theory in the Design of Compliant Mechanisms,” *Proceedings of the 24th Biennial Mechanisms Conference*, Irvine, California, August, pp. 96-DETC/MECH-1181-1-8.

Mettlach, G.A., and Midha, A., 1999, “Characteristic Deflection Domain Concept in Compliant Mechanism Design and Analysis,” *Proceedings of the 6th National Applied Mechanisms and Robotics Conference,* Cincinnati, Ohio, December, pp. 27-1 – 27-6.

Midha, A., Bapat, S., Mavanthoor, A., and Chinta V., 2012, “Analysis of a Fixed-Guided Compliant Beam with an Inflection Point Using the Pseudo-Rigid-Body Model (PRBM) Concept,” *Proceedings of the ASME 2012 International Design Engineering Technical Conferences & Computers and Information in Engineering Conference*, Chicago, IL, DETC2012/MECH-71400.

Midha, A., Her, I., and Salamon, B.A., 1992a, “A Methodology for Compliant Mechanisms Design: Part I – Introduction and Large Deflection Analysis,” *Advances in Design Automation,* (Ed.: D.A. Hoeltzel), DE-Vol. 44-2, 18th ASME Design Automation Conference, pp. 29-38.

Midha, A., T. W. Norton and L. L. Howell, 1994 "On the Nomenclature, Classification, and Abstractions of Compliant Mechanisms," *Journal of Mechanical Design*, Trans. ASME, Vol. 116, No. 1, March 1994, pp. 270-279.

Miller, R.E., 1980, “Numerical Analysis of a Generalized Plane Elastica,” *International Journal for Numerical Methods in Engineering,* Vol. 15, pp. 325-332.

Murphy, M.D., 1993, “A Generalized Theory for the Type Synthesis and Design of Compliant Mechanisms,” Ph.D. Dissertation, Purdue University.

Nahvi, H., 1991, "Static and Dynamic Analysis of Compliiant Mechanisms Containing Highly Flexible Members," Ph.D. Dissertation, Purdue University.

Norton, T.W., 1991, "On the Nomenclature, Classification, and Mobility of Compliant Mechanisms," M.S. Thesis, Purdue University.

Norton, T.W., Howell, L.L., and Midha, A., 1991, "Graphical Synthesis of a Four-Bar Mechanism for Specification of Limit Positions or Transmission angle," *Proceedings of the 2nd National Applied Mechanisms and Robotics Conference,* Vol. I, Cincinnati, Ohio, pp. IIA.4-1 – IIA.4-9.

Pauly, J., and A. Midha, 2004, "Improved Pseudo-Rigid-Body Model Parameter Values for End-Force-Loaded Compliant Beams," *Proceedings of the 28th Biennial ASME Mechanisms and Robotics Conference*, Salt Lake City, Utah, pp. DETC 2004-57580 – 1-5.

Salamon, B.A., 1989, "Mechanical Advantage Aspects in Compliant Mechanisms Design," M.S. Thesis, Purdue University.

Salamon, B.A., and Midha, A., 1992, "An Introduction to Mechanical Advantage in Compliant Mechanisms," *Advances in Design Automation,* (Ed.: D.A. Hoeltzel), DE-Vol 44-2, 18th ASME Design Automation Conference, pp. 47-51.

Sevak, N.M., and McLarnan, C.W., 1974, "Optimal Synthesis of Flexible Link Mechanisms with Large Static Deflecitons," ASME Paper No. 74-DET-83.

Shigley, J.E., and Mischke, C. R., 2003, Mechanical Engineering Design, 7th Ed., McGraw-Hill, New York, New York.

Shigley, J.E., and Uicker, J.J., 1995, *Theory of Machines and Mechanisms,* Second Edition, McGraw-Hill, New York, New York.

Shoup, T.E., 1972, "On the Use of Nodal Elastica for the Analysis of Flexible Link Devices," *Journal of Engineering Industry*, Trans. ASME, Vol. 94, No. 3, pp. 871-875.

Shoup, T.E., and Mclarnan, C.W. 1971, "On The Use of the Undulating Elastica for the Analysis of Flexible Link Deviceds," *Journal of Engineering For Industry*, Trans. ASME, pp. 263-267.

Tripathi, D., 2002, *A Practical Guide to Polypropylene,* Rapra Technology Limited, Shropshire, UK.

Winter, S.J., and Shoup, T.E., 1972, “The Displacement Analysis of Path Generating Flexible-Link Mechanisms,” *Mechanism and Machine Theory*, Vol. 7, No. 4, pp. 443-451.

APPENDIX A

PLOTS COMPARING THE OLD AND NEW K_Θ EQUATIONS FOR VARYING LOAD FACTOR

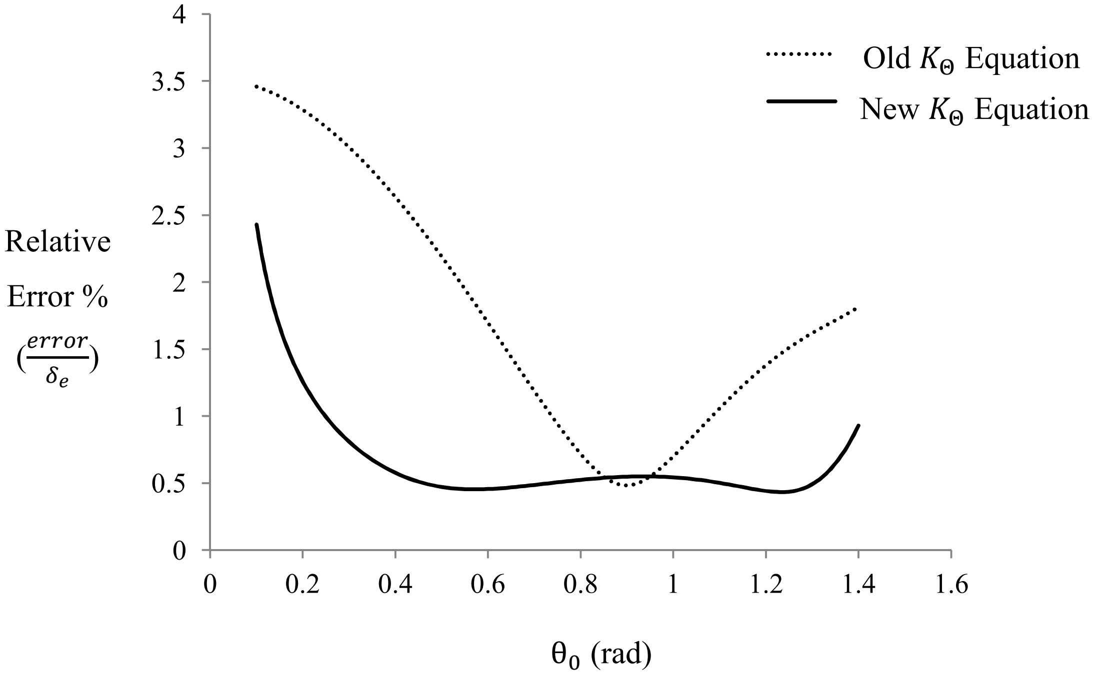

A. 1. Relative Error versus Beam End Angle for $n = 0$

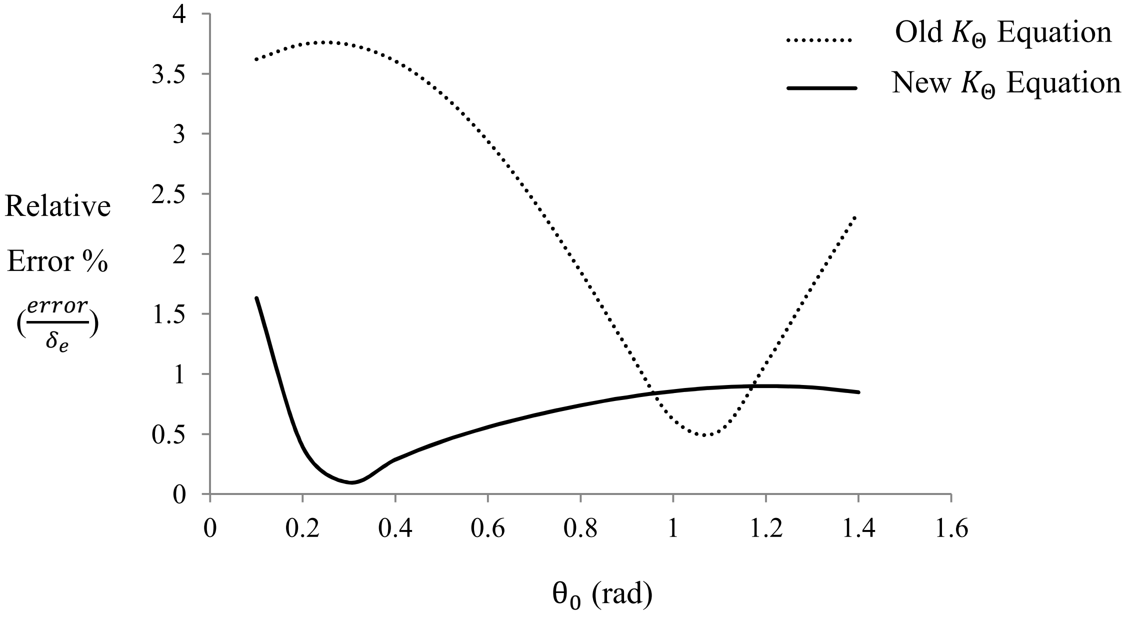

A. 2. Relative Error versus Beam End Angle for $n = 1$

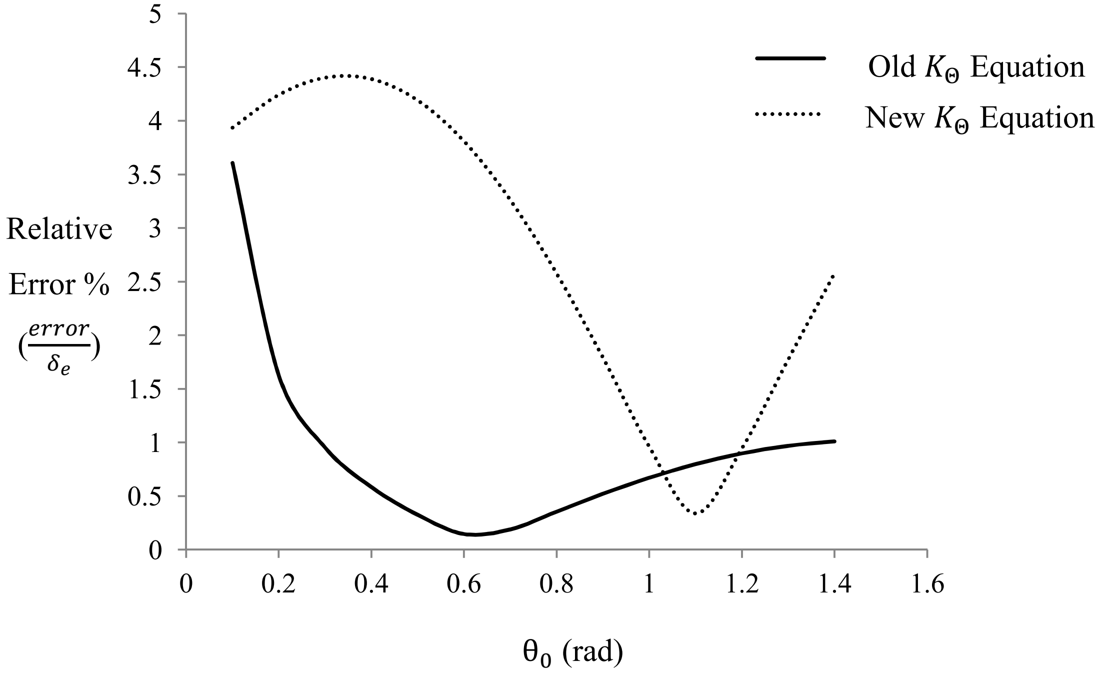

A. 3. Relative Error versus Beam End Angle for $n = 2$

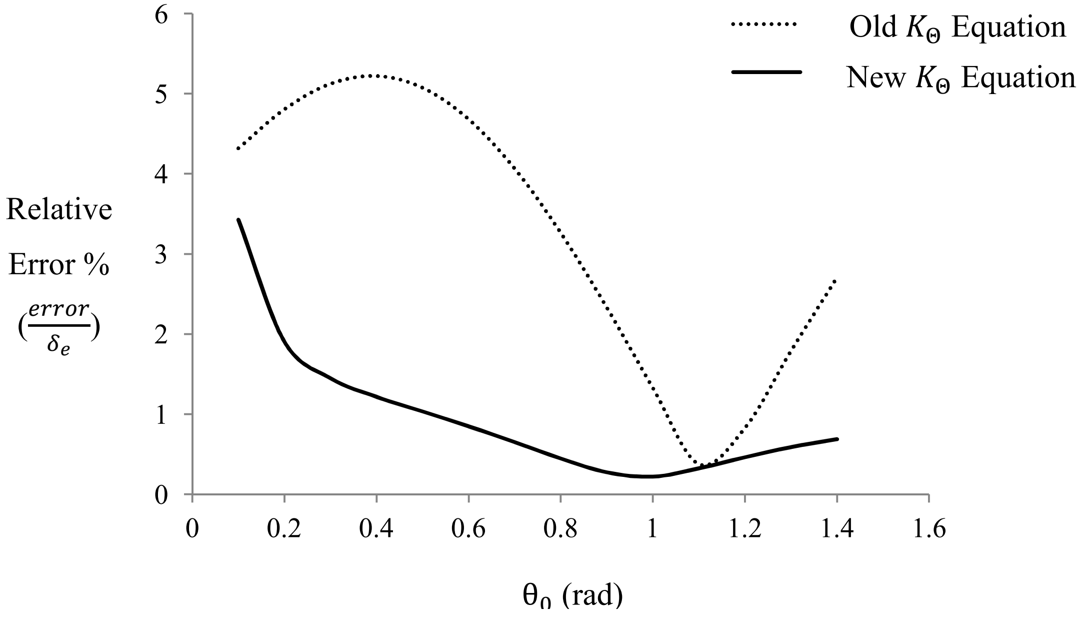

A. 4. Relative Error versus Beam End Angle for $n = 3$

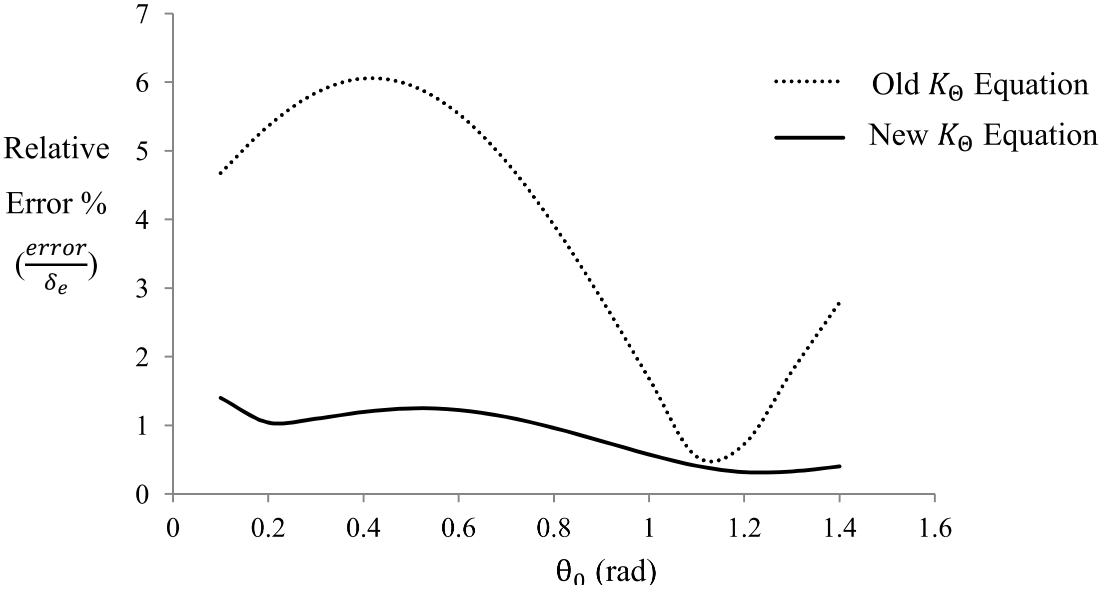

A. 5. Relative Error versus Beam End Angle for $n = 4$

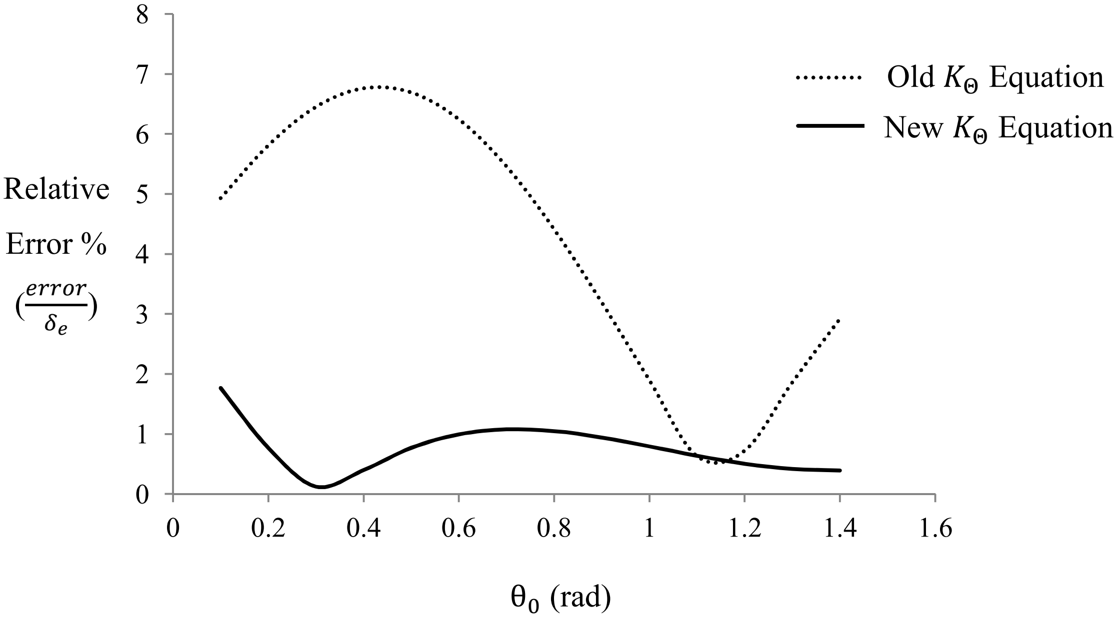

A. 6. Relative Error versus Beam End Angle for $n = 5$

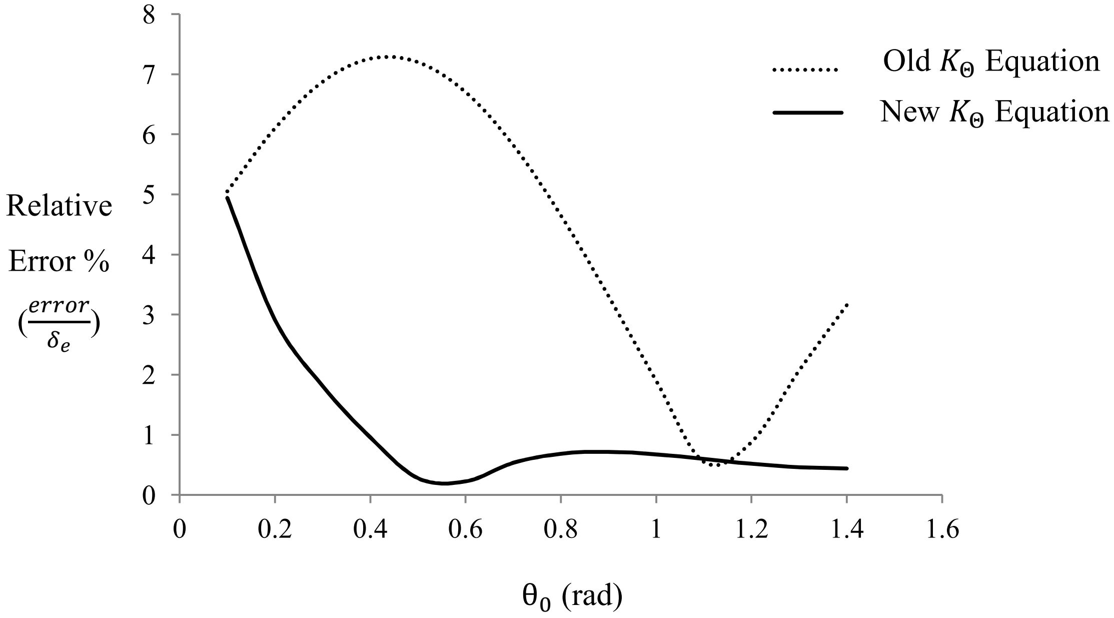

A. 7. Relative Error versus Beam End Angle for $n = 6$

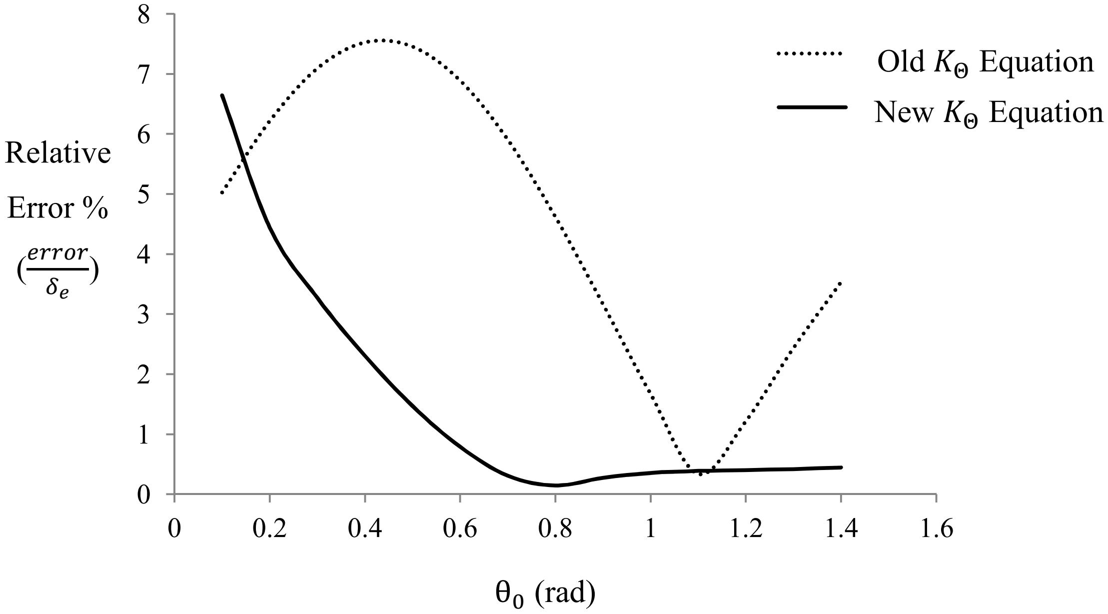

A. 8. Relative Error versus Beam End Angle for $n = 7$

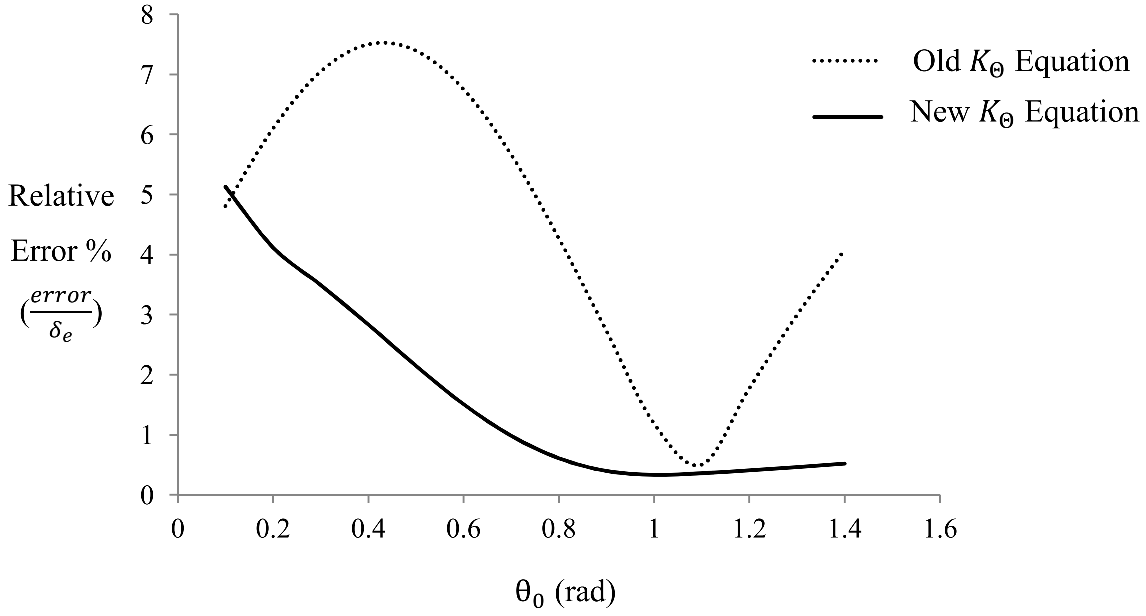

A. 9. Relative Error versus Beam End Angle for $n = 8$

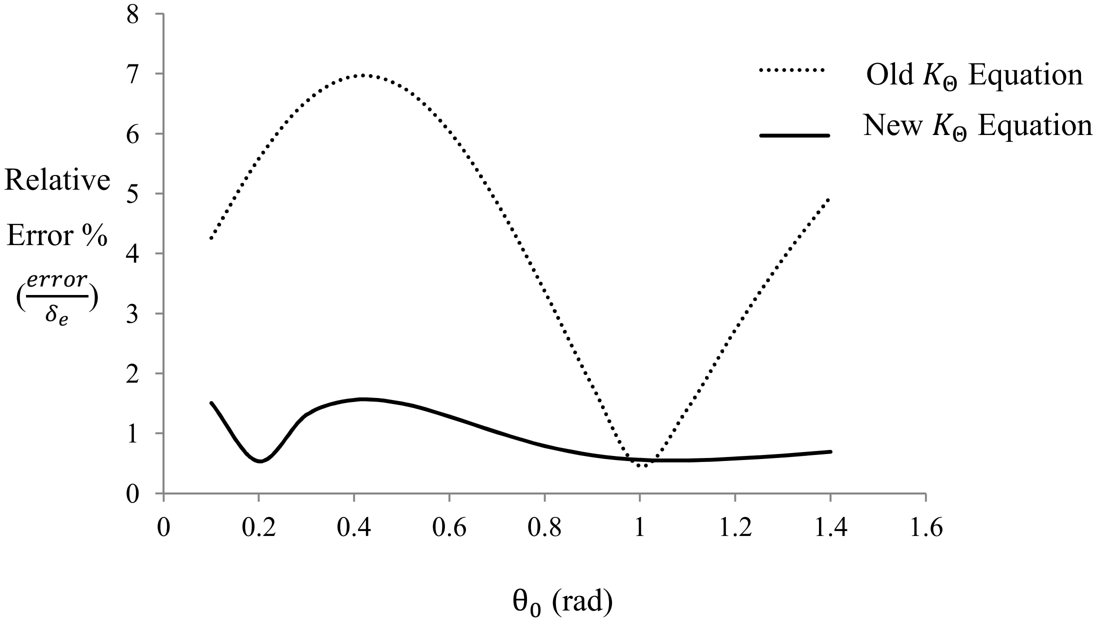

A. 10. Relative Error versus Beam End Angle for $n = 9$

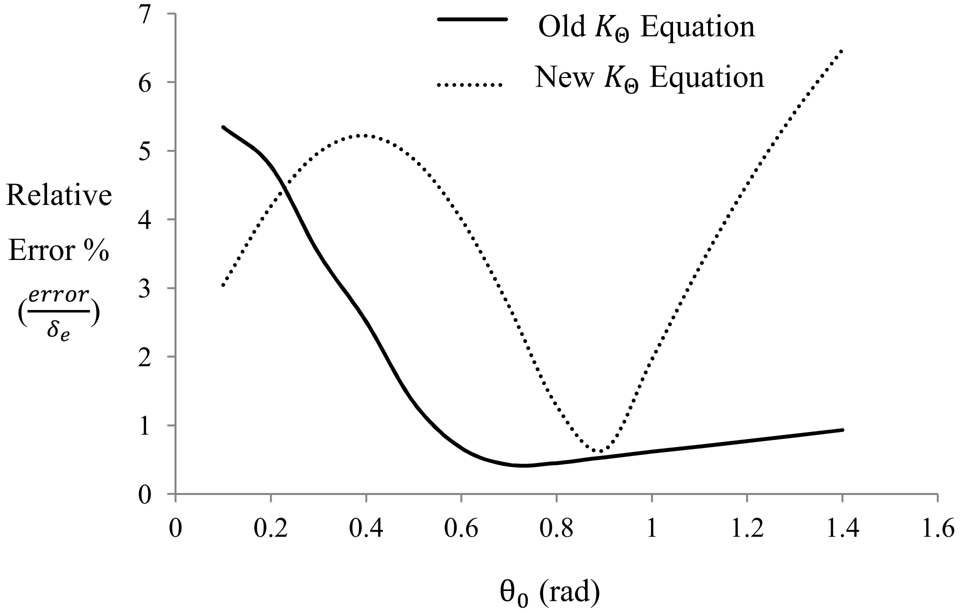

A. 11. Relative Error versus Beam End Angle for $n = 10$

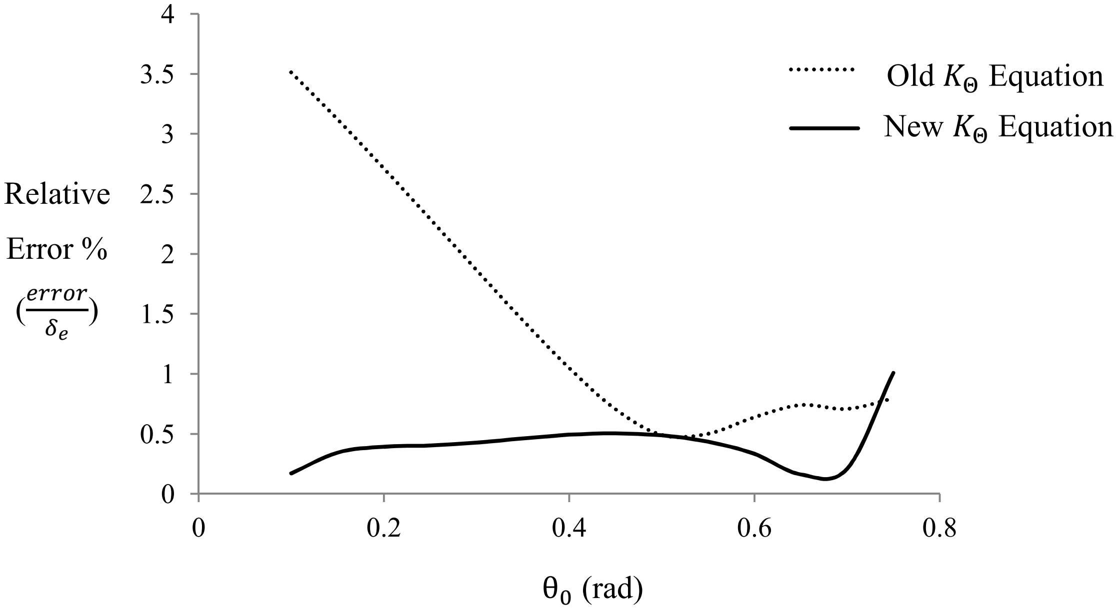

A. 12. Relative Error versus Beam End Angle for $n = -1$

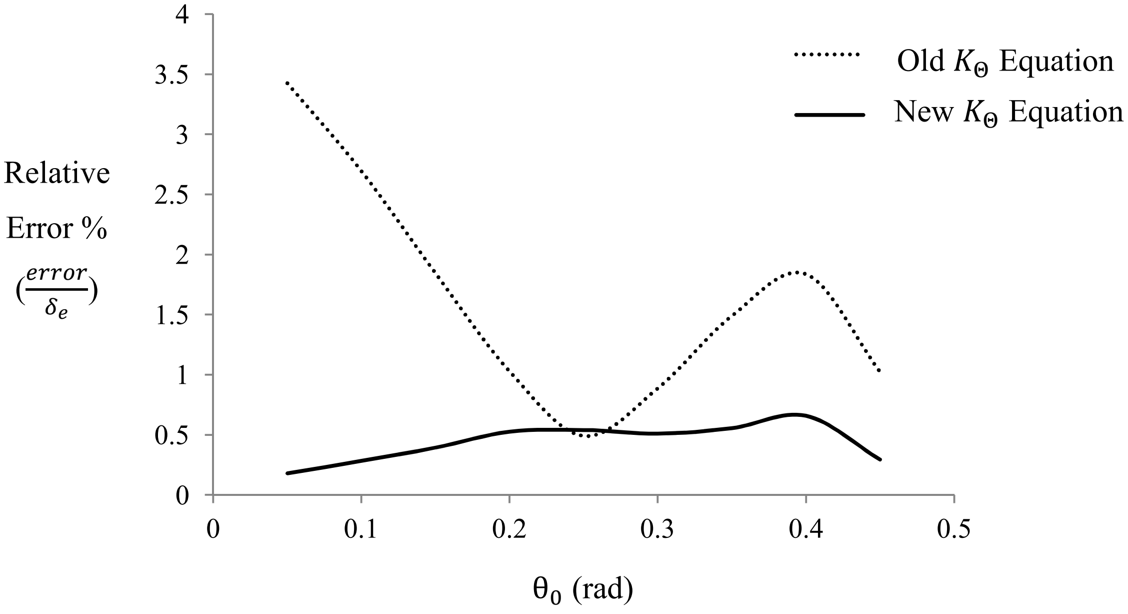

A. 13. Relative Error versus Beam End Angle for $n = -2$

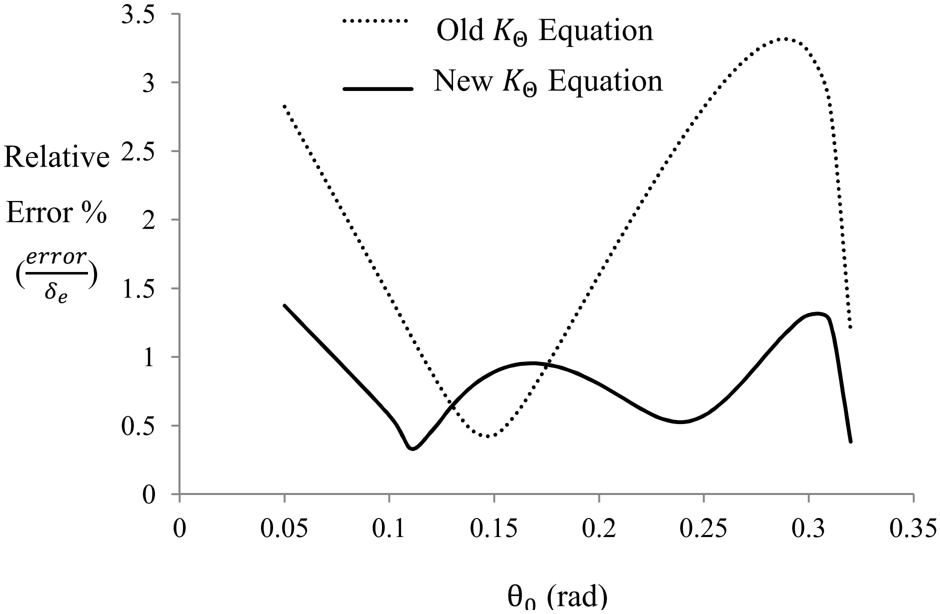

A. 14. Relative Error versus Beam End Angle for $n = -3$

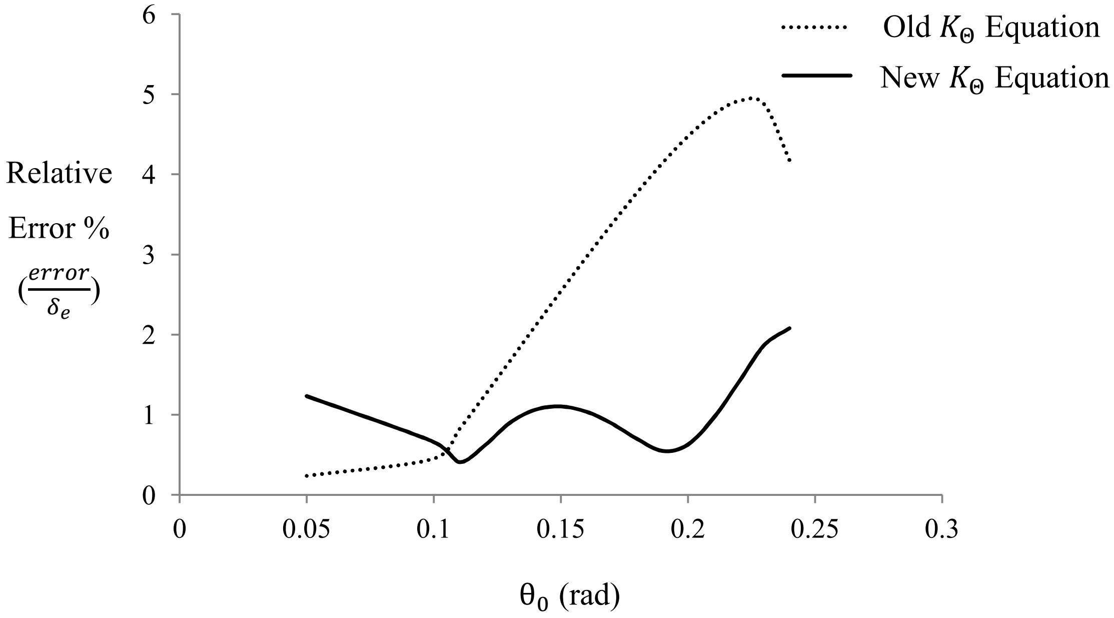

A. 15. Relative Error versus Beam End Angle for $n = -4$

APPENDIX B

MAPLE CODE FOR PRBM RESULTS OF EXPERIMENTS 1 AND 2

> $restart;$

> $unprotect(\mathrm{gamma}) :$

```
> #Enter beam material and geometric properties and load angle:
```

> $\mathrm{n} := 0.896 : \mathrm{L} := 10 : \mathrm{E1} := 550000 : \mathrm{E2} := 30000000 : \mathrm{w1} := 2.5 : \mathrm{w2} := 1 : \mathrm{w3} := 2.5 : \mathrm{h1} := 0.125 : \mathrm{h2} := 0.025 : \mathrm{h3} := 0.125 :$

```
> #Enter value of the load applied:
```

> $P := 4.34;$

$$P := 4.34$$

```
> #Enter value of the coefficient of friction:
```

> $m := 0.01;$

$$m := 0.01$$

> $P1 := evalf\left(\frac{\mathrm{P}}{\mathrm{e}^{\mathrm{m}\cdot\left(\frac{160\cdot\pi}{180}\right)}}\right)$

$$P1 := 4.220480906$$

> $P2 := evalf\left(\frac{\mathrm{P1}}{\mathrm{e}^{\mathrm{m}\cdot\left(\frac{70\cdot\pi}{180}\right)}}\right)$

$$P2 := 4.169231705$$

> $F := evalf\left(\frac{\mathrm{P2}}{\mathrm{e}^{\mathrm{m}\cdot\left(122\cdot\frac{\pi}{180}\right)}}\right) :$

>

> $\mathrm{eta} := \mathrm{sqrt}(1 + n^2);$

$$\eta := 1.342689838$$

```
>
NumericEventHandler(division_by_zero=proc(operator,operands
,defVal)
if operator=ln then return -infinity else return defVal end
if
end proc);
division_by_zero=proc(operator,operands,defVal)defVal end
proc:
```

$$division\_by\_zero = default$$

```
> #Calculate characteristic radius factor:
```

> $\gamma := 0.85189 - 0.020805 \cdot n + 0.005867 \cdot n^2 - 0.000895 \cdot n^3 + 0.000069 \cdot n^4 - 0.000002 \cdot n^5;$

$$\gamma := 0.8373583637$$

$$> K_{\text{theta}} := \frac{1}{\text{theta}} \cdot \big(0.004233335366 - 0.01297170465\, n + 2.5670950459583843\, \theta + 0.003992737439\, n^{2} - 0.03717332563\, \theta^{2} - 0.0002974096442\, n^{3} + 0.1799707532\, \theta^{3} - 0.03467817537\, n\, \theta + 0.003467424816\, n^{2}\, \theta - 0.009474321422\, n\, \theta^{2}\big) :$$

$$> \text{phi} := \pi + evalf\left(\tan^{-1}\left(-\frac{1}{n}\right)\right);$$

$$\phi := \pi - 0.8401955706$$

\> #Calculate M.I. of the beams:

$$> I1 := \frac{w1 \cdot h1^{3}}{12};$$

$$> I2 := \frac{w2 \cdot h2^{3}}{12};$$

$$> I3 := \frac{w3 \cdot h3^{3}}{12};$$

$$> \text{K1} := \gamma \cdot K_{\text{theta}} \cdot \left(\frac{E1 \cdot I1}{L}\right) :$$

$$> K2 := \gamma \cdot K_{\text{theta}} \cdot \left(\frac{E2 \cdot I2}{L}\right) :$$

$$> K3 := \gamma \cdot K_{\text{theta}} \cdot \left(\frac{E1 \cdot I3}{L}\right) :$$

$$> K := K1 + K2 + K3;$$

$$K := \frac{1}{\theta}\big(40.75035005\,(-0.004397812142 + 2.538807105\, \theta - 0.04566231762\, \theta^{2} + 0.1799707532\, \theta^{3})\big)$$

$$> \text{eq1} := \text{K} \cdot \text{theta} - \text{F} \cdot \gamma \cdot \text{L} \cdot \sin(\text{phi} - \text{theta});$$

$$eq1 := -0.1792123842 + 103.4572782\, \theta - 1.860755427\, \theta^{2} + 7.333871192\, \theta^{3} - 34.17589953 \sin(0.8401955706 + \theta)$$

\> #Calculate Pseudo-rigid-body angle

$$> \textbf{theta} := \boldsymbol{fsolve}(eq1 = 0, \text{theta} = 0\,..2);$$

$$\theta := 0.3018607412$$

\> #Calculate beam end coordinates

$$> b := \gamma \cdot L \cdot \sin(\text{theta});$$

$$b := 2.489444041$$

$$> a := L \cdot (1 - \gamma \cdot (1 - \cos(\text{theta})));$$

$$a := 9.621387989$$

APPENDIX C

MAPLE CODE FOR PRBM RESULTS OF EXPERIMENT 3

$>$ *restart*;

$>$ *unprotect*(gamma) :

```
> #Enter beam material and geometric properties and load angle:
```

$>$ n := -0.673 : L := 10 : E1 := 550000 : E2 := 30000000 : w1 := 2.5 : w2 := 1 : w3 := 2.5 : h1 := 0.125 : h2 := 0.025 : h3 := 0.125 :

```
> #Enter value of the load applied:
```

$>$ $P := 4.34;$

```
> #Enter value of the coefficient of friction:
```

$>$ $m := 0.01;$

$>$ $$P1 := evalf\left(\frac{\mathrm{P}}{\mathrm{e}^{\mathrm{m}\cdot\left(\frac{160\cdot\pi}{180}\right)}}\right)$$

$>$ $$F := evalf\left(\frac{\mathrm{P1}}{\mathrm{e}^{\mathrm{m}\cdot\left(47\cdot\frac{\pi}{180}\right)}}\right) :$$

$>$ $\mathrm{eta} := \mathrm{sqrt}\left(1 + n^2\right);$

```
>
>NumericEventHandler(division_by_zero=proc(operator,operands,defVal)

if operator=ln then return -infinity else return defVal end if

end proc);

division_by_zero=proc(operator,operands,defVal)defVal end proc:
```

$$division\_by\_zero = default$$

```
> #Calculate characteristic radius factor:
```

$>$ $\gamma := 0.855651 - 0.016438\cdot n;$

$$\gamma := 0.866713774$$

> $K_{\text{theta}} := \frac{1}{\text{theta}} \cdot \big(0.0006511791252 - 0.008244418725\, n$
$+ 2.544577067\, \theta - 0.004764045850\, n^2 + 0.07121501781\, \theta^2$
$- 0.0001036663527\, n^3 + 0.07969598320\, \theta^3 + 0.06927372525\, n$
$+ 0.06150685207\, n^2\, \theta - 0.3475886083\, n\, \theta^2\big)$:

> $\text{phi} := \mathit{evalf}\left(\tan^{-1}\left(-\frac{1}{n}\right)\right);$

$$\phi := 0.9784219149$$

> `#Calculate M.I. of the beams:`

> $I1 := \frac{w1 \cdot h1^3}{12};$

> $I2 := \frac{w2 \cdot h2^3}{12};$

> $I3 := \frac{w3 \cdot h3^3}{12};$

> $\text{K1} := \gamma \cdot K_{\text{theta}} \cdot \left(\frac{E1 \cdot I1}{L}\right)$:

> $K2 := \gamma \cdot K_{\text{theta}} \cdot \left(\frac{E2 \cdot I2}{L}\right)$:

> $K3 := \gamma \cdot K_{\text{theta}} \cdot \left(\frac{E1 \cdot I3}{L}\right)$:

> $K := K1 + K2 + K3;$

> $\text{eq1} := \text{K} \cdot \text{theta} - \text{F} \cdot \gamma \cdot \text{L} \cdot \sin(\text{phi} - \text{theta});$

> `#Calculate Pseudo-rigid-body angle`

> $\textbf{theta} := \boldsymbol{\mathit{fsolve}}(eq1 = 0, \text{theta} = 0\,..2);$

$$\theta := 0.2249187208$$

> `#Calculate beam end coordinates`

> $b := \gamma \cdot L \cdot \sin(\text{theta});$

$$b := 1.933006863$$

> $a := L \cdot (1 - \gamma \cdot (1 - \cos(\text{theta})));$

$$a := 9.781694196$$

VITA

Raghvendra Sharadchandra Kuber was born in 1988 in India. He received his primary and secondary education in Aurangabad, India. After completing his junior college, he attended the Government College of Engineering, Aurangabad, and graduated first class with distinction in August of 2009. He moved to the United States to pursue a Master of Science degree program in Mechanical Engineering at Missouri University of Science and Technology, Rolla, MO, and received his degree in May 2013.